UNIVERSITÀ DEGLI STUDI DI TRIESTE

XXII CICLO
DEL DOTTORATO DI RICERCA IN
FISICA

Study of T-odd parton distribution functions in polarised Drell-Yan processes at COMPASS

Settore scientifico-disciplinare
FISICA NUCLEARE E SUBNUCLEARE (FIS/04)

ANNO ACCADEMICO 2008/2009

Dottorando
Stefano Takekawa

Coordinatore del collegio dei docenti
chiar.mo prof. Gaetano Senatore

Relatore
chiar.mo prof. Franco Bradamante

Tutore
chiar.mo prof. Franco Bradamante

Correlatore
chiar.mo prof. Daniele Panzieri

Contents

Chapter 1

Introduction

The knowledge of the constituents of matter has expanded during the last one hundred years. Since the experiments which sir Rutherford made to probe the structure of the atoms and which led to the discovery of the nucleus, the capability to explore the infinite small has grown, as a consequence of the improving resolution available with increasing energy particle accelerators. Big jumps were done: nuclei were discovered to be made of nucleons, and in the 1970s first experiments proved that they are made of more basic elements, the quarks whose existence we are nowadays familiar with. The parton model (PM), developed in the late 1960s, was successfull and many properties of the nucleon (and other hadrons) were understood in a simple way. The evolution of theory led to the modern Quantum Chromodynamics (QCD) which can consistenlty describe, with a complete approach, hadrons and their interaction.

A lot of attention has been, and still is, given to the structure of the proton, which is one of the basic constituent of the world we see every day. By means of PM, quark model (QM) and QCD almost all its properties can be understood and modelized.

However, since more than 20 years, the spin structure of the proton is still debated. The discussion was started when, in 1987, the European Muon Collaboration (EMC), surprised the physics community and showed that the spin of the quarks only contributes to a small fraction, $\Delta\Sigma$, of the proton spin [1]. Since then, the question "Where is the spin of the proton?" [2] still waits a conclusive answer.

The longitudinal spin of the proton can be decomposed in the sum of differ-

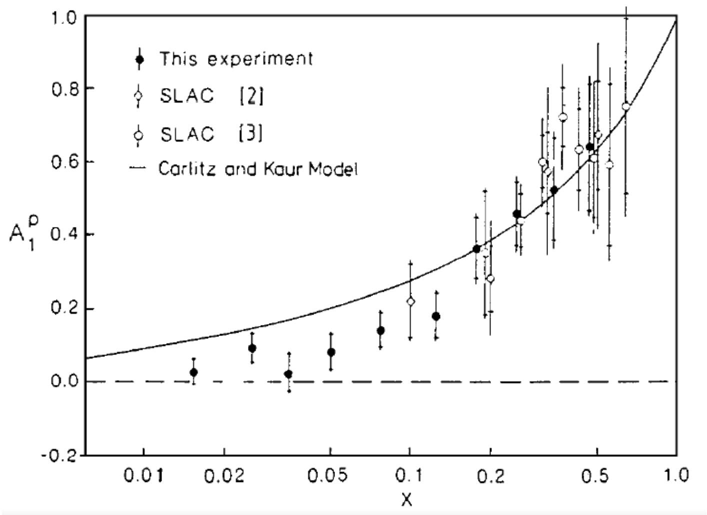

Figure 1.1: Measured values of the asymmetry A_1^p from SLAC (open circles) and from EMC measurements (full circles). The smooth curve is a theoretical calculation based on standard quark model. The points added by EMC at lower x allowed to better compute the contribution of quarks to the proton spin, and it was found compatible with zero.

ent terms:

$$\frac{1}{2} = \frac{1}{2}\Delta\Sigma + \Delta G + \langle L_z \rangle \tag{1.1}$$

where $\Delta\Sigma$ is the contribution of quarks to the proton spin, ΔG is the contribution of the gluons and $\langle L_z \rangle$ is the contribution coming from the orbital momentum of quarks and gluons inside the proton. In the most naïve model, when one thinks that only quarks carry the proton spin, $\Delta\Sigma$ is equal to one and all the other terms are zero. The prediction for these values can be improved by adding relativistic correction, thus obtaining $\Delta\Sigma \approx 0.75$ and finding small contribution to orbital momentum angular momentum $\langle L_z \rangle$ coming only from quarks, while still no contributions come from the gluons. Improved results are obtained when the quark flavour is taken into account, and using u, d and s and SU(3) symmetry the value of $\Delta\Sigma$ can be lowered to 0.6. EMC came in this picture with the measurement of $\Delta\Sigma = \Delta u + \Delta d + \Delta s = 0.12 \pm 0.09 \pm 0.14$, which is compatible with zero [1]. That was a real *spin crisis* and the *spin puzzle* began. Fig. 1.1 shows the original data of the asymmetry A_1^p measured by EMC. The quantity $A_1^p(x)$

is given by:

$$A_1^p(x) = \frac{\sum_f e_q^2 \left[(q+\bar{q})^{\uparrow} - (q+\bar{q})^{\downarrow} \right]}{\sum_f e_q^2 \left[(q+\bar{q})^{\uparrow} + (q+\bar{q})^{\downarrow} \right]} = \frac{\frac{4}{9}\Delta u + \frac{1}{9}\Delta d + \frac{1}{9}\Delta s}{\frac{4}{9}u + \frac{1}{9}d + \frac{1}{9}s} \tag{1.2}$$

In this expression $\Delta q(x) = (q+\bar{q})^{\uparrow} - (q+\bar{q})^{\downarrow}$ and u, d and s are the three light quarks flavours q of charge e_q; $\uparrow$ and $\downarrow$ refer to the spin of quark, whether they are parallel or anti-parallel to the longitudinal nucleon spin. $A_1^p(x)$ could be extracted from the measured cross section asymmetry. Combining the result for $A_1^p(x)$ and relations given by the weak decays of the baryon octect, one finally obtains $\Delta\Sigma = 0.12 \pm 0.09 \pm 0.14$. But this is only the beginning of the story. The helicity structure of the proton is much more complicated and much work has been done to clarify the problem. Other experiments were done to confirm and extend the results of EMC, like SMC at CERN, and E142, E143, E154, E155 at SLAC; all these experiments, which made their investigation exploiting the Deep Inelastic Scattering (DIS), which consist in using a lepton to probe the nucleon, confirmed EMC results. The two most recent experiments used and still use Semi Inclusive Deep Inelastic Scattering (SIDIS), like HERMES at HERA and COMPASS at CERN. SIDIS process differs from DIS because a hadron is measured in the final state in addition to the scattered lepton. Other experiments focusing on spin physics (STAR, PHENIX, BRAMHS), were also developed at Relativistic Heavy Ion Collider (RHIC) in Brookhaven where polarised proton beams are used to investigate the proton structure.

Contemporary, theory did lots of improvements in the description of proton. To fully describe the DIS process with polarised beam and target, the two structure functions $\mathcal{F}_1$ and $\mathcal{F}_2$ are not enough and to describe the helicity structure of the proton, two more structure functions, g_1 and g_2, are necessary to describe a polarised proton. g_1 and g_2 were measured in the experiments mentioned above, so a reasonable knowledge exists.

However, a better discussion can be done focusing attention to parton distribution functions (PDF) of the proton. At leading order, a complete description of the proton requires three parton distribution functions. In the collinear approximation, they are the momentum distribution function $q(x)$, the helicity distribution function $\Delta q(x)$ and the transversity function $\Delta q_T(x)$. Access to $q(x)$ and $\Delta q(x)$ is possible with DIS while to address the transversity distribution $\Delta q_T(x)$ one needs Semi Inclusive Deep Inelastic Scattering (SIDIS) in which a hadron is detected in the final state in addition to the scattered beam particle. SIDIS is needed because of the chiral-odd property of transversity, which requires to be convoluted with another chiral-odd function (fragmentation functions) to be observable.

It has been realised in the recent years that the structure of the proton is even more complicated and a new picture can be drawn when the intrinsic transverse momentum of partons, $\mathbf{k}_T$, is taken into account. In this case the number of parton distribution functions increases to eight: $f_1\left(x, \mathbf{k}_T^2\right)$, $g_{1L}\left(x, \mathbf{k}_T^2\right)$, $h_1\left(x, \mathbf{k}_T^2\right)$, $g_{1T}\left(x, \mathbf{k}_T^2\right)$, $h_{1L}^{\perp}\left(x, \mathbf{k}_T^2\right)$, $h_{1T}^{\perp}\left(x, \mathbf{k}_T^2\right)$, $h_1^{\perp}\left(x, \mathbf{k}_T^2\right)$ and $f_{1T}^{\perp}\left(x, \mathbf{k}_T^2\right)$. The first three functions, when integrated over $\mathbf{k}_T$ give back $f(x)$, $\Delta f(x)$ and $\Delta f_T(x)$, while the others vanish. The last three functions have been named, respectively, Pretzelosity, Boer-Mulders and Sivers functions; some knowledge on the Sivers function has been obtained by HERMES collaboration at DESY and by COMPASS, while the first two are unknown. Nevertheless some speculations have been done for the Boer-Mulders function.

Apart from polarised SIDIS, another way to measure transverse momentum dependent (TMD) PDF is to study the Drell-Yan process. Drell and Yan proposed a model, in the beginning of 1970s, to explain a continuum di-muon spectrum: a quark and an anti-quark coming from two different hadrons annihilate producing a virtual photon which then decays into a lepton pair. For thirty years many experiments were done focusing on Drell-Yan processes and recently several experiment were proposed to extract TMD PDFs. Among them, a proposal has been worked out for a Drell-Yan program at COMPASS; the existence of a polarised target in COMPASS will make possible to study single polarised Drell-Yan process as well as unpolarised one. The Drell-Yan cross section has modulations due to polarisation state of target and these contributions allow to extract TMD PDFs. Moreover Drell-Yan has a complementary role to SIDIS, improving the knowledge of proton and offering the possibility of a new test of QCD. In fact the naïvely T-odd Sivers and Boer-Mulders functions, measured with Drell-Yan process, are predicted to have a change of sign with respect to ones they have in SIDIS.

This short and dense sorting of facts and experiments may transmit the wrong idea that all this transversity stuff is something quite new. That is not true, since already in 1976 the importance of transverse spin effects at high energy in hadronic physics was suggested by the discovery that Λ hyperons were produced polarised in unpolarised collisions of a 300 GeV proton beam on Berillium and proton targets [3]. This result, shown in Fig. 1.2(a), was unexpected and cannot be easily explained. The poor understanding of the underlying physics was also manifest in the belief that asymmetries and transverse effects were due to low energy phenomena and that they would disappear at higher energy. However large single spin asymmetries (up to 30-40%, see Fig. 1.2(b)) were observed by E704 [4], where the available center of mass energy was large ($\sqrt{s} \sim 20$ GeV) in pp and $p\bar{p}$ collisions. Also, in the literature the transversity function can be found since 1979 [5]; then it was rediscovered in the 1990s [6, 7], when results, like the one by E704, renewed the interested on it.

This thesis has, as main theme, the studies I have done for writing a

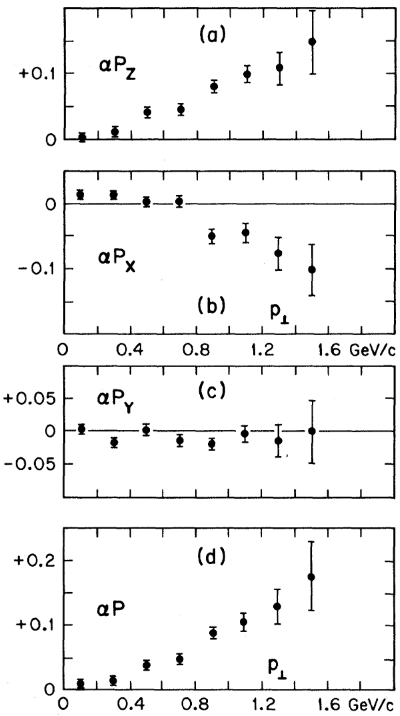

(a)

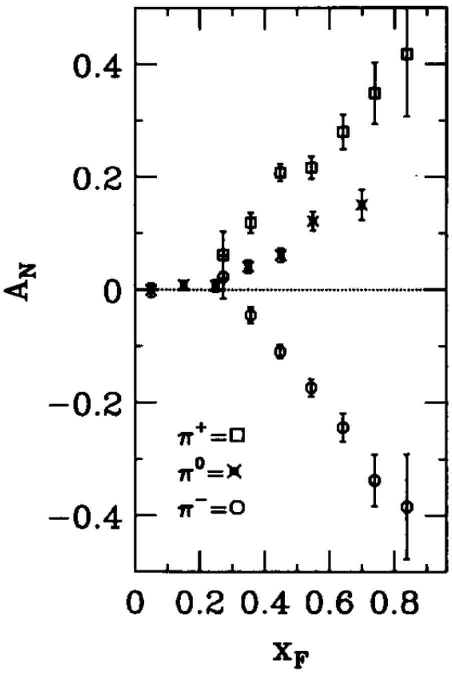

(b)

Figure 1.2: (a) measurements of Λ polarisation for inclusive production in proton-Berillium scattering at Fermilab [3] (b) asymmetries in the inclusive production of pions using a polarised proton beam at Fermilab [4]

proposal of Drell-Yan program at COMPASS. This topic involved me for the main fraction of my PhD work. In the second chapter the structure of the proton is described. In the following one, the COMPASS experiment is presented. The forth chapter covers the Drell-Yan process and the aspects revelant to the study of TMD PDF of the proton; as a consequence it recovers topic from the second chapter and has links with it. The following chapters summarise the work done for the preparation of a proposal I am helping in writing. In particular, a data analysis of the beam tests taken in the years 2007 and 2008 is treated. Monte Carlo studies for acceptances and revelant resolutions for the Drell-Yan measurement are also presented. Finally I had the possibility to have a first look into the data collected during the test done at the end of the run of year 2009, when a geometry as close as possible to the one of the proposal has been implemented and tested in COMPASS. For the preparation of this test, in particular, I contributed with the design of the trigger, which seems to have had a good impact on the collected statistic. In fact, a first, very preliminary analysis suggests a gain of at least a factor two in the collected data with respect to the sample which was collected during the test in 2007, when the new trigger used in 2009 did not exist. Therefore a short chapter dealing with this topic is added before conclusions.

Chapter 2

The structure of the nucleon

The structure of the nucleon has been investigated by means of the Deep Inelastic Scattering (DIS). In DIS process, an electromagnetic probe (a lepton) is used to resolve the nucleon and access its constituents. Therefore it is not possible to discuss the structure of the nucleon without saying anything on DIS. Being the proton one of the two nucleons, proton and nucleon will be often used as synonyms. Structure functions describe the difference of the cross sections from those expected for point-like particles, in the case of unpolarised scattering ($\mathcal{F}_1$ and $\mathcal{F}_2$) or longitudinally polarised lepton-nucleon scattering (g_1 and g_2).
The structure functions can be expressed in terms of parton distribution functions (PDF): the momentum distribution function $q(x)$, the helicity distribution $\Delta q(x)$ and the transversity fuction $\Delta_T q(x)$. The $\mathcal{F}_{1,2}$ structure functions can be extracted in unpolarised DIS, as well as the $f(x)$. The helicity structure functions and the helicity parton distribution function can be extracted by means of polarised DIS. The transversity function, being chiral-odd, needs to be convoluted with another chiral-odd quantity in order to get an observable. This happens in Semi Inclusive Deep Inelastic Scattering (SIDIS), in which a hadron is detected in the final state in addition to the scattered lepton; in SIDIS, the transversity function appears convoluted with a chiral-odd fragmentation function.

2.1 Longitudinaly polarised Deep Inelastic Scattering

The polarised deep inelastic process involves the scattering of a longitudinally polarised lepton off a longitudinally polarised nucleon target:

$$l(k, s) + N(P, S) \rightarrow l(k', s') + X \tag{2.1}$$

where $k = (E, \mathbf{k})$, s, $k' = (E', \mathbf{k}')$, and s' are the four-momenta and spin vectors of lepton before and after scattering, P and S the four-momentum and the spin vector of the target nucleon. X is an undected hadronic system, as in DIS process only the scattered lepton is tracked. In addition M is the nucleon mass, m_l the lepton mass and the center of mass energy is $s = (l + P)^2$.

The reaction can be described choosing two invariants among the following, where lepton masses have been neglected:

- $q^2 = (k - k')^2 = -2EE'(1 - \cos\theta) \equiv -Q^2$
- $\nu = \frac{P \cdot q}{M} \overset{lab}{=} E - E'$
- the Bjorken variable $x = \frac{Q^2}{2P \cdot q} = \frac{Q^2}{2M\nu}$
- the inelasticity $y = \frac{P \cdot q}{P \cdot k}$

where θ is the scattering angle. In COMPASS, typical values of Q^2 are in the range 1-100 $(\mathrm{GeV/c^2})^2$ and the center of mass energy $s \sim 300$ GeV/c^2, the momentum of the initial lepton (a muon) being 160 GeV/c.

The DIS differential cross section to find the scattered lepton in a solid angle $\mathrm{d}\Omega$ with energy in the range $(E', E' + \mathrm{d}E')$ can be written [8, 9]

$$\frac{\mathrm{d}^2\sigma}{\mathrm{d}\Omega \mathrm{d}E'} = \frac{\alpha^2}{2Mq^4} \frac{E'}{E} L_{\mu\nu} W^{\mu\nu} \tag{2.2}$$

where α is the fine structure constant, and $L_{\mu\nu}$ and $W^{\mu\nu}$ are respectively the leptonic and the hadronic tensor. The approximation of only one photon exchange is assumed and, since in COMPASS the scattered lepton polarisation is not measured, a sum over all the lepton spin configuration in the final state will be performed.

Considering the behaviour under μ, ν interchange, both tensors can be split in a symmetric (S) and an anti-symmetric part (A), the former non depending on the spin, the latter depending on it:

$$\begin{aligned} L_{\mu\nu} &= L^{(S)}_{\mu\nu}(\mathbf{k};\mathbf{k'}) + iL^{(A)}_{\mu\nu}(\mathbf{k},\mathbf{s'};\mathbf{k'}) \\ W_{\mu\nu} &= W^{(S)}_{\mu\nu}(\mathbf{q};\mathbf{P}) + iW^{(A)}_{\mu\nu}(\mathbf{q},\mathbf{P};\mathbf{S}) \end{aligned}$$

The lepton tensor $L_{\mu\nu}$ can be calculated and its decomposed terms are:

$$\begin{aligned} L^{(S)}_{\mu\nu} &= 2\left(k_\mu k'_\nu + k_\nu k'_\mu - g_{\mu\nu} k\cdot k'\right) \\ L^{(A)}_{\mu\nu} &= 2m_l \epsilon_{\mu\nu\rho\sigma} s'^{\rho}(k-k')^\sigma \end{aligned}$$

The hadronic tensor $W_{\mu\nu}$ has no rigorous derivation since the complex structure of the nucleon prevents it. However it can be expressed by a parametrization involving two pairs of structure functions, W_1, W_2 and G_1, G_2, with only requirements of parity, time reversal and translation invariances, hermicity and gauge invariance.

$$\begin{aligned} \frac{1}{2M}W^{(S)}_{\mu\nu} = &\left(-g_{\mu\nu} + \frac{q_\mu q_\nu}{q^2}\right) W_1(P\cdot q, q^2) \\ &+ \frac{1}{M*2}\left[\left(P_\mu - \frac{P\cdot q}{q^2}q_\mu\right)\left(P_\nu - \frac{P\cdot q}{q^2}q_\nu\right)\right] W_2(P\cdot q, q^2) \end{aligned}$$

$$\begin{aligned} \frac{1}{2M}W^{(A)}_{\mu\nu} = &\epsilon_{\mu\nu\rho\sigma} q^\rho \Big\{ M S^\sigma G_1(P\cdot q, q^2) \\ &+ \frac{1}{M}\left[P\cdot q S^\sigma - S\cdot q P^\sigma\right] G_2(P\cdot q, q^2)\Big\} \end{aligned}$$

The cross section can be rewritten:

$$\frac{\mathrm{d}^2\sigma}{\mathrm{d}\Omega \mathrm{d}E'} = \frac{\alpha^2}{2Mq^4}\frac{E'}{E}\left[L^{(S)}_{\mu\nu}W^{\mu\nu(S)} - L^{(A)}_{\mu\nu}W^{\mu\nu(A)}\right] \tag{2.3}$$

The unpolarised cross section is then obtained by averaging over the spins of the incoming lepton (s) and of the nucleon (S) and reads

$$\frac{\mathrm{d}^2\sigma^{unp}}{\mathrm{d}\Omega \mathrm{d}E'} = \frac{1}{4}\sum_{s',S}\frac{\mathrm{d}^2\sigma}{\mathrm{d}\Omega \mathrm{d}E'} = \frac{\alpha^2}{2Mq^4}\frac{E'}{E}L^{(S)}_{\mu\nu}W^{\mu\nu(S)} \tag{2.4}$$

Computing the product of $L_{\mu\nu}^{(S)}$ and $W_{\mu\nu}^{(S)}$ one gets the well-known expression:

$$\frac{\mathrm{d}^2\sigma^{unp}}{\mathrm{d}\Omega\mathrm{d}E'} = \frac{4\alpha^2 E'^2}{q^4}\left[2W_1 \sin^2\frac{\theta}{2} + W_2\cos^2\frac{\theta}{2}\right] \tag{2.5}$$

The two unpolarised structure functions W_1 and W_2 are known to approximately scale, in the Bjorken limit ($Q^2 \to \infty$, x finite):

$$\begin{aligned} MW_1(P\cdot q, q^2) &\to \mathcal{F}_1(x) \\ \nu W_2(P\cdot q, q^2) &\to \mathcal{F}_2(x) \end{aligned} \tag{2.6}$$

and that means that $\mathcal{F}_{1,2}(x)$ change very slowly with Q^2 at fixed x. The $\mathcal{F}_{1,2}$ describe the deviation from the cross section for the scattering of a spin-$\frac{1}{2}$ particle off a spin-$\frac{1}{2}$ point like constituent and they correspond to the electrical and magnetic form factor in lepton-nucleon elastic scattering. Fig. 2.1 shows how well $\mathcal{F}_2$ is known. To access the polarised structure functions G_1 and G_2, the difference of cross sections with opposite target spins with respect to the lepton incoming direction has to be computed to single out the anti-symmetric term of the cross section:

$$\frac{\mathrm{d}^2\sigma^{s,S}}{\mathrm{d}\Omega\mathrm{d}E'} - \frac{\mathrm{d}^2\sigma^{s,-S}}{\mathrm{d}\Omega\mathrm{d}E'} = -\frac{\alpha^2}{2Mq^4}\frac{E'}{E}4L_{\mu\nu}^{(A)}W^{\mu\nu(A)} \tag{2.7}$$

With similar computations to the ones used for the unpolarised cross section, considering only longitudinally polarised leptons, with spin along ($\rightarrow$) or opposite ($\leftarrow$) to the direction of motion, and the nucleon at rest, polarised in the same ($\Rightarrow$) or opposite ($\Leftarrow$) direction of motion of the lepton, one gets:

$$\frac{\mathrm{d}^2\sigma^{\overset{\rightarrow}{\Rightarrow}}}{\mathrm{d}\Omega\mathrm{d}E'} - \frac{\mathrm{d}^2\sigma^{\overset{\rightarrow}{\Leftarrow}}}{\mathrm{d}\Omega\mathrm{d}E'} = -\frac{4\alpha^2}{Q^2}\frac{E'}{E}\left[\left(E + E'\cos\theta\right)M\frac{\nu}{(P\cdot q)^2}g_1 - Q^2\frac{g_2}{\nu(P\cdot q)}\right] \tag{2.8}$$

where the two polarised structure functions $g_1(x)$ and $g_2(x)$ have been introduced, as G_1 and G_2 show a scaling behaviour in the Bjorken limit:

$$\begin{aligned} M^2\nu G_1(P\cdot q, q^2) &\to g_1(x) \\ M\nu^2 G_2(P\cdot q, q^2) &\to g_2(x) \end{aligned} \tag{2.9}$$

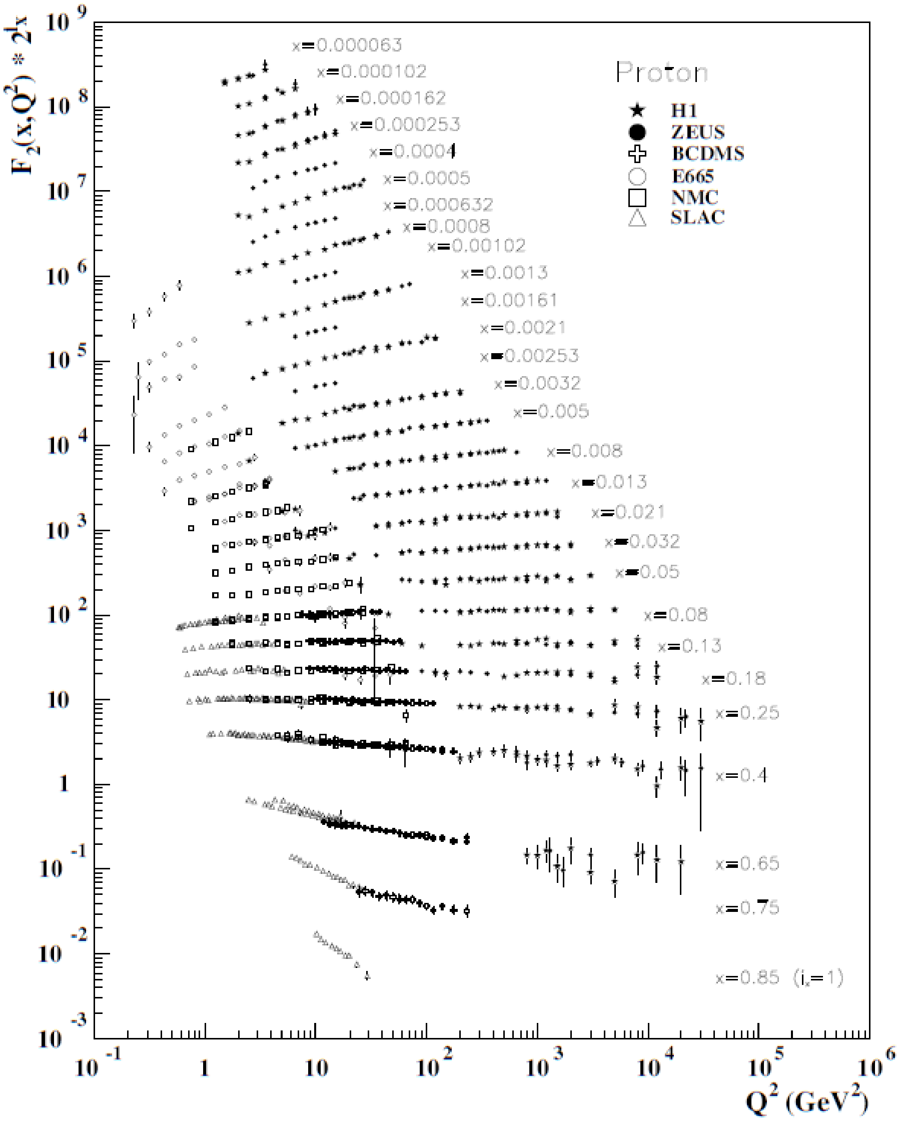

Figure 2.1: The proton structure function F_2^p measured in electromagnetic scattering of positrons on protons (experiment ZEUS [10, 11] and H1 [12, 13] at HERA), for $x > 0.00006$, and for electrons (SLAC [14]) and muons (BCDMS [15], E665 [16], NMC [17]) on a fixed target. Statistical and systematic errors added in quadrature are shown. The data are plotted as a function of Q^2 in bins of x. For clarity, F_2^p has been multiplied by 2^{i_x}, where i_x is the number of the x bin, ranging from $i_x = 1$ ($x = 0.85$) to $i_x = 28$ ($x = 0.000063$). The figure has been taken from [18].

If nucleons are transversely polarised ($\Uparrow$ and $\Downarrow$ define the two possible directions), the cross section is given by:

$$\frac{\mathrm{d}^2\sigma^{\rightarrow\Uparrow}}{\mathrm{d}\Omega\mathrm{d}E'} - \frac{\mathrm{d}^2\sigma^{\rightarrow\Downarrow}}{\mathrm{d}\Omega\mathrm{d}E'} = -\frac{4\alpha^2}{Q^2}\frac{E'}{E}\sin\theta\cos\phi\left(M\frac{\nu}{(P\cdot q)^2}g_1 + 2E\frac{g_2}{\nu(P\cdot q)}\right) \quad (2.10)$$

where ϕ is the azimuthal angle between the scattering plane and the polarisation plane. The two polarised structure functions g_1 and g_2, however, are not directly measured through cross sections, but from measured asymmetries. In experiments using a longitudinally polarised target the longitudinal spin-spin asymmetry is defined as:

$$A_{\parallel} \equiv \frac{\mathrm{d}\sigma^{\rightrightarrows} - \mathrm{d}\sigma^{\rightleftarrows}}{\mathrm{d}\sigma^{\rightrightarrows} + \mathrm{d}\sigma^{\rightleftarrows}} \quad (2.11)$$

and, if target is transversely polarised, the following asymmetry can be extracted:

$$A_{\perp} \equiv \frac{\mathrm{d}\sigma^{\rightarrow\Uparrow} - \mathrm{d}\sigma^{\rightarrow\Downarrow}}{\mathrm{d}\sigma^{\rightarrow\Uparrow} + \mathrm{d}\sigma^{\rightarrow\Downarrow}} \quad (2.12)$$

From both asymmetries, informations on g_1 and g_2 can be extracted, but since in expression 2.8 the term depending on g_2 is suppressed by a factor M/E, g_1 can be extracted from $A_{\parallel}$ and knowing g_1, g_2 can be extracted from $A_{\perp}$.

2.1.1 The Parton Model

The structure functions can have a simple interpretation in the framework of the parton model (PM), in which hadrons are made of discrete elementary constituents, the partons. Such a model was suggested by the observation of the scaling behaviour of the $\mathcal{F}_1$ and $\mathcal{F}_2$ structure functions, which are consistent with a model of a nucleon composed of point-like constituents. In the infinite momentum frame, where the nucleon moves with a very large momentum in one direction, partons are considered massless and carry a fraction x of the nucleon momentum. x is the familiar Bjorken variables and the collinear approximation is assumed since transverse momenta are neglected. Moreover partons are considered quasi-free, that means that they do not interact between them but only with an external probe. In the 1970s, the charged partons in the nucleon were unambiguously identified with the quarks, proposed in 1964 to explain the hadron spectrum. In this framework,

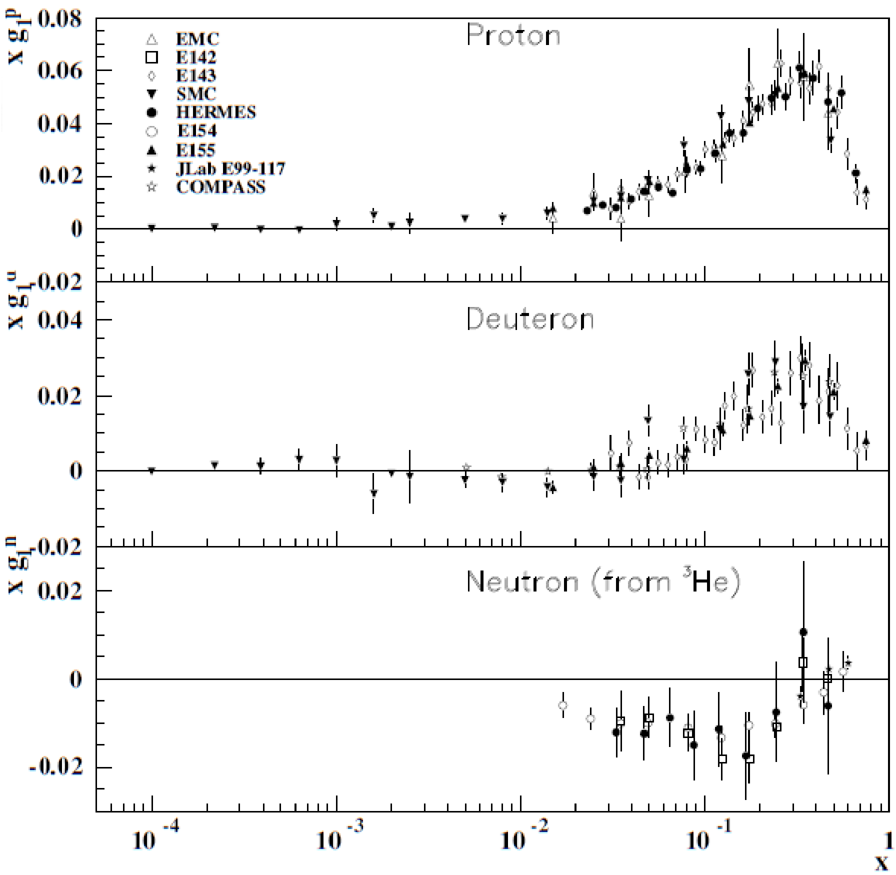

Figure 2.2: The spin-dependent structure function $xg_1(x)$ of the proton (top), deuteron (middle) and neutron (bottom) measured in deep inelastic scattering of polarised electron/positrons (E142 [19] ($Q^2 \sim 0.3 - 10GeV^2$), E143 [20] ($Q^2 \sim 0.3 - 10GeV^2$), E154 [21] ($Q^2 \sim 1 - 17GeV^2$), E155 [22, 23] ($Q^2 \sim 1 - 40GeV^2$), JLab E99-117 [24] ($Q^2 \sim 2.71 - 4.83GeV^2$), HERMES [25, 26] ($Q^2 \sim 0.8 - 20GeV^2$)) and muons (EMC [1] ($Q^2 \sim 1.5 - 100GeV^2$), SMC [27, 28] ($Q^2 \sim 0.01 - 100GeV^2$), COMPASS [29] $Q^2 \sim 1 - 100GeV^2$)) shown at the measured Q^2 (except for EMC data given at $Q^2 = 10.7$ GeV^2 and E155 data given at $Q^2 = 5$ GeV^2. Statistical errors are added in quadrature. The figure has been taken from [18].

the parton densities $q(x)$ are introduced for each quark flavour q, carrying momentum xP; they are the partons distribution functions (PDF). DIS can be understood as the incoherent sum of elastic scattering of the probe on the constituents and the structure function $\mathcal{F}_2$ has a simple interpretation:

$$\mathcal{F}_2(x) = \sum_q e_q^2 x q(x) \tag{2.13}$$

In the parton model, the $\mathcal{F}_1$ is connected with the $\mathcal{F}_2$ trought the Callan-Gross relationship [30]:

$$2x\mathcal{F}_1(x) = \mathcal{F}_2(x) \tag{2.14}$$

The Callan-Gross relation is a prediction of the model, because of the $\frac{1}{2}$-spin of the quarks. In other word, the structure functions can be intepreted in terms of probability to find a quark with a fraction x of the nucleon momentum.

When one computes the integral $\sum_q \int_0^1 xq(x)$ to obtain the total momentum carried from the partons, one expects to get 1. However experimental data from proton and neutron give back a value of about 0.5, thus suggesting that the contribution of u and d quark is not sufficient and other partons are present in the nucleon. These partons do not interact with the incoming charged lepton, therefore they must be electrically neutral: they are the gluons, the mediators of the force between two quarks. Their density in a nucleon is usually indicated as $G(x)$.

In the PM, one can introduce another PDF, Δq, to give g_1 a simple intepretation and it can be decomposed in terms of parton contributions, partons with spin parallel to the longitudinal nucleon spin ($q(x, s; S)$) or antiparallel ($q(x, -s; S)$):

$$g_1(x) = \frac{1}{2}\sum_q e_q^2 \left[q(x, s; S) - q(x, -s; S)\right] = \frac{1}{2}\sum_q e_q^2 \Delta q(x, S) \tag{2.15}$$

A partonic intepretation of g_2 does not exist.

The first moment of g_1 of the proton and of the neutron can be expressed as:

$$\begin{aligned}\Gamma_1^{p,n} &= \int_0^1 \mathrm{d}x g_1^{p,n}(x) = \\ &= \pm\frac{1}{12}(\Delta u - \Delta d) + \frac{1}{36}(\Delta u + \Delta d - 2\Delta s) + \frac{1}{9}(\Delta u + \Delta d + \Delta s)\end{aligned} \tag{2.16}$$

where $\Delta q = \int_0^1 \Delta q(x)$ are the first moments of the quark helicity distributions $\Delta q(x, Q^2)$. The three terms in Eq. 2.16 can are identified as:

$$a_3 = \Delta u - \Delta d \tag{2.17}$$

$$a_8 = \frac{1}{\sqrt{3}} (\Delta u + \Delta d - 2\Delta s) \tag{2.18}$$

$$a_0 = \Delta u + \Delta d + \Delta s \tag{2.19}$$

a_3 and a_8 can be obtained from data on baryon β-decay. From Eq. 2.16, a fundamental sum rule for QCD, the Bjorken sum rule, can be obtained:

$$\Gamma_1^p - \Gamma_1^n = \frac{1}{6} a_3 = \frac{1}{6} \left| \frac{g_A}{g_V} \right| \tag{2.20}$$

where g_A and g_V are the axial and vector coupling costants in the neutron β-decay. The EMC and SMC experiment measured respectively Γ_1^p [31] and Γ_1^n [27], allowing a first check of the Bjorken sum rule. It has been found consistent with its expectation value, predicted using the known value of a_3. Another sum rule exists, in the assumption of $\Delta s = \Delta \bar{s} = 0$, which implies $a_0 = \sqrt{3} a_8$: the Ellis-Jaffe rule. It is derived from Eq. 2.16:

$$\Gamma_1^{p,n} = \frac{1}{12} a_3 \left\{ \pm 1 + \frac{5}{\sqrt{3}} \cdot \frac{a_8}{a_3} \right\} \tag{2.21}$$

Nevertheless, the value of Γ_1^p from EMC indicated a large violation of the Ellis-Jaffe sum rule, and therefore the assumption of $\Delta s = \Delta \bar{s} = 0$ is not correct. Γ_1^p is used to extract the a_0 term and also each contribution Δu, Δd and Δs. All these terms should contribute to the spin of the nucleon, $\Delta\Sigma$, being in the parton model the result of the sum of the contribution of all quarks.
The total nucleon spin is:

$$S_z = \frac{1}{2} \sum_q \Delta q = \frac{\Delta\Sigma}{2} \tag{2.22}$$

From Eq. 2.19, a_0 appears to coincide with $\Delta\Sigma$, and therefore, being the spin of the nucleon $\frac{1}{2}$, a_0 is expected to be 1. But EMC measured a value

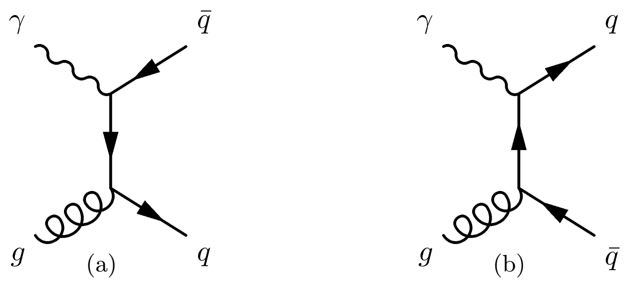

Figure 2.3: Diagrams contributing to the mixing between g_1^p and the polarised gluon parton density.

compatible with zero:

$$a_0 = 0.06 \pm 0.12 \pm 0.17 \tag{2.23}$$

That was a big surprise and the beginning of the so-called *spin crisis*. Again, like for the total momentum carried by the quarks, something appears to be missing, and that can be easily identified with gluons. Gluons do not interact with the electromagnetic probe, but they can give rise to QCD corrections which depends on Q^2, leading to a violation of the Bjorken scaling. As the resolution increases with Q^2, parton distribution functions vary and the number of resolved partons increases. The evolution of quark structure functions is described by the DGLAP equations, which express gluon emission/absorption and $q\bar{q}$ pairs creation. In QCD, a contribution with a non zero value can come from gluon-photon-fusion diagram (see Fig. 2.3) [32], that corrects the value of a_0 in the following way:

$$a_0(Q^2) = \Delta\Sigma - 3\frac{\alpha_s(Q^2)}{2\pi}\Delta G(Q^2) \tag{2.24}$$

where $\alpha_s(Q^2)$ is the strong coupling and $\Delta G(Q^2) = G^{\rightrightarrows}(Q^2) - G^{\rightleftarrows}(Q^2)$ the gluon contribution to the nucleon spin. Eq. 2.24 states that, if a_0 is small, it is not necessary that $\Delta\Sigma$ is small, and that a cancellation can occur due to an anomalous gluonic contribution. ΔG is not a vanishing correction at high Q^2, because it behaves like $1/\alpha_s$ when $Q^2 \to \infty$.
Therefore the spin of the nucleon receives more contribution and it can be

rewritten:

$$S_z = \frac{1}{2} = \frac{1}{2}\Delta\Sigma + \Delta G + \langle L_z \rangle \tag{2.25}$$

where both the contributions of quarks and gluons have been included as well as a term arising from their orbital angular momentum $\langle L_z \rangle$.

2.1.2 Transversity

In the previous section, two PDFs have been introduced, $q(x)$ and $\Delta q(x)$. At leading order, a third PDF has to be considered to describe the spin structure of the nucleon; this additional distribution is the quark transverse polarisation distribution Δq_T, called transversity. A naïve way to understand why it is needed can be found in the fact that rotations and Lorentz boost do not commute. In fact, the description of the nucleon is done in the infinite momentum frame, where it moves along a direction; its spin can be aligned along this direction or be perpendicular and therefore a longitudinal description of its spin and a transverse one exist.

Transversity was introduced by Ralston and Soper in 1979 in a work about Drell-Yan processes in proton-proton collisions [5]. It was forgotten for many years and rediscovered in the nineties by Artru and Mekhfi [6] and Jaffe and Ji [33]. Since then great interest has grown, both from the theoretical and from the experimental point of view.

A simple understanding of transversity can be found in the following. The optical theorem relates the hadronic tensor to forward virtual Compton scattering amplitudes [34]. Thus leading-twist quark distribution functions can be expressed in terms of quark-nucleon forward amplitudes. In the helicity basis these amplitudes have the form $\mathcal{A}_{\Lambda,\lambda,\Lambda',\lambda'}$, where λ, λ' (Λ, Λ') are quark (nucleon) helicities. These are in general 16 amplitudes. Imposing helicity conservation, parity and time invariance, only three independent amplitudes (see Fig. 2.4) survive:

$$\mathcal{A}_{++,++}, \quad \mathcal{A}_{+-,+-}, \quad \mathcal{A}_{+-,-+} \tag{2.26}$$

Two of the amplitudes, $\mathcal{A}_{++,++}$ and $\mathcal{A}_{+-,+-}$, are diagonal in the helicity basis (the quark does not flip its helicity: $\lambda = \lambda'$); the third, $\mathcal{A}_{+-,-+}$, is off-diagonal (helicity flips: $\lambda = -\lambda'$). Using the optical theorem we can relate these quark-nucleon helicity amplitudes to the three leading-twist quark

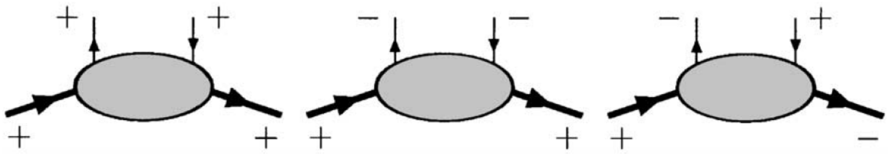

Figure 2.4: The three quark-nucleon helicity amplitudes.

distribution functions, according to the scheme:

$$\begin{aligned} q(x) &= q_+(x) + q_-(x) \sim Im(\mathcal{A}_{++,++} + \mathcal{A}_{+-,+-}) \\ \Delta q(x) &= q_+(x) - q_-(x) \sim Im(\mathcal{A}_{++,++} - \mathcal{A}_{+-,+-}) \\ \Delta_T q(x) &= q_\uparrow(x) - q_\downarrow(x) \sim Im(\mathcal{A}_{+-,-+}) \end{aligned}$$

The probabilistic interpretation is manifest for $q(x)$ and $\Delta f(x)$, while it is not so for $\Delta_T q(x)$. In a transversity basis, with $\uparrow$ transverse with respect to the direction of motion,

$$\begin{aligned} |\uparrow\rangle &= \frac{1}{\sqrt{2}}\left[+\rangle + i|-\rangle\right] \\ |\downarrow\rangle &= \frac{1}{\sqrt{2}}\left[+\rangle - i|-\rangle\right] \end{aligned}$$

then $\Delta_T q(x)$ reads:

$$\Delta_T q(x) = q_\uparrow(x) - q_\downarrow(x) \sim Im(\mathcal{A}_{\uparrow\uparrow,\uparrow\uparrow} - \mathcal{A}_{\uparrow\downarrow,\uparrow\downarrow})$$

leading to the interpretation of $\Delta_T q(x)$ as the polarised quark distribution in a nucleon transversely polarised with respect to its momentum.
Reasoning in terms of parton-nucleon forward helicity amplitudes, it is easy to understand why there is no such thing as leading-twist transverse polarisation of gluons. A hypothetical $\Delta_T G$ would imply an helicity flip gluon-nucleon amplitude, which cannot occour due to helicity conservation. One remark has to be done: if the collinear approximation is dropped, thus recovering the transverse momentum of quarks, the situation becomes more complicated and the number of independent helicity amplitudes increases. These amplitudes combine to form eight k_T-dependent functions (three of which reduce to $q(x)$, $\Delta q(x)$ and $\Delta_T q(x)$).
The transversity function is a chiral-odd quantity that requires the helicity

of the quark to be flipped. All the hard processes conserve the helicity, and as a consequence $\Delta_T f(x)$ cannot be measured in inclusive DIS. It has to be measured in process where it appears convoluted with another chiral-odd quantity. This happens in Semi Inclusive Deep Inelastic Scattering (SIDIS) processes where the transversity function is multiplied by a chiral-odd fragmentation function (see Sec 2.2).

2.1.3 Soffer inequality

From the definition of q, Δq and $\Delta_T q$, two bounds on Δq and $\Delta_T q$ can be derived:

$$|\Delta q(x)| \leq q(x)$$
$$|\Delta_T q(x)| \leq q(x)$$

and similar inequalities are satisfied by the antiquark distributions. Another bound, simultaneously involving q, Δq and $\Delta_T q$, was discovered by Soffer [35]:

$$q(x) + \Delta q(x) \geq 2|\Delta_T q| \tag{2.27}$$

This relationship is known as the Soffer inequality. It is an important bound, which must be satisfied by the leading-twist distribution functions.

2.2 Polarised SIDIS

The SIDIS process offers the possibility to measure the transversity function. Its cross section can be expressed in terms of transverse momentum dependent distribution functions and fragmentation functions D that explicitly depend on the transverse parton momentum $\mathbf{k}_T$, with respect to the nucleon direction and on the transverse momentum $\mathbf{p}_T$ of the final state hadron with respect to the fragmenting quark direction. These partonic functions, usually indicated as unintegrated functions, are a generalization of the distributions appearing in standard factorization for the collinear case, in which both $\mathbf{k}_T$ and $\mathbf{p}_T$ are ignored. A common choice for the reference frame where the SIDIS cross section is described is the *gamma-nucleon system* (GNS), where the virtual photon direction defines the z axis, and the xz plane is the lepton scattering plane (defined by the initial and final lep-

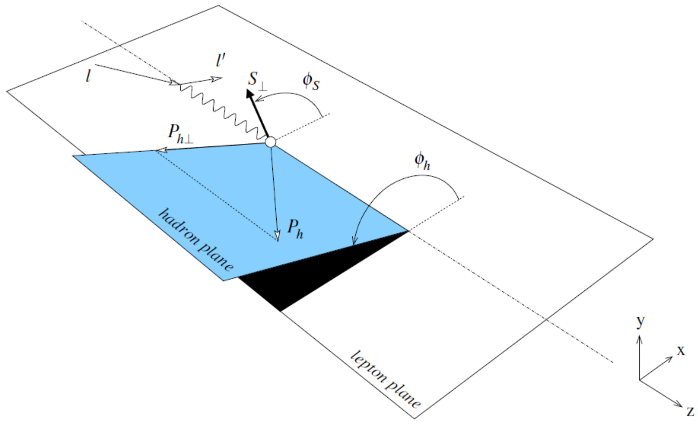

Figure 2.5: Definition of the azimuthal angles ϕ_h and ϕ_S in the *gamma-nucleon system.*

ton momenta). The polarised SIDIS cross section depends on the azimuthal angle ϕ_h of the produced hadron with respect to the scattering plane and on the azimuthal angle ϕ_S of the target nucleon spin. At Born level, with spinless hadrons in final state, the polarised SIDIS cross section is [36]:

$$
\begin{aligned}
&\frac{\mathrm{d}\sigma}{\mathrm{d}x\mathrm{d}y\mathrm{d}\phi_S\mathrm{d}z\mathrm{d}\phi_h\mathrm{d}P_T^h} = \\
&\frac{\alpha^2}{xyQ^2}\frac{y^2}{2(1-\epsilon)}\left(1+\frac{\gamma^2}{2x}\right)\Bigg\{F_{UU,T}+\epsilon F_{UU,L}+\sqrt{2\epsilon\,(1+\epsilon)}\cos\phi_h F_{UU}^{\cos\phi_h} \\
&+\epsilon\cos\left(2\phi_h\right)F_{UU}^{\cos 2\phi_h}+\lambda_e\sqrt{2\epsilon\,(1-\epsilon)}\sin\phi_h F_{LU}^{\sin\phi_h} \\
&+S_{\|}\left[\sqrt{2\epsilon\,(1+\epsilon)}\sin\phi_h F_{UL}^{\sin\phi_h}+\epsilon\sin(2\phi_h)F_{UL}^{\sin(2\phi_h)}\right] \\
&+S_{\|}\lambda_e\left[\sqrt{1-\epsilon^2}F_{LL}+\sqrt{2\epsilon\,(1-\epsilon)}\cos\phi_h F_{LL}^{\cos\phi_h}\right] \\
&+S_{\perp}\Bigg[\sin\left(\phi_h-\phi_S\right)\left(F_{UT,T}^{\sin(\phi_h-\phi_S)}+\epsilon F_{UT,L}^{\sin(\phi_h-\phi_S)}\right) \\
&+\epsilon\sin(\phi_h+\phi_S)F_{UT}^{\sin(\phi_h+\phi_S)}+\epsilon\sin(3\phi_h-\phi_S)F_{UT}^{\sin(3\phi_h-\phi_S)} \\
&\sqrt{2\epsilon\,(1+\epsilon)}\sin\phi_S F_{UT}^{\sin\phi_S}+\sqrt{2\epsilon\,(1+\epsilon)}\sin(2\phi_h-\phi_S)F_{UT}^{\sin(2\phi_h-\phi_S)}\Bigg]
\end{aligned}
$$

$$+ S_{\perp}\lambda_e\left[\sqrt{1-\epsilon^2}\cos(\phi_h-\phi_S)F_{LT}^{\cos(\phi_h-\phi_S)} + \sqrt{2\epsilon\,(1-\epsilon)}\cos\phi_S F_{LT}^{\cos\phi_S} \right.$$
$$\left.\left. + \sqrt{2\epsilon\,(1-\epsilon)}\cos(2\phi_h-\phi_S)F_{LT}^{\cos(2\phi_h-\phi_S)}\right]\right\} \tag{2.28}$$

where λ_e is the helicity of the lepton beam, $S_{\parallel}$ and $S_{\perp}$ are respectively the projections of the target polarisation in the plane parallel or transverse with respect to the photon direction, ϵ is the ratio of longitudinal and transverse photon flux which is given by:

$$\epsilon = \frac{1-y-\frac{1}{4}\gamma^2 y^2}{1-y+\frac{1}{2}y^2+\frac{1}{4}\gamma^2 y^2} \tag{2.29}$$

where $\gamma = \frac{2Mx}{Q} \sim 0$, and it will be neglected in the following; P_T^h is the transverse momentum of the final state hadron with respect to the photon direction. The structure functions F which appears in Eq. 2.28 depend on x, Q^2 and P_T^h; their first and second subscript indicate the respective polarisation of beam and target (U = unpolarised, L = longitudinal, T = transverse), while the third subscript, when is present, specifies the polarisation of the virtual photon. The superscript of F indicates the different azimuthal modulation in ϕ_h and ϕ_S.
Eq. 2.28 shows eighteen structure functions that can be singularly extracted, as they are all multiplied by a different cosine or sine function of ϕ_h, ϕ_S or a linear combination of them. When Eq. 2.28 is multiplied by one of these functions and integrated over the angle, the result is only the specific F times a constant. In this way it is possible to access each structure function.

2.3 Transverse momentum dependent PDF

In the SIDIS cross section, written explicitly in the previous section, eighteen structure fuctions appears. Their expression can be found in [34], where the SIDIS cross section is factorized into the hard photon-quark scattering process, transverse momentum dependent (TMD) parton distribution functions and TMD fragmentation functions.
The TMD PDFs are eight, corresponding to the eight forward Compton scattering amplitudes presented in Subsec. 2.1.2, and they are listed in Tab. 2.1.

The letters f, g and h refer respectively to unpolarised, longitudinal and transversely polarised quark distributions. The subscript 1 means that they are leading-twist quantities; the subscripts L and T mean that the target nucleon is longitudinally or transversely polarised; the superscript $\perp$ indicates the presence of transverse momentum effect. The structure functions

PDF	meaning
$f_1(x, \mathbf{k}_T^2)$	unpolarised distribution
$g_{1L}(x, \mathbf{k}_T^2)$	helicity distribution
$g_{1T}(x, \mathbf{k}_T^2)$	distribution of longitudinally polarised quarks in transversely polarised nucleon
$f_{1T}^{\perp}(x, \mathbf{k}_T^2)$	Sivers distribution: distribution of quarks in a transversely polarised nucleon
$h_{1T}(x, \mathbf{k}_T^2)$	quark transverse polarisation along nucleon transverse polarisation
$h_{1L}^{\perp}(x, \mathbf{k}_T^2)$	quark transverse polarisation in the longitudinally polarised nucleon
$h_{1T}^{\perp}(x, \mathbf{k}_T^2)$	quark transverse polarisation in the transversely polarised nucleon
$h_1^{\perp}(x, \mathbf{k}_T^2)$	Boer-Mulders distribution: quark transverse polarisation in an unpolarised nucleon

Table 2.1: The eight leading twist TMD PDF.

in Eq. 2.28 are related to the TMD PDF by a convolution:

$$\mathcal{C}[wfD] = x \sum_a e_a^2 \int \mathrm{d}^2\mathbf{k}_T \mathbf{p}_T \delta^2 \left(\mathbf{k}_T - \mathbf{p}_T - \frac{\mathbf{P}_T}{z} \right) \cdot w(\mathbf{p}_T, \mathbf{k}_T) f_a(x, k_T^2) D_a(z, p_T^2) \tag{2.30}$$

where f D are generic parton distribution functions and fragmentation functions, $w(\mathbf{p}_T, \mathbf{k}_T)$ is a function depending of the transverse momenta and the summation runs over quarks and anti-quarks; the δ function enforces transverse momentum conservation.

With Eq. 2.30, one can show that eight transverse structure functions of Eq. 2.28 can be expressed via the eight leading twist PDFs:

$$F_{UU,T} = \mathcal{C}\left[f_1 D \right] \tag{2.31}$$

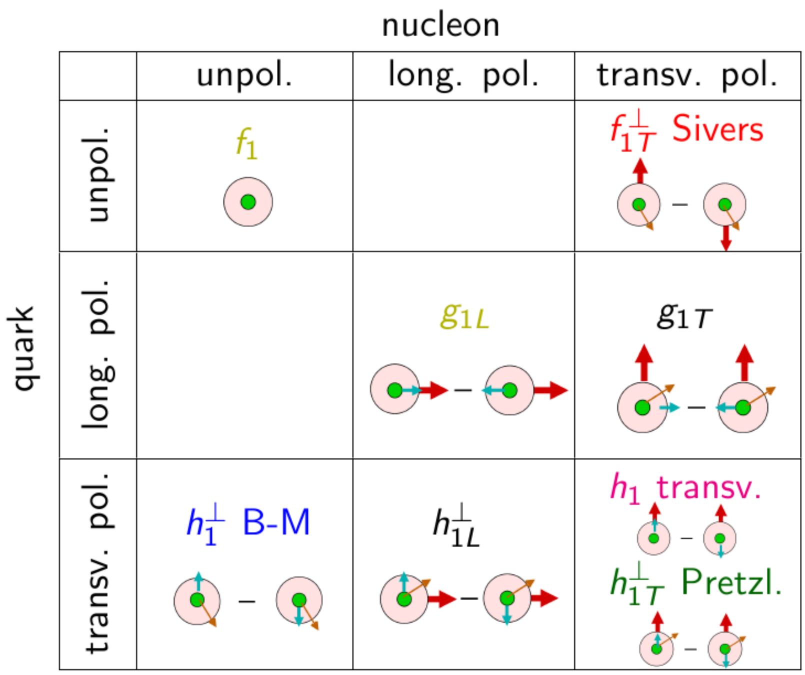

Figure 2.6: TMD PDF organised in a table: rows and columns refer to different polarisation states of quarks and nucleon.

$$F_{UT}^{\sin(\phi_h+\phi_S)} = \mathcal{C}\left[-\frac{\hat{h}\cdot\mathbf{p}_T}{M_h}h_1 H_1^{\perp}\right] \tag{2.32}$$

$$F_{UT,T}^{\sin(\phi_h-\phi_S)} = \mathcal{C}\left[-\frac{\hat{h}\cdot\mathbf{k}_T}{M}f_{1T}^{\perp}D\right] \tag{2.33}$$

$$F_{UT}^{\sin(3\phi_h-\phi_S)} = \mathcal{C}\left[\frac{2(\hat{h}\cdot\mathbf{p}_T)(\mathbf{k}_T\cdot\mathbf{p}_T)+\mathbf{k}_T^2(\hat{h}\cdot\mathbf{p}_T)-4(\hat{h}\cdot\mathbf{k}_T)^2(\hat{h}\cdot\mathbf{p}_T)}{2M^2M_h}h_{1T}^{\perp}H_1^{\perp}\right] \tag{2.34}$$

$$F_{LT}^{\cos(\phi_h-\phi_S)} = \mathcal{C}\left[\frac{\hat{h}\cdot\mathbf{k}_T}{M}g_{1T}D\right] \tag{2.35}$$

$$F_{LL} = \mathcal{C}\left[g_{1L}D_1\right] \tag{2.36}$$

$$F_{UU}^{\cos 2\phi_h} = \mathcal{C}\left[-\frac{2(\hat{h}\mathbf{k}_T)(\hat{h}\mathbf{p}_T)-\mathbf{k}_T\cdot\mathbf{p}_T}{MM_h}h_1^{\perp}H_1^{\perp}\right] \tag{2.37}$$

$$F_{UL}^{\sin 2\phi_h} = \mathcal{C}\left[-\frac{2(\hat{h}\mathbf{k}_T)(\hat{h}\mathbf{p}_T)-\mathbf{k}_T\cdot\mathbf{p}_T}{MM_h}h_{1L}^{\perp}H_1^{\perp}\right] \tag{2.38}$$

where $\hat{h} = \frac{\mathbf{P}_T^h}{|P_T^h|}$ and $H_1^\perp$ is the Collins fragmentation function, which describes the spin-dependent part of the fragmentation. Eq. 2.31 contains the unpolarised parton distribution function f_1 and the unpolarised fragmentation function D. Eq. 2.32 is related to the Collins effect [37]: it contains the transversity function h_1 defined as:

$$h_1(x, k_T^2) = h_{1T}(x, k_T^2) - \frac{k_T^2}{2M_2} h_{1T}^\perp(x, k_T^2) \tag{2.39}$$

which, when integrated over $\mathbf{k}_T$, gives back the already introduced transversity function:

$$\Delta_T f_(x) \equiv h_1(x) = \int \mathrm{d}^2\mathbf{k}_T h_1(x, k_T^2) \tag{2.40}$$

Eq. 2.33 describes the Sivers effect [38] and it contains the Sivers function $f_{1T}^\perp$ which is convoluted with the fragmentation function D. In Eq. 2.37 the Boer-Mulders function appears convoluted with $H_1^\perp$.

2.3.1 Naïve T-odd TMD PDF

In the following a short description of naïve T-odd transverse momentum dependent parton distribution functions is provided: the Sivers function $f_{1T}^\perp$ [38, 39] and the Boer-Mulder function $h_1^\perp$ [40]. This two new distributions have also a partonic interpretation. $f_{1T}^\perp$ is related to the number density of unpolarised quarks in a transversely polarised nucleon and it is given by:

$$\begin{aligned}\mathcal{P}_{q/N_\uparrow}(x, \mathbf{k}_T) - \mathcal{P}_{q/N_\downarrow}(x, \mathbf{k}_T) &= \mathcal{P}_{q/N_\uparrow}(x, \mathbf{k}_T) - \mathcal{P}_{q/N_\uparrow}(x, -\mathbf{k}_T) \\ &= -2\frac{|\mathbf{k}_T|}{M} \sin(\phi_k - \phi_S) f_{1T}^\perp(x, \mathbf{k}_T^2)\end{aligned} \tag{2.41}$$

The Boer-Mulder function measures the quark transverse polarisation in an unpolarised hadron and it is defined by:

$$\mathcal{P}_{q_\uparrow/N}(x, \mathbf{k}_T) - \mathcal{P}_{q_\downarrow/N}(x, \mathbf{k}_T) = -\frac{|\mathbf{k}_T|}{M} \sin(\phi_k - \phi_s) h_1^\perp(x, \mathbf{k}_T^2) \tag{2.42}$$

$(\phi_k - \phi_S)$ and $(\phi_k - \phi_s$ are the relative azimuthal angle between the target spin $\mathbf{S}_\perp$ and the quark transverse momentum $\mathbf{k}_T$ and the relative azimuthal angle between the quark spin and its transverse momentum $\mathbf{k}_T$.
For later convenience, let us define two quantities, $\Delta_0^T f$ and $\Delta_T^0 f$, which are

related to $f_{1T}^{\perp}$ and $h_1^{\perp}$, respectively by:

$$\Delta_0^T f(x, \mathbf{k}_T^2) \equiv -2\frac{\mathbf{k}_T}{M} f_{1T}^{\perp} \tag{2.43}$$

$$\Delta_T^0 f(x, \mathbf{k}_T^2) \equiv -\frac{\mathbf{k}_T}{M} h_1^{\perp} \tag{2.44}$$

The Sivers function can be accessed via SIDIS and Drell-Yan (DY) processes. The DY way will be discussed in Chap. 4 and in particular in Subsection 4.7.1. The SIDIS process allows to access the Sivers function by looking at the asymmetry of cross section. In the assumption that the hadron produced in the fragmentation and the fragmenting quark are collinear, so that the transverse momentum originates only from the intrinsic transverse momentum of the quark in the nucleon ($\mathbf{P}_T^h = z\mathbf{k}_T$), the SIDIS cross section with the unpolarised and the Sivers term of Eq. 2.28 reduces to:

$$\begin{aligned}\frac{\mathrm{d}\sigma}{\mathrm{d}x\mathrm{d}y\mathrm{d}\phi_S\mathrm{d}z\mathrm{d}\phi_h\mathrm{d}P_T^h} = \frac{\alpha^2}{xyQ^2}\sum_q \frac{e_q^2}{2}\left[1+(1+y)^2\right]\cdot x\cdot y \\ \left[f(x, \frac{P_T^{h^2}}{z^2}) + S_\perp \sin\Phi_S \Delta_0^T f(x, \frac{P_T^{h^2}}{z^2})\right]\cdot D_q^h(z)\end{aligned} \tag{2.45}$$

where the Sivers angle is $\Phi_S = \phi_h - \phi_S$ and the $D_q^h(z)$ are the fragmentation functions describing the probability of a quark q to hadronize in a hadron h. Then, by comparing the cross sections with oppositely polarised target nucleons, one obtains the transverse spin asymmetry:

$$A_T^h \equiv \frac{\mathrm{d}\sigma(\mathbf{S}_\perp) - \mathrm{d}\sigma(-\mathbf{S}_\perp)}{\mathrm{d}\sigma(\mathbf{S}_\perp) + \mathrm{d}\sigma(-\mathbf{S}_\perp)} = S_\perp \cdot A_{Siv}\sin\Phi_S \tag{2.46}$$

where the Sivers asymmetry is:

$$A_{Siv} \simeq \frac{\sum_q e_q^2 \cdot x \cdot \Delta_0^T f(x, \frac{P_T^{h^2}}{z^2}) \cdot D_q^h(z)}{\sum_q e_q^2 \cdot x \cdot f(x, \frac{P_T^{h^2}}{z^2}) \cdot D_q^h(z)} \tag{2.47}$$

The Boer-Mulders function can be accessed with Drell-Yan processes and the discussion can be found in Chap. 4.
From theoretical argumentations [41], in QCD, an expectation exists for the Sivers and the Boer-Mulders functions, whether they are accessed via DIS

or Drell-Yan processes:

$$f_{1T}^{\perp}(x, \mathbf{k}_T^2)|_{SIDIS} = -f_{1T}^{\perp}(x, \mathbf{k}_T^2)|_{DY} \tag{2.48}$$

$$h_1^{\perp}(x, \mathbf{k}_T^2)|_{SIDIS} = -h_1^{\perp}(x, \mathbf{k}_T^2)|_{DY} \tag{2.49}$$

2.3.2 Experimental overview

Since the end of nineties only two experiments have provided data on transverse effects, the HERMES Collaboration at DESY and the COMPASS Collaboration at CERN. These two experiments have performed measurements of azimuthal asymmetries in SIDIS processes of leptons off transversely polarised target. These two experiments have provided the first ever measurements of the so-called Collins and Sivers asymmetries, which involve the transversity function $\Delta_T f(x)$ and the Sivers function $f_{1T}^{\perp}(x)$. In the following, I will comment only on the measurements of the Sivers functions, which is relevant for this thesis. First result were published by HERMES in 2004 for a proton target [42] for years 2002-2003; the analysis has been completed for years 2002-2005 [43]. HERMES showed for the first time that the Sivers effect is a real effect and that the transversity PDF is different from zero. The kinematical region covered by the HERMES experiment is: $W^2 > 10$ GeV^2, $Q^2 > 1$ (GeV/c)^2, $0.1 < y < 0.85$, $0.2 < z < 0.7$ and $0.023 < x < 0.4$. Sivers asymmetries are available for pion and kaons; they are positive for positive hadrons and consistent with zero for negative hadrons. Results are shown in Fig. 2.7.

The COMPASS Collaboration has measured for the first time the Sivers asymmetry using a transversely polarised deuteron target (2003-2004) and successively for a transversely polarised proton target (2006). The kinematical region covered is: $W^2 > 25$ GeV^2, $Q^2 > 1$ (GeV/c)^2, $0.1 < y < 0.9$, $z > 0.2$ and $0.003 < x < 0.4$. Results for the deuteron target are shown in Fig. 2.7. Results for the proton target are shown in Fig. 2.8. The COMPASS data are all compatible with zero, both for positive and negative hadrons, within their statistical errors. This fact is explained in terms of cancellation between u and d quark in the case of deuteron target, and there is a good agreement between the COMPASS data points and the theoretical fits also shown in Fig. 2.7. The theoretical calculation predicts a slightly positive Sivers asymmetries for COMPASS positive hadrons, but the compatibility of the measured data and the theoretical predictions is marginal.

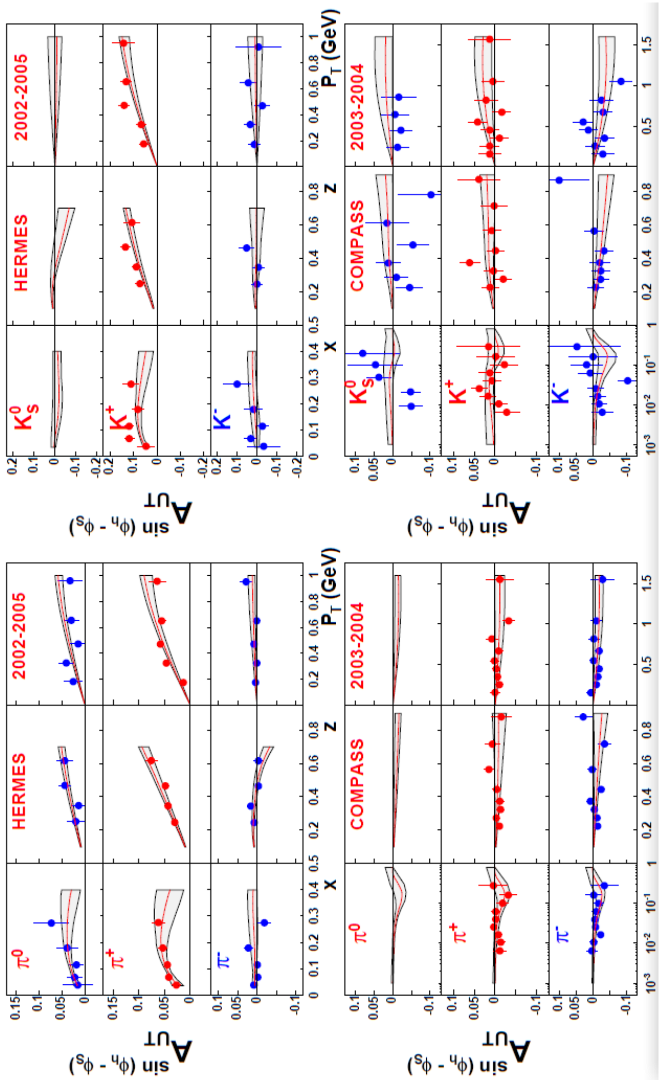

Figure 2.7: Sivers asymmetries as a function of x, z and P_T^h from HERMES (proton, upper row) [43], and COMPASS (deuteron, lower row) [44]. The curves are fits to the data, taken from [45].

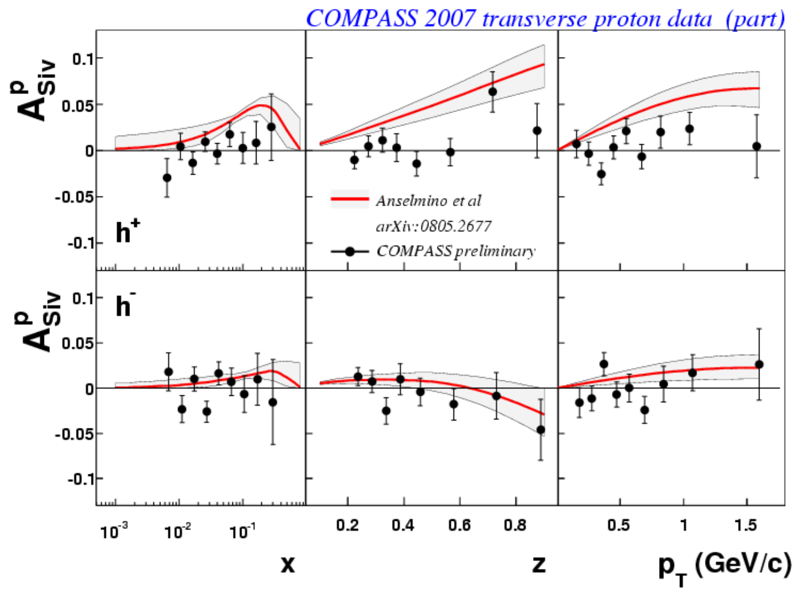

Figure 2.8: Sivers asymmetry as a function of x, z and P_T^h from COMPASS proton data. Continuous line are fits on previous data [45].

Chapter 3

The COMPASS spectrometer

The COmmon Muon and Proton Apparatus for Structure and Spectroscopy (COMPASS) is located in the North Area of the European Center for Nuclear Research (CERN) and it is a high rate fixed target experiment built at the end of the beam line M2 which delivers particles produced from the Super Proton Synchrotron (SPS).
In 1996 the COMPASS proposal [46] was written by a collaboration formed by two different research communities, HMC and CHEOPS, which had different scientific program but similar experimental needs.
In this chapter the COMPASS spectrometer is presented as it was in 2007: from 2002, when it started data taking, it has been steadily improved, by implementing new trackers ad calorimeters, to achieve the configuration which was used in 2007 for transversely and longitudinally data taking. Few changes have been done to the spectrometer setup for the hadronic data taking which started in 2008 and it has been continued in 2009. In 2010 a new transversity data taking is foreseen.

3.1 Overview of the spectrometer

The COMPASS spectrometer was built keeping in mind some important points:

- large polar angular acceptance

- large momentum measurement range
- good track reconstruction
- particle identification
- high luminosity

To fulfill all these requests the spectrometer is structured as a two stages spectrometer having the advantages to enhance the momentum analysing power and to reduce the overall detector occupancies. The two stages are named *Large Angle Spectrometer* (LAS) and *Small Angle Spectrometer* (SAS) and they are built around two dipole magnets; the first spectrometer, LAS, accepts particles tracks with polar angle of 30 mrad to 180 mrad with respect to the beam line at the target position, while the second spectrometer (SAS) covers the inner cone which contains tracks with polar angle smaller than 30 mrad. The spectrometer is 60 m long after the target. Some detectors are installed before the target to track beam particles and analyse the beam itself, like the Beam Momentum Station (BMS) which is used to measure momenta of beam particles. The *Large Angle Spectrometer* is built around the SM1 magnet which is located 4 meter downstream the target; it has the main field vertical-oriented (going from top to bottom) such that charged particles are bent in the horizontal plane; it has a integral field of 1 Tm for particles passing along the beam line and it has a gap of 2.29×1.52 m^2 which ensures an acceptance of $\pm$ 180 mrad. The minimal momentum required for particle to cross SM1 is ≈ 0.4 GeV/c. The heart of *Small Angle Spectrometer* is the SM2 magnet, located 18 m away from the target; like for SM1, its main field component is vertical and it bends particles in the same direction SM1 does, thus sequentially increasing the dispersion in angular range of tracks with different momenta. SM2 has an entrance window of 2×1 m^2 and a field integral of 4.4 Tm when 4000 A current circulates in its coils. Only particles with momentum greater than 4 GeV/c are tracked in SAS. Both spectrometers have similar structure, having tracking detectors, electromagnetic and hadronic calorimeters and muon filters for muon identification. In the LAS a RICH detector (RICH) is also present and used for charged particle identification. Being a fixed target experiment the particle rate is highest on the beam axes and decreases outwards. This translates into a variety of constraints which are coped with by subdividing

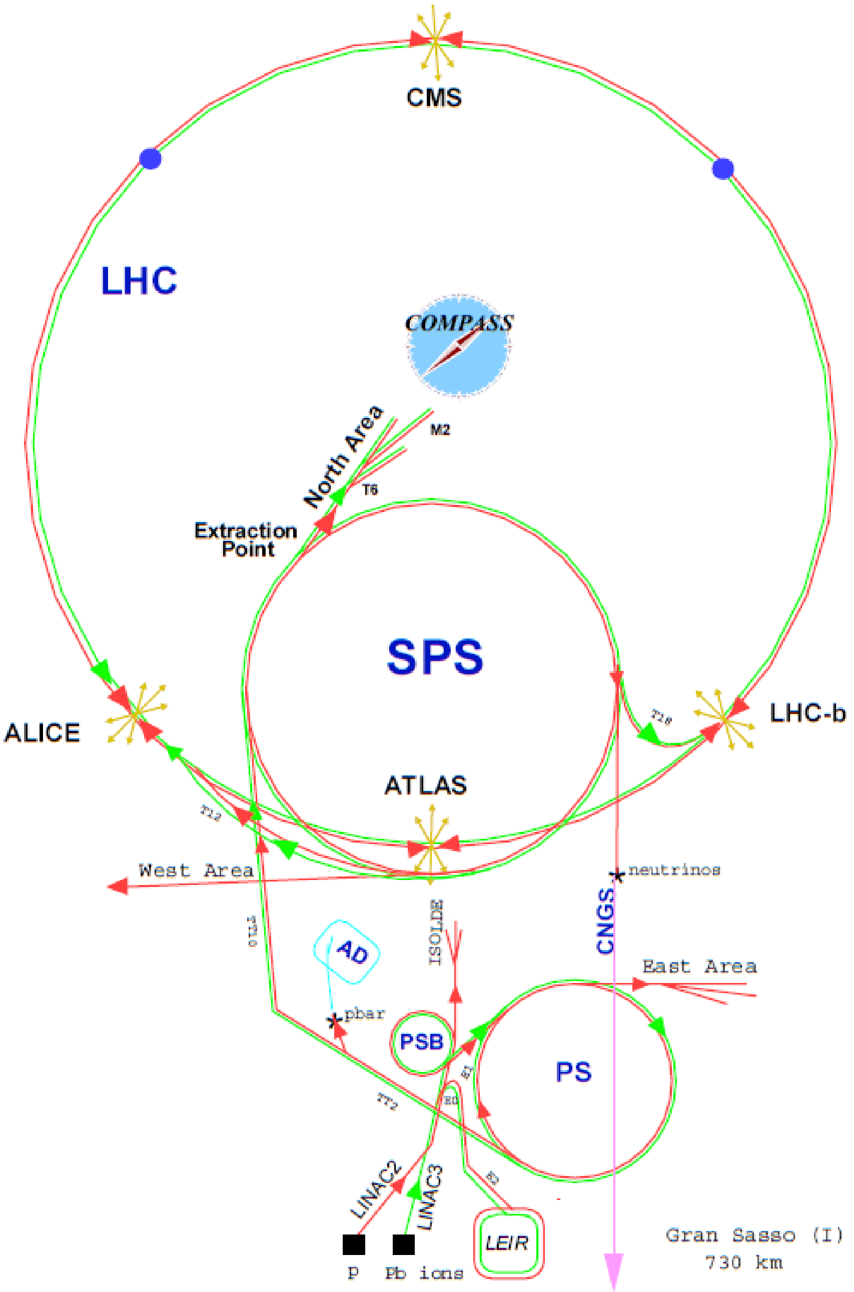

Figure 3.1: Schematic view of the accelerator complex at CERN; COMPASS is indicated in the middle of the figure

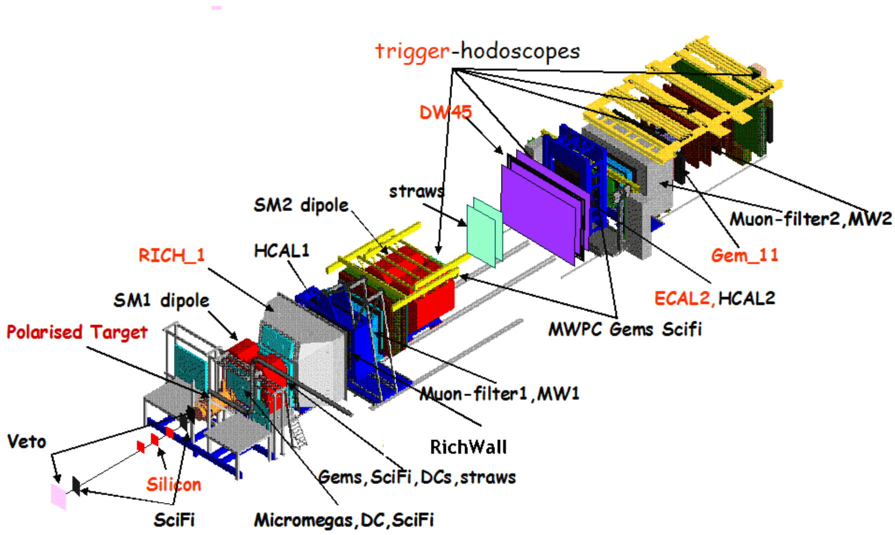

Figure 3.2: Artistic view of the COMPASS spectrometer

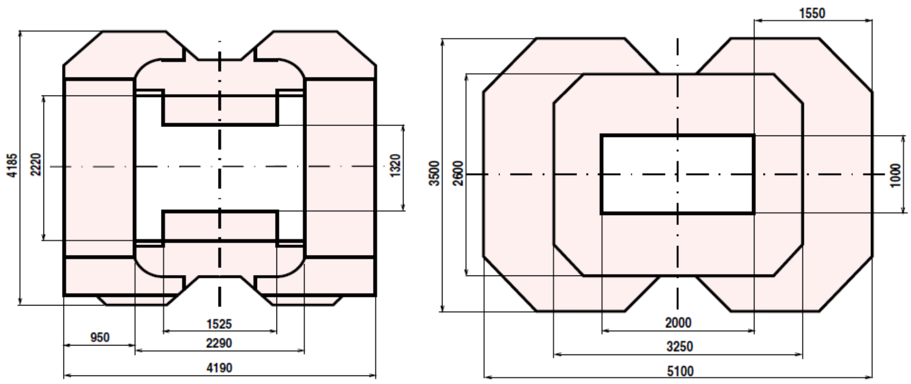

Figure 3.3: Front view of two dipole magnets SM1 (left) and SM2 (right).

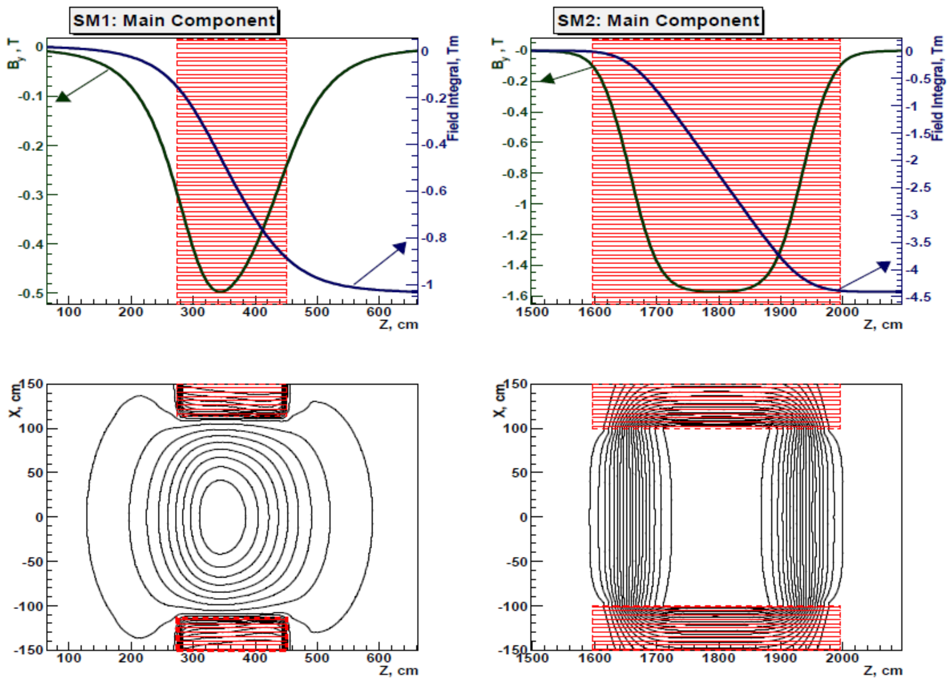

Figure 3.4: The value of the main field component B_y for SM1 (left) and SM2 (right).

the tracking system into a set of nested detectors of increasing rate capabilities. In this way larger detectors have non-sensitive area in their inner region which is covered by smaller detectors. Different types of detectors are used: MicroMesh Gaseous Structure (MicroMegas) detectors [47, 48], Gas Electron Multiplier (GEM) detectors [49, 50], Drift Chambers [51], scintillating fibers, Multiwire Proportional Chambers (MWPC), Iarocci tubes [52] for the MuonWall1 [53] and the RichWall detector [54].

3.2 The M2 beam line

COMPASS uses beams delivered by the M2 beam line which points to a production target which is hit by a proton beam extracted from the Super Proton Synchrotron. The line can be setup to produce either a secondary beam of hadrons ($\pi^{\pm}$, $k^{\pm}$, p) with a maximal momentum of 280 GeV/c or a tertiary beam of positive muons at the maximum momentum of 190 GeV/c. It is also possible to get a μ^- or e^- beam but at lower intensity and energy. The primary proton beam comes from the SPS with 400 GeV/c momentum

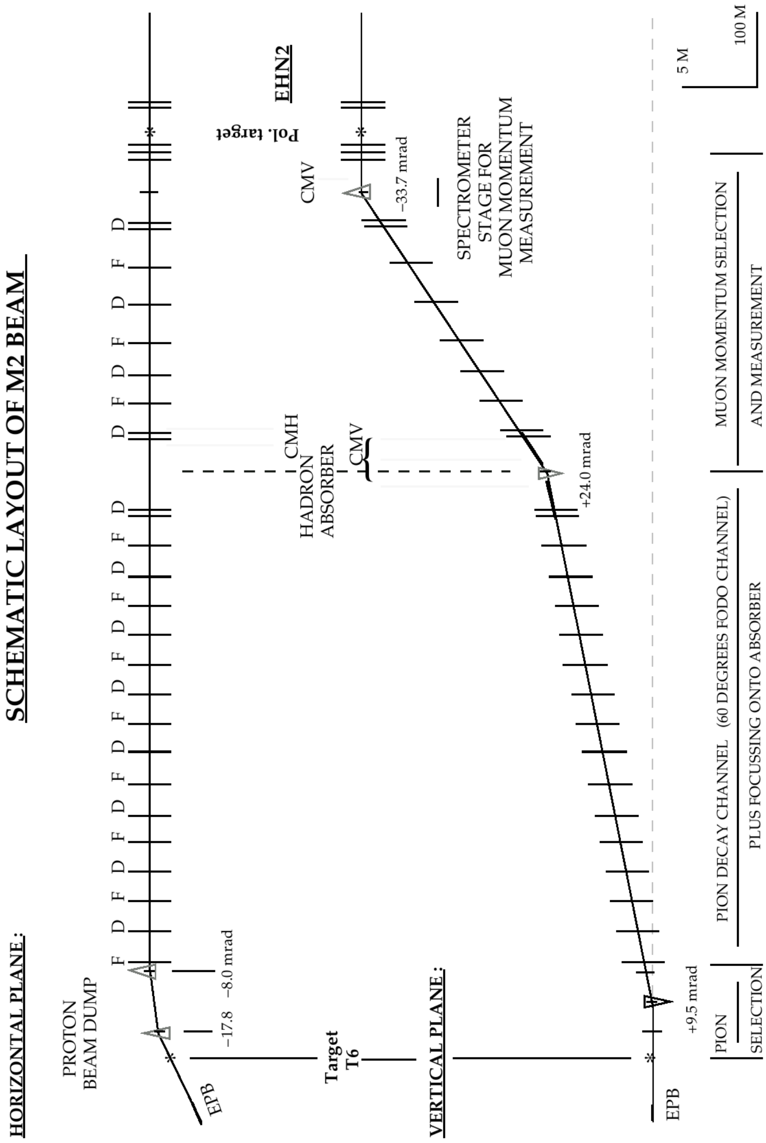

Figure 3.5: Schematic view of the M2 beam line.

and it has an intensity of $1.2{\cdot}10^{13}$ p in a spill of 4.8 s over a SPS cycle of 16.8 s. For the muon beam production, protons are guided to a target called T6 whose thickness can be adjusted to get different muon beam intensities: the highest one corresponds to the 500 mm thick beryllium target. Six quadrupoles and three dipoles make the optics which selects pions with 172 GeV/c $\pm$ 10% momentum which decay into muons (and neutrinos) along 600 m. The hadron composition of the beam is cleaned by six 1.1 m long beryllium absorber and the beam momentum is selected by a last sequence of quadrupoles and dipoles. The last part of the line carries out the beam from underground. Standard muon data taking uses a beam with momentum of 160 GeV/c at the intensity of $2{\cdot}10^8$ μ^+ per spill. The beam is longitudinally polarised thanks to the parity violating nature of weak interaction; muons are produced through the pionic decay $\pi \to \mu + \nu$ (and from kaonic decay) and the polarisation of muons P_μ reads, in the laboratory frame [55]:

$$P_\mu = \pm \frac{m_{\pi,k}^2 + \left(1 - 2\frac{E_{\pi,k}}{E_\mu}\right) m_\mu^2}{m_{\pi,k}^2 - m_\mu^2} \tag{3.1}$$

where $m_{\pi,k}$ and m_μ are the masses of the decaying mesons and of the muon and $E_{\pi,k}$ and E_μ their respective energies; the sign depends on the charge of the muon. From Eq. 3.1 it is clear that the polarisation of the muon depends on the ratio of its energy and the energy of the meson since masses are fixed. For E_π = 172 GeV/c and E_μ = 160 GeV/c, our setting for the experiment, the expected polarisation is 80%. In this two bodies decay all the kinematic is fixed and choosing the momenta of pions and muons through the optics allows to get a polarised beam. Montecarlo simulations showed a good agreement with measurements (Fig. 3.7) [56] and the polarisation is not measured by COMPASS, relying on the model. However the momenta of beam particles are measured by the Beam Momentum Station (BMS) which is composed by several scintillating fiber planes and a bending magnet; this is needed because of the way the beam is produced: it has a large momentum spread, 160 GeV/c $\pm$ 5%. The beam is focused to a sigma of 7 mm for the Gaussian core and it has a divergence of about 1 mrad. A near halo component is also present and 15% of muons belong to that. A far halo is also present, extending to many meters, and the overall intensity is compatible with the beam intensity.

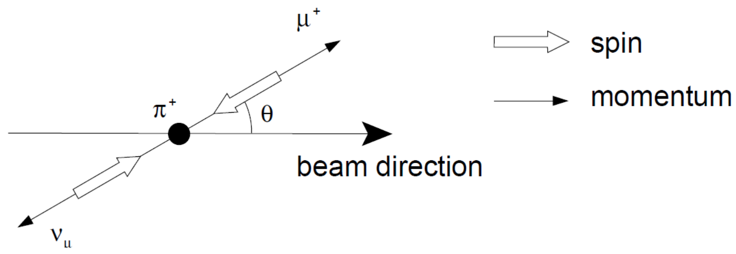

Figure 3.6: Weak π decay in the pion rest frame. Outgoing muon polarisation is obtained by selecting θ angles close to zero.

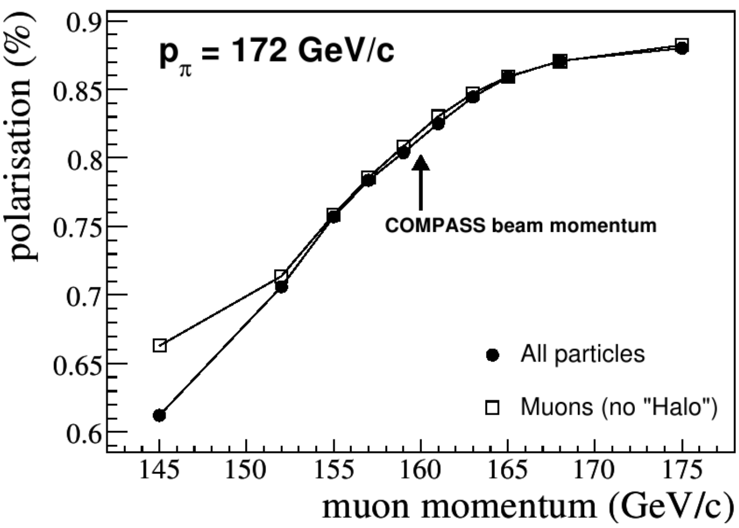

Figure 3.7: Polarisation of muons: at 160 GeV/c corresponds 80% polarisation.

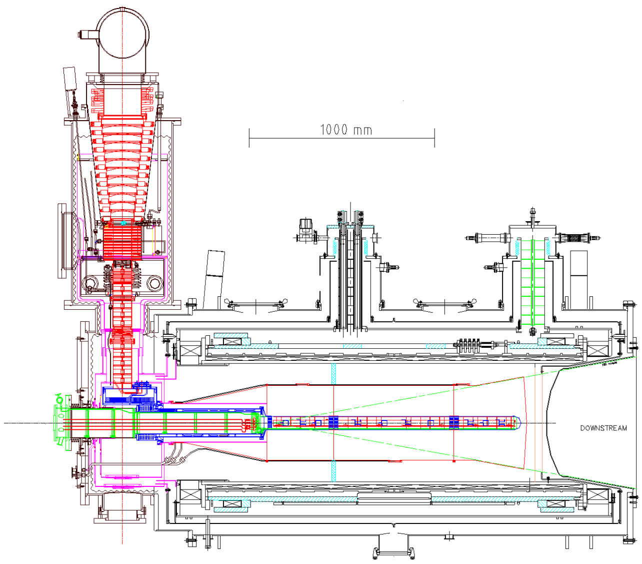

Figure 3.8: The COMPASS polarised target: the solenoid, the cryogenics and the three cells can be appreciated.

3.3 The polarised target

The polarised target is one of the most important pieces in the experiment. It allows to polarise the target material either longitudinally or transversely with respect to the beam direction. The material is in solid state thus the density makes possible to reach high luminosity. The target is organised in three cylindrical cells with radius of 4 cm and length of 30, 60 and 30 cm spaced by 5 cm; this design is needed to lower systematics error and this is implemented by polarising contiguous cells in opposite directions and regularly inverting their polarisation direction. This setup was introduced in 2006 while previously the target was made by only two cells. The cells are filled with ^{6}LiD or NH_3, according with the need to have either polarised deuteron or polarised proton. The way polarisation is obtained is very interesting and it is called *Dynamic Nuclear Polarisation* (DNP) [57] which implements the idea of transferring the polarisation from electrons to nuclei. It is clear that direct polarisation of nucleon is very hard, almost impossible, due to the small nuclear magnetic moment (μ_N is about 2000 times smaller than μ_B) which expresses the small response of the nucleon to an external magnetic field; then an intense magnetic field would be needed to reach reasonable working conditions. Curie law clearly shows this behaviour, which reads for spin-1 and spin-$\frac{1}{2}$ particles:

$$P_1 = \frac{N_1 - N_{-1}}{N_1 + N_0 + N_{-1}} = \frac{4\tanh\frac{\hbar\omega}{2kT}}{3 + \tanh^2\frac{\hbar\omega}{2kT}} \tag{3.2}$$

$$P_{\frac{1}{2}} = \frac{N_{\frac{1}{2}} - N_{-\frac{1}{2}}}{N_{\frac{1}{2}} + N_{-\frac{1}{2}}} = \tanh\frac{\hbar\omega}{2kT} \tag{3.3}$$

where $\omega = \frac{\mu B}{\hbar}$ is the Larmor frequency, μ the magnetic moment of the particle, k the Boltzmann constant and N_m the population of the magnetic sublevel m. The expected polarisation is more than 99% for electrons in a magnetic field of 2.5 T at the temperature of 1 K, while for protons and deuterons polarisations are both less than 1%. Here comes the trick of transferring the polarisation from electrons, easily polarisable, to the nucleons, let's say to protons. A surplus of electrons is created in the target material by irradiating it with an electron beam. Almost all these electrons align to opposite field direction when they are inside a magnetic field, while a little percentage of protons align to the field, as Curie law predicts. The material is then exposed to microwaves with a frequency which corresponds to the energy between the quantum state $\mid\downarrow\Downarrow>$ to the state $\mid\uparrow\Uparrow>$ (see Fig. 3.9), where the small arrow is the electron polarisation state, the bigger arrow identifies the proton's one, parallel (up direction) or anti-parallel (down direction) to magnetic field. Stimulated by microwaves, the electron-nucleon system jumps from one state to the other, and being very short the relaxation time of the electron and very long the proton's one, electrons spin suddenly aligns back opposite to magnetic field, leaving the nucleon spin aligned with field. The electron is ready to carry another proton to the aligned polarisation state. In this way protons can be pumped to the wanted quantum state and, the polarisationis built. The opposite polarisation can be achieved using the same field but using the microwaves frequency corresponding to quantum state jump $\mid\downarrow\Uparrow>$ to $\mid\uparrow\Downarrow>$. A similar consideration can be performed for the deuteron to explain the way its polarisation is obtained.

The polarisation is measured using several NMR-coil per cell [58]: the results for both NH_3 and ^{6}LiD are shown in Table 3.1 which also shows the relaxation times, the ratio f of polarisable nucleon over the total number of a atom and the product of these values with the corresponding polarisations.

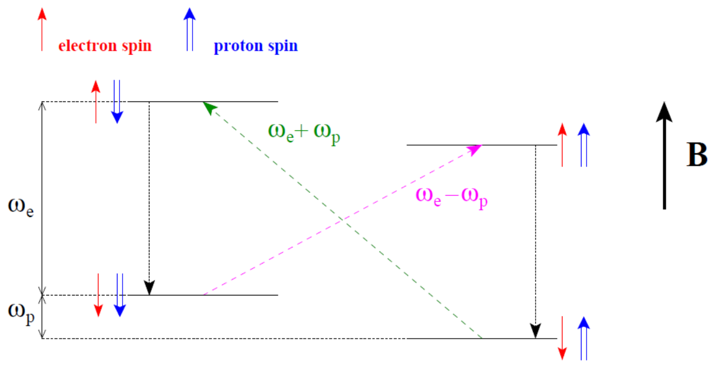

Figure 3.9: Energy levels of an electron-proton pair in a strong magnetic field B. The two frequency $\omega_e - \omega_p$ and $\omega_e + \omega_p$ are the two used to stimulate the two quantum state jump and build polarisation.

Material	P	Relaxation time	f	P$\cdot f$
NH_3	90%	4000 h @ B = 0.6 T	0.16	0.14
^{6}LiD	50%	> 1400 h @ B = 0.42 T	0.35	0.17

Table 3.1: Polarisation P , relaxation time and f for the material used as a target in COMPASS. [1]Being the target in a bath of ^{3}He and ^{4}He the effective dilution factor is lowered from 0.5 to 0.35 [63, 64, 65].

[59, 60, 61, 62]. Once the polarisation has been constructed, microwaves are stopped, the temperature drops to ∼50 mK, and the spins get "frozen". At this point, the spins can be rotated adiabatically by rotating the holding magnetic field. To obtain transverse polarisation a dipole is used: spins are again adiabatically rotated changing the magnetic field components and this is achieved by lowering the solenoid field while the dipole field increases. Polarisation cannot be measured during data taking in the transverse mode but relaxation times are large enough to guarantee it for quite a long time (days). It is worth to point out that the target material occupies only half the target cells volume, the remaining half being filled by a bath of ^{3}He and ^{4}He. Traces of other materials are also present inside the target like carbon, flour, nickel, copper and other coming from target cells, NMR-coils and other objects in contact with the target [60, 61].

3.4 Tracking detectors

The COMPASS spectrometer is made of several detecting plane measuring x and y coordinates along the beam direction z (see Fig. 3.10). To disentangle ambiguities when serveral tracks are present, some u-v planes are installed with some tilting angles around z axis. As already said, different types of detectors covers different areas, because of the increasing particle flux closer to the beam axis and this requires that detectors can sustain high rates; depending on the size of the covered area it is possible to group the detectors in *Very Small Area Trackers*, *Small Area Trackers* and *Large Area Trackers*.

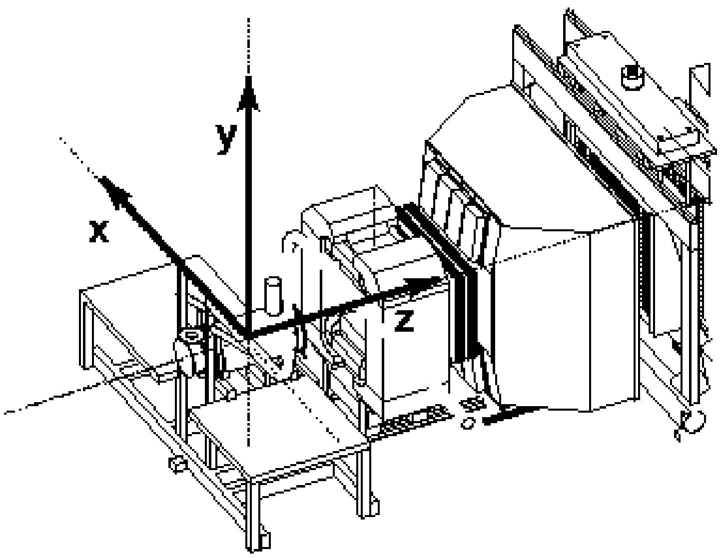

Figure 3.10: COMPASS Main Reference System (MRS): the z axis is along the nominal beam direction, the y axis is in the vertical direction pointing upwards, the x axis points such that a right handed frame is defined (toward Jura side); the center of target is in the origin of axis.

3.4.1 Very Small Area Trackers

The aim of these detectors is to track particles in the region around the beam axis and in particular beam particles. To this category belong Scintillating Fiber (SciFi) and Silicon detectors. Four stations of SciFi are around the target, two before and two after; other four stations are around the two

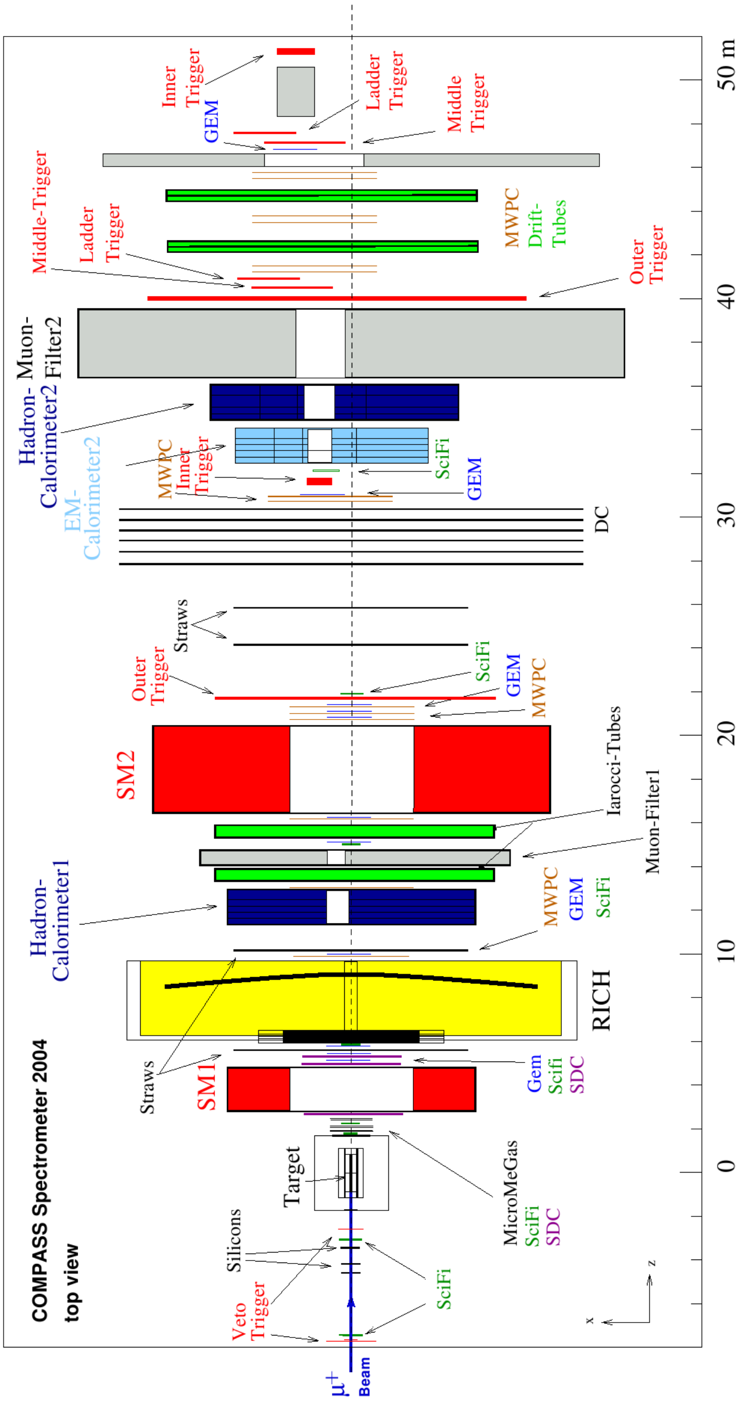

Figure 3.11: The COMPASS spectrometer in 2004.

magnets. They cover around 5x5 cm^2 and do not have dead zones; fibers have a diameter of 0.5-1 mm and each stations counts at least two projections providing good spatial and time resolutions (up to 130-250 μm and 350-450 ps [66, 67]).
The beam telescope formed by the two SciFi station upstream the target is completed by three Silicon stations made from two wafers; one wafer uses both sides for x and y projections measurement, while the other, being 5 degree tilted, gives u and v projections. Average spatial resolution is about 10 μm, time resolution is about 2.5 ns. Other Silicon Stations have been added for the hadronic program and a cryogenic system has been implemented to keep them cold and protect them from radiation damage.

3.4.2 Small Area Trackers

To the *Small Area Trackers* category belongs detectors which cover region distant 2.4 to 30-40 cm from beam axis. These detectors are gaseous detectors, GEM and MicroMegas; these are two new type of detectors, which have been used for the first time in COMPASS spectrometer. Twelve MicroMegas planes are installed between the target and the first magnet, SM1. They are grouped by four, each station providing x-y projections and 45° rotated u-v projections. They cover 40 $\times$ 40 cm^2 and have a dead zone of 5 $\times$ 5 cm^2 in the center. The design of MicroMegas has been thought in order to have a fast detector with good spatial resolution; both requirements have to be fulfilled by detectors installed close to the target, where high rates are expected since the particles flux has not lost its very low momentum component by passing through SM1. MicroMegas chambers are made with a metallic mesh separating the gas volume in two different zones (see Fig. 3.12): in the first one, 3.2 mm wide, ionisation is produced by particles passing in the gas and resulting primary electrons drift, driven by a moderate electric field of 1 kV/cm; in the second zone, wide only 100 μm, the applied field is 50 kV/cm and avalanches are produced and quickly collected by anodes. This structure manages to evacuate positive ions produced during the avalanche and to reduce transverse electron movements, resulting in a very fast detector.
GEMs are detectors which implement similar idea but with different technique, namely separation of ions and electrons, removal of the formers, fast detection and amplification of the latters. GEMs are made of several

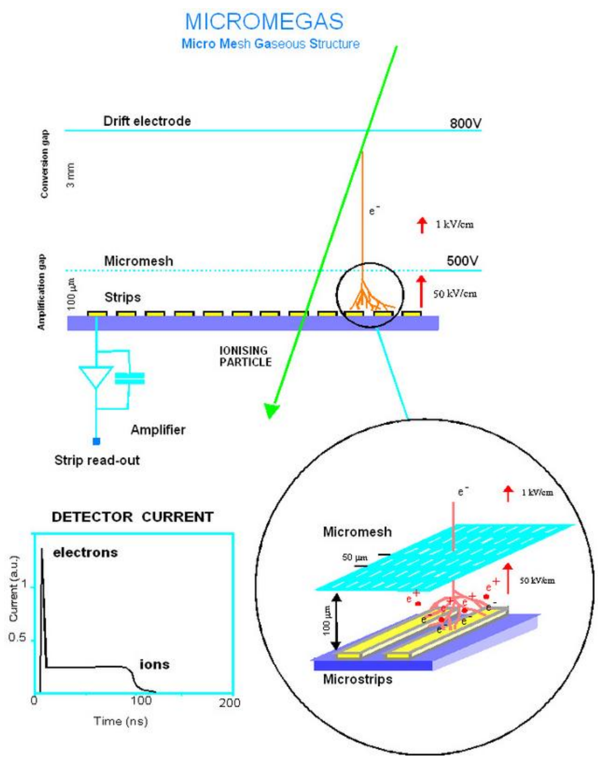

Figure 3.12: Structure of MicroMegas detectors: in the first volume electrons derive; after passing the mesh the avalanche reaches anodes.

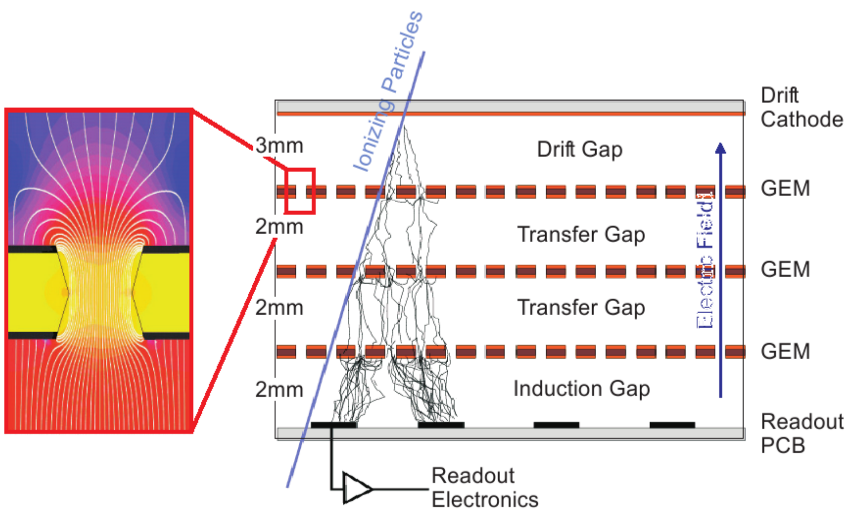

Figure 3.13: Schematic view of a GEM chambers: electrons amplify by going through holes in foils

Polyamide foils with a copper cladding on both sides; foils have been worked to have a high density of micro-holes (10^4 holes per cm^2) with 70 μm diameter. These GEM foils are inserted between electrodes in a chamber filled of gas (see Fig. 3.13), and a potential difference is applied across the foils. Charged particles pass, the gas is ionised, electrons drift and are multiplied in the micro-holes, foil after foil, while positive ions are removed by cladding. After the last foil, a pcb plane with read-out electrodes is used to read signals. GEMs cover 31 $\times$ 31 cm^2 area, have dead zone like MicroMegas, space and time resolution of 12 ns and 70 μm. In the last two years a new kind of GEM has been introduced, the Pixelised GEM (PixelGEM), used as *Very Small Area Trackers* covering 10 $\times$ 10 cm^2 and substituting SciFi stations around the two magnets.

3.4.3 Large Area Trackers

Increasing the distance from the beam axis, drift chambers, Multiwire Proportional Chambers, Straw and Iarocci tubes are used as detectors.
In the LAS four Drift Chambers (DC) stations are used, three before and one after SM1. Each station provides x-y and u-v projections. The first three stations have a useful area of 180 $\times$ 127 cm^2, with a dead zone of 30 $\times$ 30 cm^2. The fourth DC station, located immediately after the SM1 magnet, has a usefull area of 240 $\times$ 204 cm^2. An enlarged view of the LAS is shown in Fig. 3.14.

Another type of drift chambers, called W4-5, are used in the SAS, they have a surface of 5 $\times$ 2.5 m^2 and also a dead zone of 50 cm radius.
Straw detectors are used in both LAS and SAS providing x-y and u-v projections, covering 3.2 $\times$ 2.8 m^2, with central dead zone of 20 $\times$ 20 cm^2.
The main tracking system in the SAS consists of 14 stations (37 planes) of MWPC disposed over 37 m along the z axis. Three different type of MWPC stations are used: A type measuring y and u-v projections; B type measuring y and v projections; A* type which is an A type with additional x projection. u-v planes are tilted by 10.14°. The plane active area is 1.7 $\times$ 1.2 m^2 and the diameter of thedead zone depends on the z position of the detector and varies from 16 cm to 22 cm to fit the beam spot and halo size. The distance between wires is 2 mm, which corresponds to a spatial resolution of about 600 μm.
In 2006 a new large-size tracking station called RichWall [54, 68] was po-

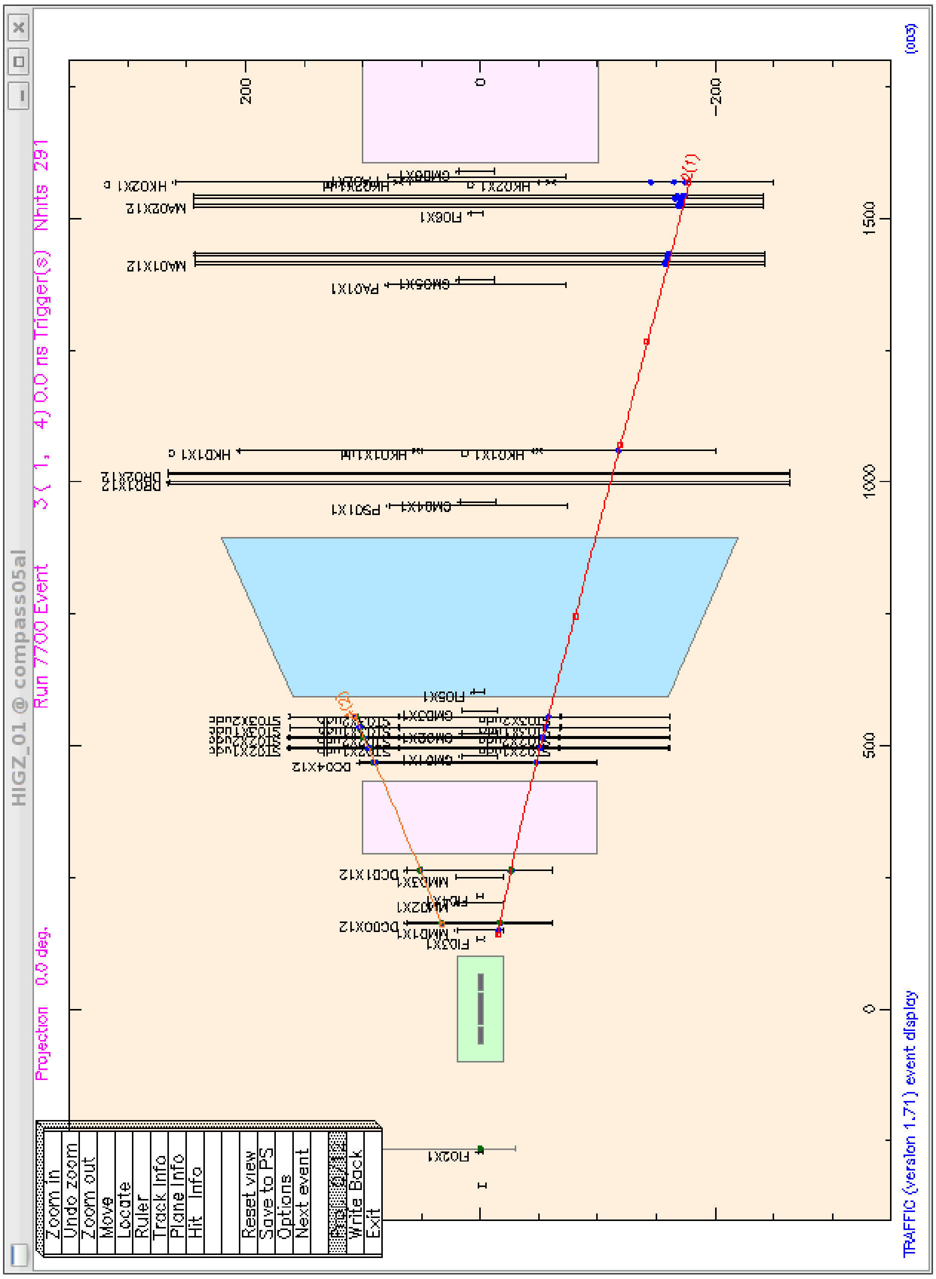

Figure 3.14: View of the LAS from the event display of reconstruction program (CORAL). Two reconstructed tracks are also visible.

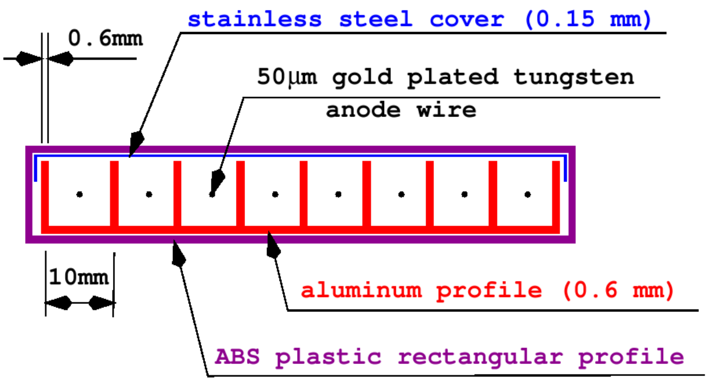

Figure 3.15: Profile of Mini Drift Tube base structure: they are used in the RichWall and in the MuonWall1 detectors with the difference that RichWall profile are 0.45 mm thick, while MuonWall1 ones are 0.6 mm.

sitioned downstream of the RICH detector directly in front of the ECAL1 electromagnetic calorimeter. It covers 4.86×4.22 m^2 and it has a hole of about 120×50 cm^2. It consists of eight layers of MDT modules (see Fig. 3.15); the basic module is composed by an eight combs aluminum profile covered with a stainless steel layer; in each comb a gold plated tungsten wire with the diamater of 50 μm acts as anode. The profile is insulated by plastic material. The RichWall detector provides up to four coordinate points per track in two projections, x-y planes. The coordinate accuracy (about 800 μm per plane) is obtained by reading out the MDT modules in drift mode. Between planes of the detector lead layers can be installed as converter counting up to 3 radiation lenghts. So the RichWall tracker station performs a twofold function in the COMPASS spectrometer. First, it measures the particle trajectories downstream of the RICH, thus allowing a better reconstruction of the particle trajectories in the RICH volume. Second, it acts as preshower for the ECAL1 electromagnetic calorimeter, thus improving the spatial resolution of the calorimeter itself.

3.5 Muon identification

The tracking and identification of muons are performed by two sets of detectors, MuonWall1 in LAS and MuonWall2 in SAS; both of them are screened from passing hadrons by hadron and electromagnetic calorimeters and pas-

sive muon filters.
The MuonWall1 (MW1) is placed at the very downstream end of LAS, just in front of SM2. It is made of Iarocci-type chambers, with 8-cell comb-like aluminum profile, like the RichWall detector. The detector consists of two modules which sandwich a 60 cm thick iron layer. It has a useful surface of about 4.8 $\times$ 4.1 m^2 and a central hole of 1.4 $\times$ 0.8 m^2, and it provides the detection of muons scattered at large angles and in the high Q^2 region. The two modules consist of 16 planes in total, measuring the x and y projections only. Because of the multiple scattering in the absorbers, there is no need to determine the muon trajectory with high accuracy. The resolution of about 3 mm achieved in the proportional chamber mode is sufficient. MuonWall 2 (MW2) consists of two identical stations of layers of drift tubes around a 2.4 m concrete absorber. Each of the two stations consists of six layers with an active area of 447 $\times$ 202 cm^2 grouped into double layers, each mounted on a separate steel frame. The three double layers have vertical, horizontal and 15° tilted tubes providing x-y and u projections. The MW2 is installed at the very end of SAS, in the region of trigger hodoscopes, and it has a quite big central physical hole of 0.9 $\times$ 0.7 m^2.
In the SAS, muon identification is also perfomed by MWPC-Bs which cover part of the MW2 hole and partially overlap it. In addition to the detectors mentioned above, trigger hodoscopes are also used in the tracking system. Made of fast scintillator counters, these hodoscopes have very high time resolution (1 ns) to provide a time reference for the other detectors. However, their space precision is limited. The slab size varies from 0.6 to 15 cm depending upon the distance from the beam line. Notwithstanding this crude space resolution, hodoscopes are helpful in solving ambiguous pattern problems, taking advantage of the long lever-arm. In particular the importance of the hodoscopes, close to the beam axis and after the second muon filter, is obvious for the reconstruction of muons scattered at small angles, since no small aperture detectors are installed downstream of the second muon filter.

3.6 The Rich detector

Charged hadron identification is obtained using a large ring imaging Cherenkov detector, the COMPASS RICH-1 [69, 70]. The RICH detector uses C_4F_{10} as

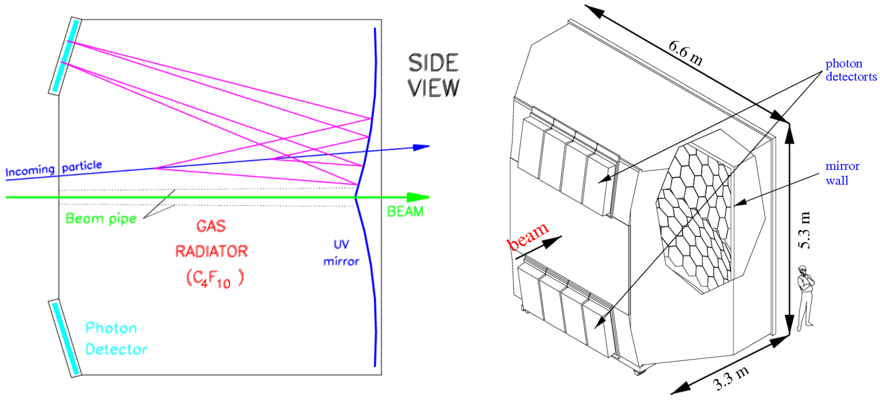

(a) (b)

Figure 3.16: (a) illustration of rays reflected by RICH mirrors; (b) artistic view of the RICH detector.

radiator gas inside a 5 × 6 m^2 wide and 3 m deep vessel, to cover the large trasverse area of 180 mrad acceptance. The produced Cherenkov photons are reflected on a 20 m^2 mirror wall onto two sets of photon detectors, an upper and a lower one which are positioned outside the spectrometer acceptance to reduce material budget. In order to absorb the photons emitted from beam muons, that would cause a prohibitive amount of background photons, a 10 cm diameter pipe filled with helium is positioned around the beam axis in the vessel. The RICH allows to identify hadron from Cherenkov threshold till momenta of 60 GeV/c^2; Cherenkov thresholds for π, K and p are respectively 2.5, 9.5 and 17 GeV/c^2.

Until 2004, the photon detectors used were eight multi-wire proportional chambers (MWPCs) with cesium iodide (CsI) photo-cathodes. During the year 2005, the RICH detector was upgraded to satisfy the requirement of the second part of COMPASS data taking. Moreover a limitation was existing due to the presence of the large muon halo which produced too many background photons which increased the occupancy on electronics. Therefore a new and fast photon detection system was developed and installed between autumn 2004 and spring 2006 in order to be able to distinguish by time information between photons from physics events and background, and to be able to run at higher trigger rates of up to 100 kHz. The upgrade of the COMPASS RICH-1 is two-fold: in the central part of the photon detectors

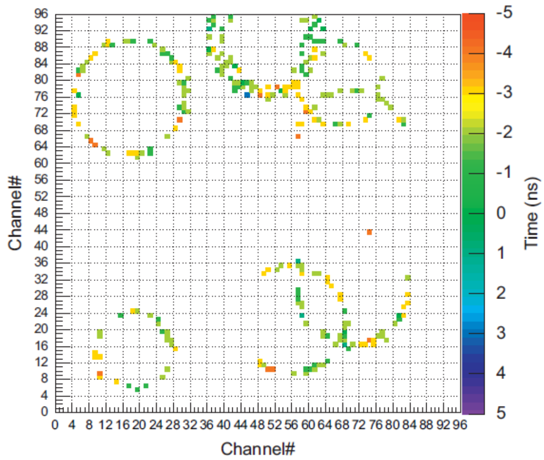

Figure 3.17: Online display of Cherenkov rings from a physic event.

(1 of the surface), the MWPCs have been replaced by Multi-Anode Photomultipliers (MAPMTs) [71] with new read-out electronics based on the $\mathcal{F}1$ digital chip [72] and on the new CMAD chip. In the outer part, the existing MWPCs have been equipped with a faster readout electronics based on the APV preamplifier with sampling ADCs.

3.7 Calorimeters

Four calorimeters are installed in the spectrometer, an electromagnetic and an hadronic calorimeter in both LAS and SAS. They are called ECAL1, HCAL1, ECAL2 and HCAL2. They are used to measure the energy of thep-articles and they are included in the trigger of semi inclusive muon scattering events. Since they consist of many radiation lenghts of material,they contribute to the absortion of the particles which cross them. All calorimeters are mounted on mobile platforms that allow to move them along transverse directions with respect to beam axis and the platforms themselves can roll on rails and move along the beam direction. ECAL1 is formed by blocks of three different sizes. The most central region is equipped with 576 blocks of 38.2×38.2 mm^2 (GAMS). In the intermediate region 580 blocks of 75×75 mm^2. The most external region is filled with 320 blocks with dimensions of 143×143 mm^2 (OLGA). The signal amplitude from all the calorimeter blocks are read by fast sampling SADCs. It allows measurements of reaction

channels with the production of low energy prompt photons and/or neutral pions.
HCAL1 has a modular structure, each module consisting of 40 layers of iron and scintillator plates, 20 mm and 5 mm thick, respectively, for a total of 4.8 nuclear interaction lengths. Monte Carlo simulations for hadrons and electrons were performed in the 10 - 100 GeV energy range, showing that these particles are almost fully absorbed in such a calorimeter. 480 calorimeter modules were assembled and framed in a matrix of 28 horizontal $\times$ 20 vertical modules with 12 of them removed from each corner. There is a rectangular window of 8 $\times$ 4 modules at the centre of the matrix for the passage of the beam and scattered muons.
ECAL2 consists of 2972 (a matrix of 64 $\times$ 48) lead glass modules (GAMS) with 38 $\times$ 38 $\times$ 450 mm^3 dimensions amounting to 16 radiation lengths. A high energy gamma ray or electron incident on ECAL2 develops an electromagnetic shower inside the lead glass. The electrons and positrons from a shower emit light on their way through the glass and the amount of light is proportional to the energy deposited in each counter. A hole of 10 $\times$ 10 modules in the centre allows passage of the beam particles.
HCAL2 takes the form of a matrix of 22 $\times$ 10 modules. The basic modules are sandwich counters with 20 $\times$ 20 cm^2 transverse dimensions. The calorimeter has a hole with the dimensions of 2 $\times$ 2 modules to let the high intensity beam go trought. Two types of modules are used in the detector: most of them consist of thirtysix 25 mm thick steel plates, interleaved with 5 mm thick scintillator sheets. The overall thickness of the counters is 5 nuclear interaction lengths for pions and 7 for protons. The central 8 $\times$ 6 cells are filled with thicker modules consisting of forty layers.
All calorimeters show good linearity which allows to parametrise the energy resolution as Tab. 3.2 summarises [73, 74, 75, 76].

3.8 The trigger

The trigger system is responsible of deciding in less than 500 ns, keeping as low as possible dead time, if an interesting scattering event has occurred and then triggers the readout of detectors. Additionally, it provides an event time reference to unambiguously associate the event with the incident muon. This is achieved using fast hodoscopes signals, energy deposits in calome-

Calorimeter	Energy resolution
HCAL1	$\frac{\sigma(E)}{E} = \left[\frac{59}{\sqrt{E}} + 8\right] \%$
ECAL2	$\frac{\sigma(E)}{E} = \left[\frac{59}{\sqrt{E}} + 8\right] \%$
HCAL2	$\frac{\sigma(E)}{E} = \left[\frac{5.5}{\sqrt{E}} + 1.5\right] \%$

Table 3.2: Calorimeter energy resolution are well parametrised thanks to good linearity of calorimeters.

ters and on the event kinematics which are coded in suitable coincidence matrixes [77].
The quasi real photon trigger consists of two parts, a trigger on the energy loss by measuring the deflection of the scattered muon in the two spectrometer magnets and a calorimetric trigger selecting hadron energy clusters above a threshold. The trigger is based on the detection of the scattered muon. Muons are measured in two horizontal scintillator hodoscopes in order to determine the projection of the muon scattering angle in the non-bending plane and to check its compatibility with the target position (vertical target pointing). Correlanting the spacial information from two vertical strips hodoscopes, only events with $Q^2 > 0.5$ (GeV/c)^2 are mainly triggered, while the maximum value of Q^2 is only limited by the SM2 hole. According to their distance from the beam axis, three pairs of vertical strips muon hodoscopes are used, the so-called Inner Trigger (IT), the Middle Trigger (MD) and the Outer Trigger (OT); their main differences is granularity: being nearer beam axis, Inner Trigger hodoscopes are thinner. To suppress events due to halo muons, a veto system, made of three hodoscope planes, is added to the trigger system. MT, IT and LT are completed by the calorimetric infomations. In fact, at these small angles there are several background processes such as elastic scattering on target electrons, elastic and quasi-elastic radiative scattering on target nuclei and beam halo contributing to the scattered muon signal. The trigger system requires energy clusters in the hadronic calorimeter, which are absent in the background processes. The signal coming from coincidence of MT hodoscopes is also available without calorimeter information, giving the Inclusive Middle Trigger (iMT). Clusters in calorimeters also fire a pure Calorimeter Trigger (CT) whose threshold is higher than the one set for previous triggers; these CT events are characterised by high Q^2

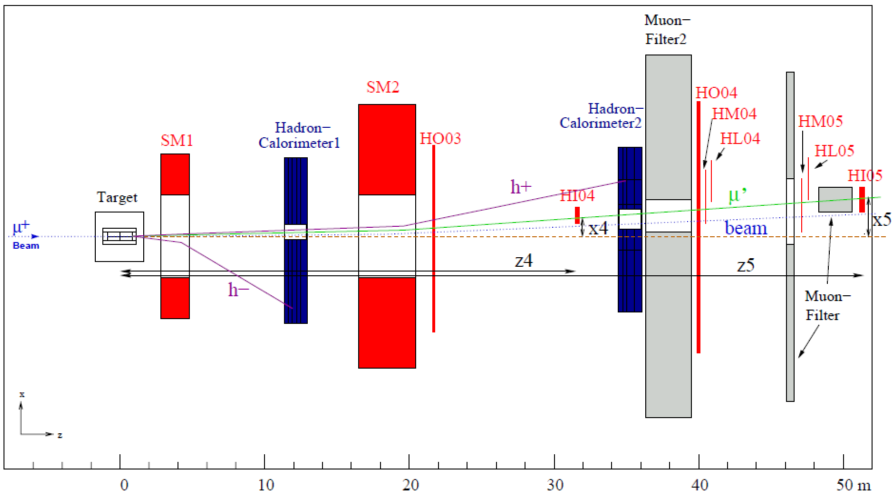

Figure 3.18: This figure schematically shows how trigger works. Beam particles (blue line) do not hit trigger hodoscopes. Produced hadrons (violet) are measured in hadronic calorimeters. The scattered muon (green) hits trigger hodoscopes, HI04 and HI05, in this picture. Knowing the distances of slabs from beam axis and from target the muon can be identified.

and the scattered muon outside OT acceptance.

New hodoscopes are foreseen for the year 2010, when a new transversity run will be taken. While all the other hodoscopes are presently in the SAS, the two new scintillator counter hodoscopes will be placed in the LAS, thus giving access to large angle scattered muon emerging from high Q^2 events.

3.9 Data acquisition

The COMPASS spectrometer has a pipelined readout architecture to reach the high performaces required by the large numbers of detector channels: more than 250000 channels send data at a trigger rate of more than 20000 triggers per spills. Data are written with more than 10 kHz rate and the average event size is 40 KByte. This result in more than 500 TByte data volume per year.

Detector signals are digitized on the front-end eletronics, using ADC or the **F**1 TDC [78] for time measurements. From here the data are sent through the full readout chain down to the recording buffers by only pushing the data without handshake. From the front-end boards the data are transferred to the central readout driver via standard Ethernet cables or optical

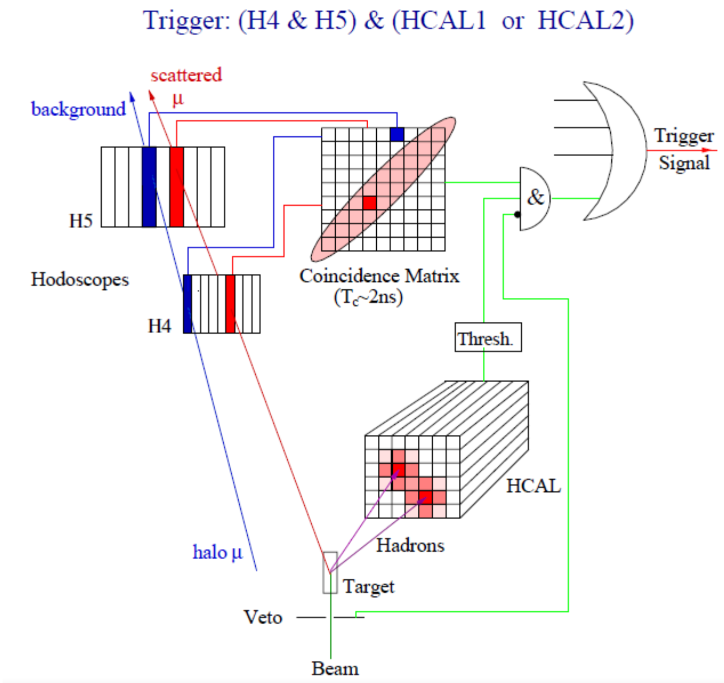

Figure 3.19: Schematic view of the way trigger hodoscopes and calorimeter information are used to construct the trigger.

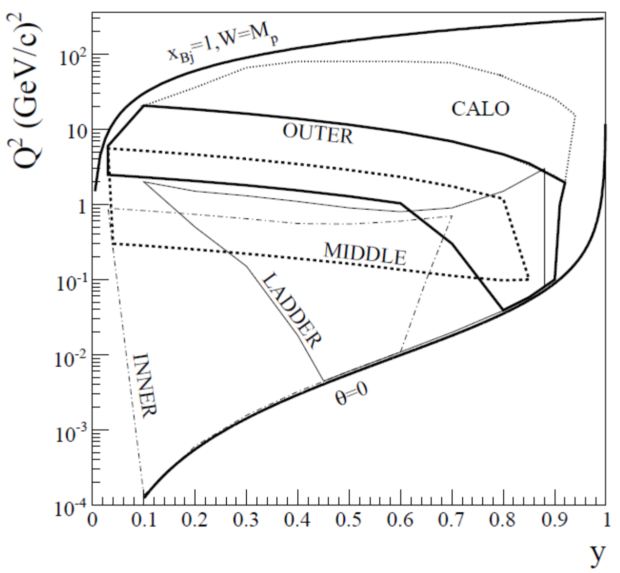

Figure 3.20: The range in y and Q^2 for the different triggers.

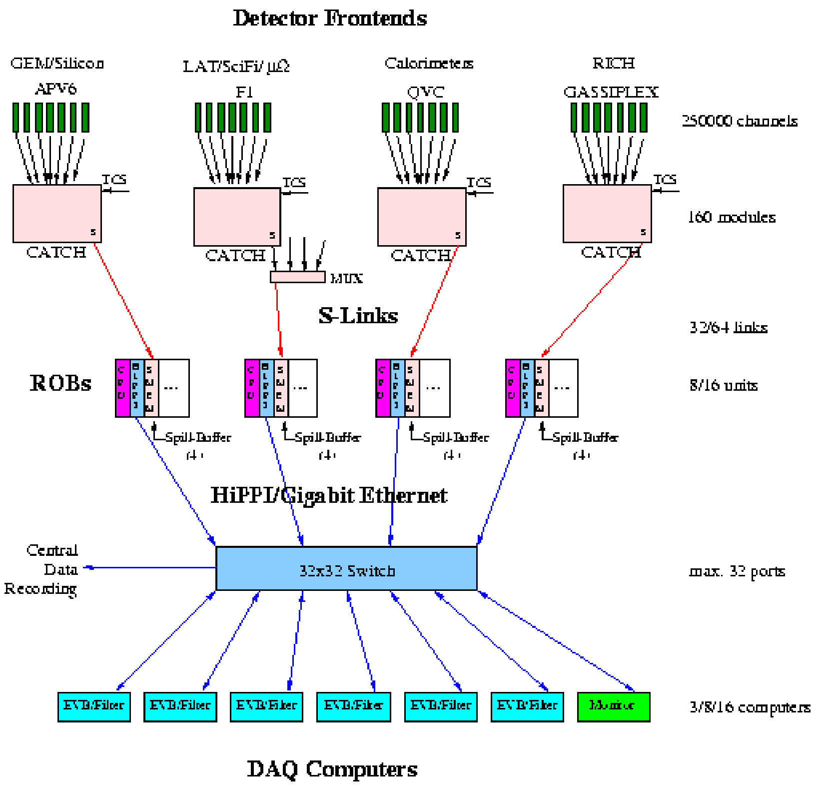

Figure 3.21: Schematic view of the data acquisition chain.

fibres. The central readout drivers for the detectors are the COMPASS Accumulate, Transfer and Control Hardware (CATCH) and the GeSiCA (GEM Silicon Control and Acquisition) [79]. The CATCH module [80, 81] is a VME module acting as an interface between frontend boards and the readout computers. It allows fast readout of the front-ends, performs local subeventbuilding and concentrates the data into few high bandwidth streams (160 MByte/sec/CATCH). The CATCH also initialises all front-ends at startup and distributes the trigger signal it receives from the Trigger Control System (TCS) to the front-end boards. The data from the CATCH are guided through the readout chain while further triggers can be accepted. The data buffering at various stages minimises the dead time and avoids data losses. The modular design makes the system easily scalable and upgradable. From the CATCH the data are transferred via optical fibres using the S-Link protocol to the spill buffers [82]. They are located inside the readout buffer (ROB) computers, where the data of several detector planes for one event is combined, consistency checks and subeventbuilding are performed. Via Gigabit Ethernet the data are transferred to the eventbuilders. Here the data from all ROB are combined to the full events, transferred to the Central Data Recording (CDR) at the CERN main site and copied on tape for long term storage. Data receiving, processing and transferring from the CATCH to the spill buffers happen only on-spill. In order to optimise the data flow, during the interspill the data are transferred from the spill buffers via the ROB to the eventbuilders, and from there to the CDR.

Chapter 4

The Drell-Yan process

The Drell-Yan process is an interaction which occurs between two different hadrons and whose characterising signal is a pair of leptons in the final state, which are believed to be created in the annihilation process of a quark and an anti-quark from the two colliding hadrons.
First experimental observations of a μ^+ μ^- pair continuum spectrum were done in early 1970s when the reaction $p+U \rightarrow \mu^+ + \mu^- + X$ was studied at the Alternating Gradient Synchrotron (AGS) at Brookhaven National Laboratory [83].
The interpretation of this process was first done by S. Drell and T. M. Yan, who proposed a possible mechanism for this di-lepton production [84, 85], suggesting the process that took its name from the two teorists: the two hadrons interact electromagnetically, a quark belonging to one hadron annihilate with an anti-quark of the other hadron producing a virtual photon, which then converts into a pair of $\mu^+\mu^-$, e^+e^+, ...
In this chapter the Drell-Yan process is described as well as the possibility to access parton distribution functions with this interaction. In this work the Drell-Yan process will be commonly intended as the production of a pair of muons; therefore di-muon and di-lepton are used as synonymous.

4.1 Drell-Yan kinematic variables

The Drell-Yan process can be characterised by kinematic variables directly computed from the two muons which are tracked in an experimental apparatus and whose vertex is reconstructed in the interaction region. The

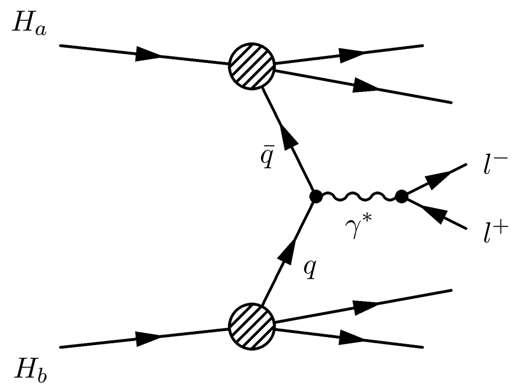

Figure 4.1: The Drell-Yan process: a quark anti-quark pair coming from two hadrons produces a pair of leptons

muons momenta are summed getting as a result the four-momentum of the virtual photon. The knowledge of the momenta of beams, in case of collider experiments, or the momentum of beam particle and the target material, in case of fixed target experiments, allows to compute the kinematic of each events.

Let us define some reference system and quantities that will be used in the following. The momenta of the two hadrons, H_a and H_b are respecively P_a and P_b. For a fixed target experiment, like COMPASS, in the laboratory frame the target is at rest, so the hadron H_b has four-momentum $(M, 0, 0, 0)$ and the beam particle H_a has four-momentum $(E_{beam}, 0, 0, p_{beam})$. In the hadronic center of mass frame the hadrons H_a and H_b have respectively momenta:

$$P_a = \left(\frac{\sqrt{s}}{2}, 0, 0, \frac{\sqrt{s}}{2}\right) \tag{4.1}$$

$$P_b = \left(\frac{\sqrt{s}}{2}, 0, 0, -\frac{\sqrt{s}}{2}\right) \tag{4.2}$$

where $\sqrt{s}$ is available energy, being $s = (P_a + P_b)^2$, and the hadron masses have been neglected (high energy approximation). The virtual photon has four-momentum $q = (q_0, \mathbf{q_T}, q_L)$ and $q^2 = M^2 = Q^2$; the leptons have four-momentum k_c and k_d and $k_c + k_d = q$; the two annihilating quarks have four-momenta k_a and k_b. Using the mentioned quantities, two variables can be defined and computed: the x_F and the τ variables:

$$x_F = \frac{2q_L}{\sqrt{s}} \tag{4.3}$$

$$\tau = \frac{M^2}{s} \tag{4.4}$$

where $\sqrt{s}$ is the energy in the center of mass frame.
In the parton model, in collinear approximation, the production of the muons can be naively explained with the annihilation of $q\bar{q}$ pair into a photon which produces the two leptons, and this is what Drell and Yan suggested.
The two quarks carry a fraction of the momenta of the parent hadrons, x_a and x_b. In the hadronic center of mass frame, where the quarks have longitudinal momenta $x_a\frac{\sqrt{s}}{2}$ and $-x_b\frac{\sqrt{s}}{2}$, the di-muon four-momentum $(q_0, \mathbf{q}_T, q_L)$ is:

$$q_0 = \frac{(x_a + x_b)\sqrt{(s)}}{2} \tag{4.5}$$

$$q_L = \frac{(x_a - x_b)\sqrt{(s)}}{2} \tag{4.6}$$

with the di-lepton mass squared:

$$M^2 = q_0^2 - q_L^2 = x_a x_b s \tag{4.7}$$

x_F and τ are naively linked to x_a and x_b by the expressions

$$x_F = x_a - x_b \tag{4.8}$$

$$\tau = x_a x_b \tag{4.9}$$

In the collinear approximation, q_T is obviously zero. Another variable, which is used to describe Drell-Yan events, is the rapidity y:

$$y = \frac{1}{2}\ln\frac{q_0 + q_L}{q_0 - q_L} = \frac{1}{2}\ln\frac{x_a}{x_b} \tag{4.10}$$

Then, the expressions for x_a and x_b are:

$$x_a = \sqrt{\frac{M^2}{s}}e^y = \frac{q_0 + q_L}{\sqrt{s}} \tag{4.11}$$

$$x_b = \sqrt{\frac{M^2}{s}} e^{-y} = \frac{q_0 - q_L}{\sqrt{s}} \tag{4.12}$$

4.2 The Drell-Yan cross-section

In this section the Drell-Yan cross section is discussed. First the collinear and the Born approximations are kept valid; then the transverse momentum of quarks is introduced as well as QCD corrections.

4.2.1 Collinear approssimation

The Drell-Yan cross section can be calculated and it has the general expression:

$$\sigma\left(H_a + H_b \to \mu^+\mu^- + X\right) = \sum_q \int \mathrm{d}x_a \int \mathrm{d}x_b f_a\left(x_a\right) f_b\left(x_b\right)\, \hat{\sigma}\left(q\bar{q} \to \mu^+\mu^-\right) \tag{4.13}$$

The cross section is the result of the product of the partonic cross section, averaged over quark flavors and spins, with the two parton distribution functions, $f_a\left(x_a\right)$ and $f_b\left(x_b\right)$ which describe, respectively, the probability of finding a quark from the first hadron carrying a fraction x_a of its momentum, and the probability of finding an anti-quark from the second hadron carrying a fraction x_b of its momentum.
The elementary cross section $\hat{\sigma}$ can be computed in QED and a derivation is reported in Appendix 9. The Drell-Yan cross section is:

$$M^2 \frac{\mathrm{d}^2\sigma}{\mathrm{d}M^2\mathrm{d}y} = \frac{4\pi\alpha^2}{9s} \sum_q e_q^2 f_a\left(x_a\right) f_b\left(x_b\right) \tag{4.14}$$

It is often expressed as differential in x_1 and x_2 or M^2 and x_F:

$$\frac{\mathrm{d}^2\sigma}{\mathrm{d}x_a\mathrm{d}x_b} = \frac{4\pi\alpha^2}{9M^2} \sum_q e_q^2 f_a\left(x_a\right) f_b\left(x_b\right) \tag{4.15}$$

$$\frac{\mathrm{d}^2\sigma}{\mathrm{d}M^2\mathrm{d}x_F} = \frac{4\pi\alpha^2}{9M^4} \frac{x_a x_b}{x_a + x_b} \sum_q e_q^2 f_a\left(x_a\right) f_b\left(x_b\right) \tag{4.16}$$

4.2.2 Corrections to the Drell-Yan cross section

When compared to experimental data, the Drell-Yan cross section computed in the previous section underestimates the measured event rate. The reason of this discrepancy can be found in the fact that what is happening in the Drell-Yan process is not a pure electromagnetic reaction, but quarks are colored particles, QCD cannot be completely negleted and QCD corrections must be taken into account.

Three types of QCD corrections can be distinguished: gluon emissions $q + \bar{q} \to \gamma^* + g$ (Fig. 4.2), Compton subprocesses $q + g \to \gamma^* + q$ (Fig. 4.3) and virtual gluon corrections to the annihilation Born term (Fig. 4.4). It has

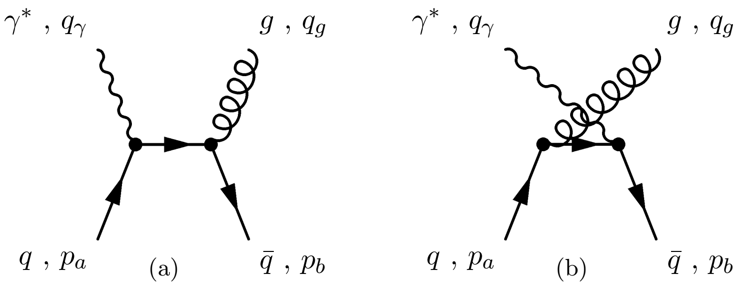

Figure 4.2: Leading order diagrams for the $q\bar{q}$ "annihilation" subprocess $q + \bar{q} \to \gamma^* + g$.

to be noticed in this respect that hard (large energy) gluon radiation is a natural mechanism by which a quark can obtain a contribution to transverse momentum and can explain transverse momentum of virtual photon, as it will be shown later in this work.

Following the prescriptions of perturbative QCD, the interaction terms can be ordered in a perturbation series in the strong coupling costant α_s, which can be parametrised as:

$$\alpha_s\left(Q^2\right) = 12\pi \left[(33 - 2f)\log\left(\frac{Q^2}{\Lambda^2}\right)\right]^{-1} \tag{4.17}$$

where f is the number of quark flavours and Λ (≈ 200 MeV/c) sets the scale of the strong interaction. When Q^2 is chosen to be of the square of typical di-muons masses (4-10 GeV/c^2) α_s is of the order of 0.1, thus making the

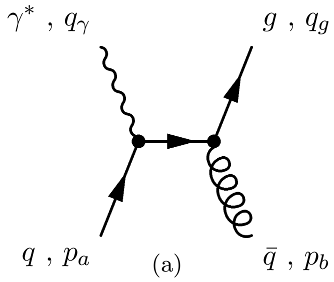

Figure 4.3: Leading order diagrams for the "Comptom" subprocess $q + g \rightarrow \gamma^* + q$.

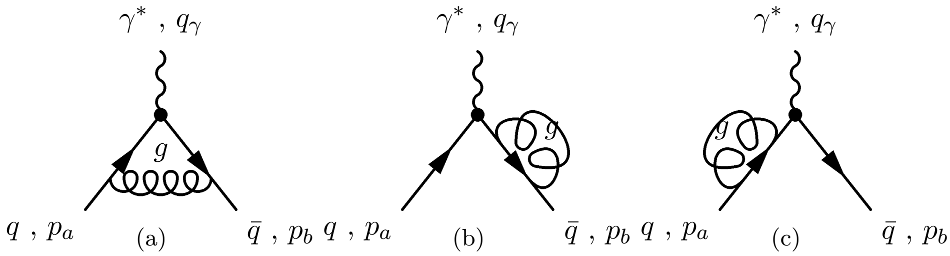

Figure 4.4: Virtual gluon corrections to the $q\bar{q}$ annihilation Born term $q + \bar{q} \rightarrow \gamma^*$.

perturbation approach not so unreasonable.
Terms, which arise from the virtual corrections in Fig. 4.2, are called "annihilation" and have two types of divergences, when gluons are soft and when they are almost collinear. These divergences also affect the "Compton" diagrams (see Fig. 4.3), so named by the analogy with the similar electromagnetic process. Fig. 4.4 illustrates three more diagrams, leading to other divergent integrals. Virtual loop divergences cancel with soft divergences, while the remaining ones are absorbed in the redefinition of parton distribution functions.
The perturbation series behaves like:

$$\begin{aligned}\sigma_{DY} &= \sigma_{naive}\left\{1+\left(\frac{8\pi}{9}-\frac{7}{3\pi}\right)\alpha_s+\cdots\right\} \\ &= \sigma_{naive}\left(1+2.05\alpha_s+\cdots\right)\end{aligned} \tag{4.18}$$

where σ_{naive} is the Born cross section. The corrections to the Drell-Yan process are quite large at first order in α_s [86, 87], suggesting that even at next order they will be quite large. However this scenario is not true and the perturbation series converge and, at least, part of it can be shown to exponentiate [88, 89]. The series in Eq. 4.18 can be written:

$$\begin{aligned}\sigma_{DY} &= \sigma_{naive}\left\{1+\left(\frac{2\pi}{9}-\frac{7}{3\pi}\right)\alpha_s+\frac{2\pi}{3}\alpha_s+\cdots\right\} \\ &= \sigma_{naive}e^{\frac{2\pi}{3}\alpha_s}\left\{1+\left(\frac{2\pi}{9}-\frac{7}{3\pi}\right)\alpha_s+\cdots\right\} \\ &= \sigma_{naive}e^{\frac{2\pi}{3}\alpha_s}\left(1-0.045\alpha_s+\cdots\right)\end{aligned} \tag{4.19}$$

which appears to be a well behaved perturbation series. For $\alpha_s = \frac{1}{3}$, it becomes:

$$\begin{aligned}\sigma_{DY} &= \sigma_{naive}e^{0.698}\left(1-0.015+\cdots\right) \\ &\approx 1.98\sigma_{naive}\end{aligned} \tag{4.20}$$

Experimentally one finds that the ratio of the predicted cross section and the measured one is around 2, in agreement with the QCD prediction. This factor takes the name of K-factor.

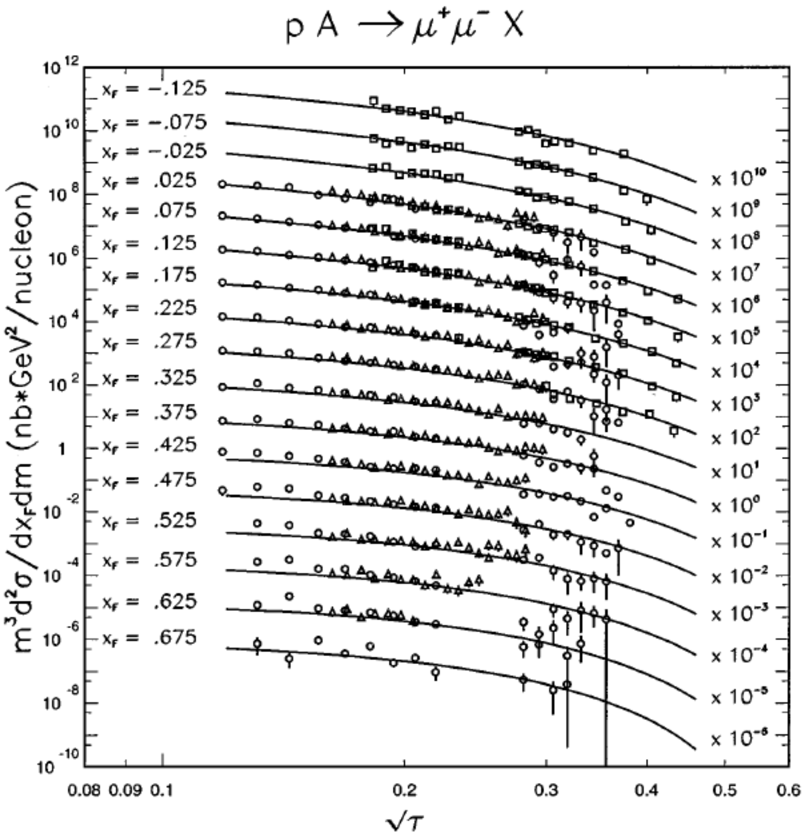

Figure 4.5: Proton induced Drell-Yan production from experiments NA3 [90] (triangles) at 400 GeV/c, E605 [91] (squares) at 800 GeV/c, and E772 [92] (circles) at 800 GeV/c. The lines are absolute NLO calculation for p + d collisions a 800 GeV/c.

Experiment	Beam and target	Momentum / $\sqrt{s}$	K-factor
NA3 [94]	$\bar{p} - p$ Pt	150	2.3 ± 0.4
NA3 [95]	p Pt	200	2.2 ± 0.4
CFS [96]	p Pt	300/400	$1.7^{+0.73}_{-0.58}$
CHFMNP [97]	pp	44, 62	1.6 ± 0.2
MNTW [98]	p W	400	1.6 ± 0.3
NA3 [99]	π^- Pt	200	2.2 ± 0.3
NA3 [99]	π^+ Pt	200	2.4 ± 0.4
NA3 [99]	$\pi^- - \pi^+$ Pt	200	2.4 ± 0.4
Omega [100]	π^- W	40	2.45 ± 0.42
Omega [100]	π^+ W	40	2.52 ± 0.49
Omega [101]	$\pi^- - \pi^+$ W	40	2.22 ± 0.41

Table 4.1: K-factor from different experiments: they all express the ratio of measured cross section and Born level cross section.

4.2.3 The K-factor

The measured Drell-Yan cross section and its theoretical computation are used to define the K-factor:

$$K(\tau) = \frac{\sigma_{exp}}{\sigma_{DY}} \tag{4.21}$$

The K-factor is defined as the ratio between the observed experimental cross section and the theoretical prediction [93] and therefore its value depends on the order α_s^n at which the computations are done. At zeroth order in α_s the K-factor has roughly a value of about 2 (see Tab. 4.1) while it is around 1 at first order (see Tab. 4.2). The K-factor is almost costant over the kinematic range $0.02 < \tau < 0.7$ and this may suggest that the perturbation expansion is not working, because a constant depencence on τ which means on s also implies a not runnig coupling costant. However the K-factor has an exponential shape and can be decomposed in terms linked to the different diagrams contributing to enhance the Drell-Yan cross section, as showed in Fig. 4.6. In this picture the continuous line is the total K-factor; the main contribution comes from virtual diagrams and divergences (dotted line); the dashed and the dot-dashed lines show the contributions coming from the annihilation and Compton diagrams, which are small, but a negative trend is noticeable.

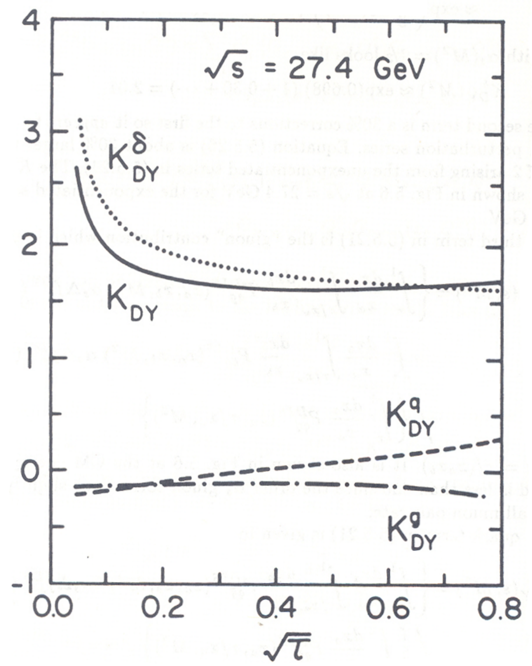

Figure 4.6: K-factor as a function of $\sqrt{\tau}$ at $\sqrt{s} = 27.4 GeV$ (full line); dotted, dashed and dot-dashed lines show contribution to K-factor from virtual, annihilation and Compton diagrams.

Experiment	Beam and target	Momentum / $\sqrt{s}$	K-factor
E288	p Pt	200/300/400	1.049 $\pm$ 0.010
E325	p Cu	200/300/400	1.112 $\pm$ 0.060
E439	p Cu	400	1.108 $\pm$ 0.009
E444	p C/Cu/W	225	1.009 $\pm$ 0.201
NA3	p Pt	200	1.105 $\pm$ 0.008
E605	p Cu	400	1.071 $\pm$ 0.010
E772	pp	800	0.641 $\pm$ 0.003
CHFMNP	pp	44, 62	1.048 $\pm$ 0.026
E537	$\bar{p}$ W	125	1.290 $\pm$ 0.007
E326	π^- W	225	1.331 $\pm$ 0.023
E615	π^- W	252	1.064 $\pm$ 0.042
NA10	π^- W	194/286	1.286 $\pm$ 0.005

Table 4.2: K-factor from different experiments [93]: they all express the ratio of measured cross section and order α_s cross section.

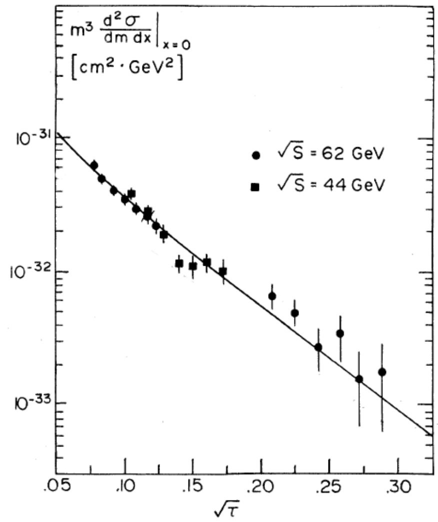

Figure 4.7: Scaling behavious of Drell-Yan cross section as a function of τ.

4.3 Scaling

A scaling behaviour can be predicted for the Drell-Yan cross section. The cross section can be written in a better way to see its independence from beam energy for a given combination of beam and target:

$$M^4 \frac{\mathrm{d}^2\sigma}{\mathrm{d}M^2\mathrm{d}x_F} = \mathcal{F}(x_F, \tau) \tag{4.22}$$

where $\mathcal{F}(x_F, \tau)$ is a function that depends on the quark content of beam and target. For $y = 0$ the scaling nature of variable τ is evident, see Fig. 4.7.

4.4 Dependence of cross section

4.4.1 Dependence of cross section on beam particle

The Drell-Yan cross section depends on the beam particle and on the atomic mass of the target material.
Ratios between cross sections for Drell-Yan production can be predicted for different beams, for example π^- and π^+. The reason of these dependence can be found in the quark composition of the hadrons in the initial state. That is clear when one looks at the ratio of cross sections for π^- and π^+ beam

particle. In the valence region, the anti-quark of the pion is of importance, thus the ratio is approximately:

$$R\left[\frac{\sigma(\pi^+)}{\sigma(\pi^-)}\right] = \frac{\int \mathrm{d}x_a \mathrm{d}x_b \bar{d}_+(x_a) d_T(x_b) e_d^2}{\int \mathrm{d}x_a \mathrm{d}x_b \bar{u}_+(x_a) u_T(x_b) e_u^2} \tag{4.23}$$

where u and d identify the u and d quark distributions and the pedices $+$ and T refer to beam and target; $e_{d,u}$ is the electric charge of quarks. In case of an isoscalar target, made of element with the same number of protons and neutrons, $u_T \equiv d_T$ getting:

$$R\left[\frac{\sigma(\pi^+)}{\sigma(\pi^-)}\right] = \frac{e_d^2}{e_u^2} = 0.25 \tag{4.24}$$

In case of hydrogen target, being $u_T \approx 2d_T$ the ratio is:

$$R\left[\frac{\sigma(\pi^+)}{\sigma(\pi^-)}\right] = 0.125 \tag{4.25}$$

4.4.2 Dependence of cross section on target atomic mass

The dependence on the atomic mass A of the target material is explained when thinking that the $q\bar{q}$ annihilation is a point-like interaction and the resulting cross section off a nucleon is the incoherent sum of the cross sections of its partons. Consequently the cross section off an atom is the incoherent sum of the cross section off its nucleon, thus justifing an A dependence:

$$\sigma(Z, A) = A^{\alpha} \sigma_0(A, Z) \tag{4.26}$$

where $\sigma_0(A, Z)$ is the Drell-Yan cross section which already takes into account the quark composition of beam and target. The expected value of α is then 1 and some measurements are shown in Tab. 4.3.

4.5 Transverse momentum distribution

In the collinear approximation the two incoming partons which annihilate have no transverse momentum. This automatically implies that the lepton pair has zero transverse momentum. On the other hand, experiments show that the Drell-Yan lepton pairs have a distribution in transverse momentum, and this can be used to infer the distribution of the partonic intrinsic $\mathbf{k}_T$.

	Beam and target	Momentum (GeV/c)	Mass range (GeV/c^2)	α
CFS [96]	p Be,Pt	400	5-11	1.007 ± 0.033
NA10 [102]	π^- C, Cu, W	280	4-8.4	0.97 ± 0.03
NA50 [103]	p on six nuclei	400	2.9-4.5	0.982 ± 0.021
NA3 [104]	π^- H_2, Pt	200	4-9	1.02 ± 0.03
NA3 [104]	π^+ H_2, Pt	200	4-9	0.95 ± 0.04
NA3 [104]	π^- H_2, Pt	150	4-9	1.00 ± 0.02
NA3 [104]	π^- H_2, Pt	280	4-9	1.00 ± 0.02

Table 4.3: Value of α for the Drell-Yan cross section dependence A^{α}.

To get an idea of how this can be done, let us build a simple model in which the partons distribution functions are factorised in two contributions, one depending on x and the other on $\mathbf{k}_T$:

$$f(x) \rightarrow f(x)h(\mathbf{k}_T^2) \tag{4.27}$$

The distribution in the transverse momentum $\mathbf{q}_T$ is then given by:

$$\frac{1}{\sigma}\frac{\mathrm{d}^2\sigma}{\mathrm{d}^2\mathbf{q}_T} = \int \mathrm{d}^2\mathbf{k}_{aT}\mathrm{d}^2\mathbf{k}_{bT}\delta^2\left(\mathbf{k}_{aT} + \mathbf{k}_{bT} - \mathbf{q}_T\right) h(\mathbf{k}_{aT}^2)h(\mathbf{k}_{bT}^2) \tag{4.28}$$

Assuming a Gaussian ansaltz for the intrinsic k$_T$ distribution, the $h(\mathbf{k}_T^2)$ is:

$$h(\mathbf{k}_T^2) = \frac{b}{\pi}e^{-bk_T^2} \tag{4.29}$$

with a $\langle \mathbf{k}_T \rangle = \sqrt{\pi/4b} \approx$ 700-800 MeV. Plugging this into Eq. 4.28 gives:

$$\frac{1}{\sigma}\frac{\mathrm{d}^2\sigma}{\mathrm{d}^2\mathbf{q}_T} = \frac{b}{2\pi}e^{\frac{-b\mathbf{q}_T^2}{2}} \tag{4.30}$$

Looking at experimental data [96], one finds that at small $\mathbf{q}_T$ the distribution is very well described (see Fig. 4.8).

However there is an excess of events at large transverse momentum. This is an evidence that QCD perturbative contributions gain importance; for large $\mathbf{q}_T$ ($\gg$M) the distribution has the following behaviour:

$$\frac{\mathrm{d}^2\sigma}{\mathrm{d}^2\mathbf{q}_T} \sim \frac{\alpha_s(\mathbf{q}_T)}{\mathbf{q}_T^4} \tag{4.31}$$

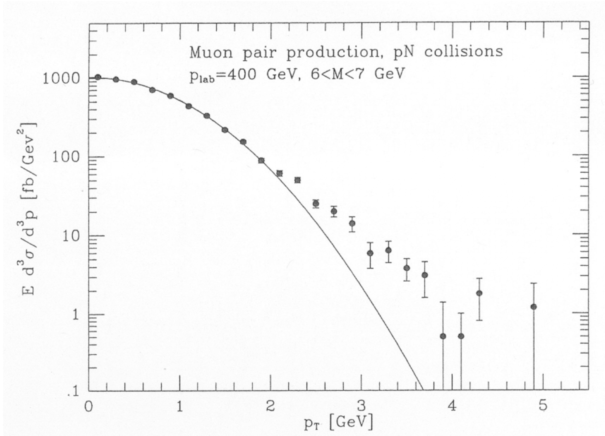

Figure 4.8: Di-lepton transverse momentum distribution from CFS collaboration [96] compared with a Gaussian intrinsic k_T distribution for the annihilating partons.

The goodness of this picture is shown in Fig. 4.9, where q_T contributions appear with the resulting prediction for the transverse momentum distribution and data point [105].
Actually it is possibile to identify three different regime zones in the q_T distribution. At low q_T the primordial k_T regime and parametrizazion are evident; at high q_T a pure QCD perturbative region describe the distribution. The intermediate region between them is correctly described with resummation. Using resummation prescriptions, which explain how to sum and to compute terms coming from non-finite diagrams, prevents the cross section from diverging as $q_T \to 0$ and makes it vanish. However at low energies ($s < 200$ GeV^2) the peak in the shape, due to the resummation result, is completely washed out by the gaussian smearing of the primordial transverse momentum.

4.6 Angular momentum distribution

The Drell-Yan angular momentum distribution can be derived from a very general expression. The angular dependent terms can be isolated in the ratio of differential cross section:

$$\frac{\mathrm{d}N}{\mathrm{d}\Omega} = \left(\frac{\mathrm{d}\sigma}{\mathrm{d}^4 q}\right)^{-1} \left(\frac{\mathrm{d}\sigma}{\mathrm{d}\Omega \mathrm{d}^4 q}\right) \tag{4.32}$$

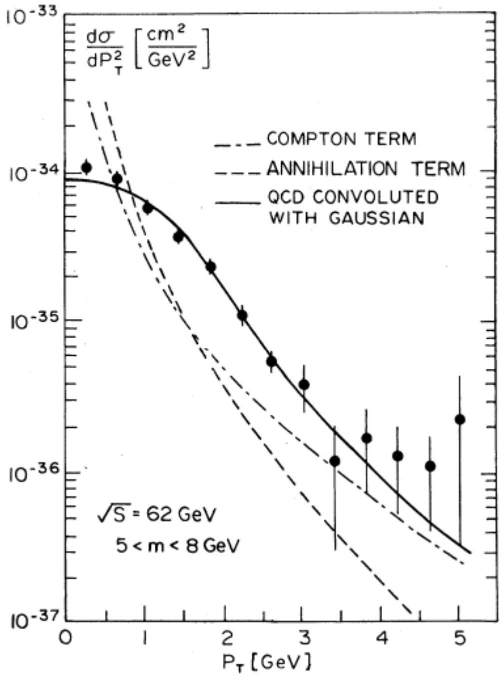

Figure 4.9: q_T distribution at $\sqrt{s} = 62$ GeV and QCD prediction with a gaussian form which models the quark intrinsic momentum distribution.

where $\mathrm{d}\Omega \equiv \mathrm{d}\cos\theta \mathrm{d}\phi$ is the solid angle of the lepton in terms of its polar and azimuthal angles in the center of mass system of the lepton pair. In the cross section appears the product of the leptonic tensor $L_{\mu\nu}$ and the hadronic tensor $W^{\mu\nu}$ [106, 107]:

$$\frac{\mathrm{d}\sigma}{\mathrm{d}^4 q \mathrm{d}\Omega} = \frac{\alpha^2}{32 s M^4} L_{\mu\nu} W^{\mu\nu} \tag{4.33}$$

where α is the structure constant, s, M and q are, as usual, the center of mass energy squared, the mass of the virtual photon and its four-vector. The lepton tensor $L^{\mu\nu}$ has already been defined previously (see Chap. 2).
The hadronic tensor is a non perturbative and complicated object that depends on the hadrons momenta; however $W^{\mu\nu}$ must satisfies some constraints such as symmetry, gauge invariance and unitarity. Defining four invariant structure functions $W_{1,2,3,4}$, an expression for $W_{\mu\nu}$ is [107]:

$$W^{\mu\nu} = -\left(g^{\mu\nu} - \frac{q^\mu q^\nu}{M^2}\right) W_1 + \tilde{P}^\mu \tilde{P}^\nu W_2 - \frac{1}{2}\left(\tilde{P}^\mu \tilde{p}^\nu + \tilde{p}^\mu \tilde{P}^\nu\right) W_3 + \tilde{p}^\mu \tilde{p}^\nu W_4 \tag{4.34}$$

where $P = P_a + P_b$, $p = P_a - P_b$, q is the virtual photon four-vector, $\tilde{P}^\mu = \left(P^\mu - q^\mu(P\cdot q)/Q^2\right)\sqrt{s})$ and $\tilde{p}^\mu = \left(p^\mu - q^\mu(p\cdot q)/Q^2\right)\sqrt{s})$.
Another decomposition of $W_{\mu\nu}$ uses the "helicity structure function": W_T, W_L, W_Δ and $W_{\Delta\Delta}$. W_T and W_L are structure functions for transversely and longitudinally polarised virtual photons, respectively, W_Δ is the single-spin-flip structure function, while $W_{\Delta\Delta}$ is the double-spin-flip one.
The hadronic tensor can be written [106, 107]:

$$\begin{aligned} W^{\mu\nu} = &-\left(g^{\mu\nu} - \frac{q^{\mu\nu}}{M^2}\right)(W_T + W_{\Delta\Delta}) - 2X^\mu X^\nu W_{\Delta\Delta} \\ &+ Z^\mu Z^\nu (W_L - W_T - W_{\Delta\Delta}) - (X^\mu Z^\nu + Z^\mu X^\nu) W_\Delta \end{aligned} \tag{4.35}$$

where X^μ, Z^ν are the axis of the dilepton rest frame orthogonal to the four-vector q^μ.
The cross section, contracting the two tensors, becomes:

$$\begin{aligned} \frac{\mathrm{d}\sigma}{\mathrm{d}^4 q \mathrm{d}\Omega} = \frac{\alpha^2}{32 s M^4}\Big[&W_T\left(1+\cos^2\theta\right) + W_L\left(1-\cos^2\theta\right) \\ &+ W_\Delta \sin 2\theta\cos\phi + W_{\Delta\Delta}\sin^2\theta\cos 2\phi\Big] \end{aligned} \tag{4.36}$$

Therefore the angular distribution can be rewritten [106]:

$$\begin{aligned} \frac{\mathrm{d}N}{\mathrm{d}\Omega} = \frac{3}{8\pi}\frac{1}{2W_T + W_L}\Big(&W_T\left(1+\cos^2\theta\right) + W_L\left(1-\cos^2\theta\right) + \\ &+ W_\Delta \sin 2\theta\cos\phi + W_{\Delta\Delta}\sin^2\theta\cos 2\phi\Big) \end{aligned} \tag{4.37}$$

Very often it is parameterized in this way [108]:

$$\frac{\mathrm{d}N}{\mathrm{d}\Omega} = \frac{3}{4\pi}\frac{1}{\lambda+3}\left[1 + \lambda\cos^2\theta + \mu\sin 2\theta\cos\phi + \frac{\nu}{2}\sin^2\theta\cos 2\phi\right] \tag{4.38}$$

where the following relations can be found:

$$\lambda = \frac{W_T - W_L}{W_T + W_L} \tag{4.39}$$

$$\mu = \frac{W_\Delta}{W_T + W_L} \tag{4.40}$$

$$\nu = \frac{2W_{\Delta\Delta}}{W_T + W_L} \tag{4.41}$$

Another parametrization of the angular distribution is [108]:

$$\frac{\mathrm{d}N}{\mathrm{d}\Omega} = \frac{3}{16\pi}\left[1 + \cos^2\theta + \frac{A_0}{2}\left(1 - 3\cos^2\theta\right) \right.$$
$$\left. + A_1 \sin 2\theta \cos\phi + \frac{A_2}{2}\sin^2\theta\cos 2\phi\right] \tag{4.42}$$

The parameters A_i are related to previous ones by the relations:

$$\lambda = \frac{2 - 3A_0}{2 + A_0} \tag{4.43}$$

$$\mu = \frac{2A_1}{2 + A_0} \tag{4.44}$$

$$\mu = \frac{2A_2}{2 + A_0} \tag{4.45}$$

and

$$A_0 = \frac{2W_L}{2W_T + W_L} \tag{4.46}$$

$$A_1 = \frac{2W_\Delta}{2W_T + W_L} \tag{4.47}$$

$$A_2 = \frac{4W_{\Delta\Delta}}{2W_T + W_L} \tag{4.48}$$

These structure functions are not uniquely defined and one has to specify a reference frame system where the photon polarisation vector is explicitely written. Common choises are to work in the Collins-Soper frame (CS) [108], or in the Gottfried-Jackson frame (GJ) [107] (also sometimes referred to as the "t-channel helicity frame"), or in the "u-channel frame".

All these frames are defined in the muon pair rest frame; for all the of them, the x-z plane is the one containing the two hadrons and the y is taken to be perpendicular to this plane. The last degree of freedom is fixed by the choice of the direction of the z axis and the three frames are related by a rotation around the y axis. In the Gottfried-Jackson frame the z axis is taken to be the direction of P_a in the muon pair rest frame; in the u-channel frame the z axis is chosen to be antiparallel to P_b direction, while in the Collins-Soper frame the z axis is the bisector of the angle between the t- and u-channel z axis, that is the direction of $P_a - P_b$. As $q_T \to 0$ the frames became indentical and ϕ becomes undefined.

The helicity structure functions are different in each frame, since their definition involves explicitly the definition of the frame axis. Therefore relations beetween the invariant structure functions and the helicity ones depends on the frame in which they are worked out. As already mentioned, the parameters acquire different values depending on the frame where they are computed. A useful transformation between the sets of coefficient λ, μ, ν, in the GJ and CS frames, is [107]:

$$\begin{pmatrix} \lambda \\ \mu \\ \nu \end{pmatrix}_{GJ} = \frac{1}{\Delta_{CS}} \begin{pmatrix} 1-\frac{1}{2}\rho^2 & -3\rho & \frac{3}{4}\rho^2 \\ \rho & 1-\rho^2 & -\frac{1}{2}\rho \\ \rho^2 & 2\rho & 1+\frac{1}{2}\rho^2 \end{pmatrix} \begin{pmatrix} \lambda \\ \mu \\ \nu \end{pmatrix}_{CS} \tag{4.49}$$

where

$$\rho = \frac{q_T}{q} \tag{4.50}$$

and

$$\Delta = 1 + \rho^2 + \frac{1}{2}\rho^2\lambda + \rho\mu - \frac{1}{4}\rho^2 \tag{4.51}$$

The reverse trasformation from the GJ frame to the CS frame is the same upon replacement of $\rho \to -\rho$ and exchange of the labels CS and GJ.
As a consequence, the values of parameters λ, μ, ν as well as A_0, A_1, A_2 depend on the reference system where they are computed. However a relation between them, called Lam-Tung sum rule, is valid whatever the frame is choosen.
The Lam-Tung sum rule [106] reads:

$$1 - \mu = 2\nu \tag{4.52}$$

This rule is a consequence of the relation between the helicity structure functions [109]:

$$W_L = 2W_{\Delta\Delta} \tag{4.53}$$

This relation is the Drell-Yan equivalent for the Callan-Gross relation in DIS[30]:

$$W_L = -W_1 + \left(\frac{\nu^2}{q^2} - 1\right) W_2 = 0 \tag{4.54}$$

The values of λ, μ, ν were measured in past experiments and the Lam-Tung sum rule was tested. In the naive Drell-Yan model, in the collinear approximation and with no gluon emissions, one obtaines $\lambda = 1$ and $\mu = \nu = 0$. However QCD effects [110, 111] can both lead to $\lambda \neq 1$ and $\mu, \nu \neq 0$,

but even in this case the Lam-Tung sum rule is expected to be followed, being unaffected by QCD corrections [106].
λ, μ, ν are shown as a function of $\mathbf{q}_T$ in Figs. 4.10, which reports values measured in E615 and NA10 experiments [112, 113]. Furthermore a violation

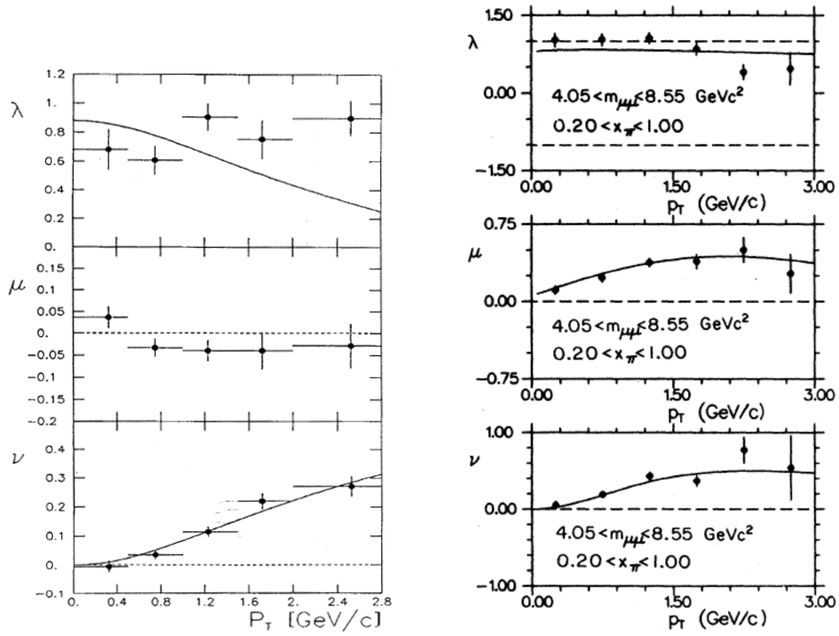

(a) (b)

Figure 4.10: λ, μ and ν parameters as a function of the virtual photon trasverse momentum from NA10 (CS frame) (a) [113] and E615 (GJ frame) (b) [112].

of the Lam-Tung sum rule was measured in the E615 experiment whose mean values for λ, μ and ν are reported together with NA10 and E866 ones [114].

4.7 TMD PDFs in the angular distribution

The impact of the non-zero values of the parameters λ, μ, ν is the presence of additional modulation in the angular distribution, in particular a $\cos 2\phi$ modulation due to the non-vanishing ν value.
Several attempts have been made to interpret these data. One idea was that a factorization-breaking QCD vacuum may lead to a correlation be-

	$\pi^- + W$ 252 GeV/c (E615)	$\pi^- + W$ 194 GeV/c (NA10)	p + d 800 GeV/c (E866)
$\langle\lambda\rangle$	1.17 ± 0.06	0.83 ± 0.04	1.07 ± 0.07
$\langle\mu\rangle$	0.09 ± 0.02	0.008 ± 0.010	0.003 ± 0.013
$\langle\nu\rangle$	0.169 ± 0.019	0.091 ± 0.009	0.027 ± 0.010
$\langle 1-\lambda-2\nu\rangle$	0.51 ± 0.07	0.01 ± 0.04	0.12 ± 0.07
x_a range	$0.2 \to 1.0$	$0.2 \to 1.0$	$0.15 \to 0.85$
x_b range	$0.04 \to 0.38$	$0.1 \to 0.4$	$0.02 \to 0.24$

Table 4.4: Mean values of the λ, μ and ν parameters and the quantity $1-\lambda-2\nu$ for three Drell-Yan measurements. The kinematic coverages in x_a and x_b are also listed.

tween the transverse spin of the anti-quark in one hadron and that of the quark in the other hadron [115]. This would result in a non-zero $\cos 2\phi$ angular dependence consistent with the data of the experiments. Then helicity flip in the instanton model was suggested as another mechanism for factorization-breaking QCD vacuum [116]. In the literature other models have been proposed, based on higher-twist effects from quark-anti-quark binding in pions [117, 118]. These models predict the behaviour of λ and ν in qualitative agreement with the data of NA10 and E615, but they are sctricly applicable only in the $x_\pi \to 1$ region, while data of both experiments exhibit non-perturbative effects over a much broader kinematic region.
Recently, Boer pointed out [119] that the $\cos 2\phi$ angular dependances observed in NA10 and E615 could be due the k_T dependent parton distribution function $h_1^\perp$. Model calculations for the nucleon and pion Boer-Mulders functions have been carried out [120, 121, 122, 123] and can describe the ν beahaviour observed in NA10. A compatible fact in support to the Boer-Mulders function model comes from the data of E866 Drell-Yan process induced by proton. The expectation of the azimuthal dependence in the angular distribution for this data is small due to the fact that the Boer-Mulders functions are small for sea quarks [119].

4.7.1 General expression of the cross-section

Lot of work has been done to explain these effects and prediction for new Drell-Yan experiments were carried out; these experiments focus on the

Drell-Yan process regarding the spin polarisation of the two hadrons. Very recently a paper has been published [124]: it analyses the Drell-Yan angular cross section as a function of TMD PDFS. The COMPASS Drell-Yan proposal deals with unpolarised and singly polarised Drell-Yan, therefore from [124] only the related part is discussed.
Unpolarised Drell-Yan means that both beam particles and target are unpolarised; when Drell-Yan is referred as single polarised, it means that the target nucleons are transversely polarised, while, the beam particles are not. The notation used below is the same of the COMPASS proposal for future program and it is similar to the one of [124]. So far the target polarisation vector S has not been defined: In the center of mass frame it reads:

$$S_{CM} = \left(-S_L \frac{|P_{bCM}|}{M_b}, \mathbf{S}_T \cos\phi_S, \mathbf{S}_T \sin\phi_S, S_L \frac{P^0_{CM}}{M_b} \right) \tag{4.55}$$

In the laboratory frame is:

$$S_{LF} = (0, \mathbf{S}_T \cos\phi_S, \mathbf{S}_T \sin\phi_S, S_L) \tag{4.56}$$

where ϕ_S is the azimuthal angle of the trasverse polarisation in the laboratory frame. The angular Drell-Yan cross section has the general expression:

$$\begin{aligned} \frac{\mathrm{d}\sigma}{\mathrm{d}^4q\mathrm{d}\Omega} = \frac{\alpha^2}{Bq^2} \Big\{ \Big[& \left(1+\cos^2\theta\right) F_U^1 + \left(1-\cos^2\theta\right) F_U^2 \\ & + \sin 2\theta F_U^{\cos\phi} \cos\phi + \sin^2\theta F_U^{\cos 2\phi} \cos 2\phi \Big] \\ & + S_L \big(\sin 2\theta F_L^{\sin\phi} \sin\phi + \sin^2\theta F_L^{\sin 2\phi} \sin 2\phi \big) \\ & + |\mathbf{S}_T| \Big[\left(F_T^{\sin\phi_S} + \cos^2\theta \tilde{F}_T^{\sin\phi_S} \right) \sin\phi_S \\ & + \sin 2\theta \left(F_T^{\sin(\phi+\phi_S)} \sin(\phi+\phi_S) + F_T^{\sin(\phi-\phi_S)} \sin(\phi-\phi_S) \right) \\ & + \sin^2\theta \left(F_T^{\sin(2\phi+\phi_S)} \sin(2\phi+\phi_S) + F_T^{\sin(2\phi-\phi_S)} \sin(2\phi-\phi_S) \right) \Big] \Big\} \end{aligned} \tag{4.57}$$

where $B = 4\sqrt{(P_a \cdot P_b)^2 - M_a^2 M_a^2}$ represents the flux of the incoming hadrons and, if hadron masses can be neglected, it can be written $B = 2s = 2(P_a \cdot P_b)^2$. The F are structure functions which depend on the invari-

ant quantities $P_a \cdot q$, $P_b \cdot q$ and q^2 but not on θ, ϕ and ϕ_S; the subscript of the structure function corresponds to the polarisation state of the target nucleon, while in the superscript the azimuthal modulation is specified.
The following equation express the relation of the structure functions above with the one in [124]:

$$
\begin{aligned}
F_T^{\sin\phi_S} &= F_{UT}^1 + F_{UT}^2 \\
\tilde{F}_T^{\sin\phi_S} &= F_{UT}^1 - F_{UT}^2 \\
F_T^{\sin(\phi+\phi_S} &= \frac{1}{2}(F_{UT}^{\sin\phi} + F_{UT}^{\cos\phi}) \\
F_T^{\sin(\phi-\phi_S} &= \frac{1}{2}(F_{UT}^{\sin\phi} - F_{UT}^{\cos\phi}) \\
F_T^{\sin(2\phi+\phi_S} &= \frac{1}{2}(F_{UT}^{\sin 2\phi} + F_{UT}^{\cos 2\phi}) \\
F_T^{\sin(2\phi-\phi_S} &= \frac{1}{2}(F_{UT}^{\sin 2\phi} - F_{UT}^{\cos 2\phi})
\end{aligned}
$$

In Eq. 4.57 the part of the cross section that survives after integration over the angles ϕ and ϕ_S can be factorised:

$$\hat{\sigma}_U = (F_U^1 + F_U^2)(1 + A_U^1 \cos^2\theta) \tag{4.58}$$

thus allowing the cross section to be written as:

$$
\begin{aligned}
\frac{\mathrm{d}\sigma}{\mathrm{d}^4 q \mathrm{d}\Omega} = \frac{\alpha^2}{Bq^2}\hat{\sigma}_U \Big\{ \Big(1 + D_{\sin 2\theta} A_U^{\cos\phi} \cos\phi + D_{\sin^2\theta} A_U^{\cos 2\phi} \cos 2\phi \Big) \\
+ S_L \Big(D_{\sin 2\theta} A_L^{\sin\phi} \sin\phi + D_{\sin^2\theta} A_L^{\sin 2\phi} \sin 2\phi \Big) \\
+ |\mathbf{S}_T| \Big[\Big(A_T^{\sin\phi_S} + D_{\cos^2\theta} \tilde{A}_T^{\sin\phi_S} \Big) \sin\phi_S \\
+ D_{\sin 2\theta} \Big(A_T^{\sin(\phi+\phi_S} \sin(\phi+\phi_S + A_T^{\sin(\phi-\phi_S} \sin(\phi-\phi_S) \Big) \\
+ D_{\sin^2\theta} \Big(A_T^{\sin(2\phi+\phi_S} \sin(2\phi+\phi_S + A_T^{\sin(2\phi-\phi_S} \sin(2\phi-\phi_S) \Big) \Big] \Big\}
\end{aligned}
\tag{4.59}
$$

where the depolarisation factors have been introduced:

$$D_{f(\theta)} = \frac{f(\theta)}{1 + A_U^1 \cos^2\theta} \tag{4.60}$$

and the asymmetries $A_{U,L,T}^{f(\phi,\phi_S)}$ are:

$$
\begin{aligned}
A_U^1 &= \frac{F_U^1 - F_U^2}{F_U^1 + F_U^2} \\
A_U^{\cos\phi} &= \frac{F_U^{\cos\phi}}{F_U^1 + F_U^2} \\
A_U^{\cos 2\phi} &= \frac{F_U^{\cos 2\phi}}{F_U^1 + F_U^2} \\
A_L^{\sin\phi} &= \frac{F_L^{\sin\phi}}{F_U^1 + F_U^2} \\
A_L^{\sin 2\phi} &= \frac{F_L^{\sin 2\phi}}{F_U^1 + F_U^2} \\
A_T^{\sin\phi_S} &= \frac{F_T^1 + F_T^2}{F_U^1 + F_U^2} \\
\tilde{A}_T^{\sin\phi_S} &= \frac{F_T^1 - F_T^2}{F_U^1 + F_U^2} \\
A_T^{\sin(\phi+\phi_S)} &= \frac{F_T^{\sin\phi} + F_T^{\cos\phi}}{2(F_U^1 + F_U^2)} \\
A_T^{\sin(\phi-\phi_S)} &= \frac{F_T^{\sin\phi} - F_T^{\cos\phi}}{2(F_U^1 + F_U^2)} \\
A_T^{\sin(2\phi+\phi_S)} &= \frac{F_T^{\sin 2\phi} + F_T^{\cos 2\phi}}{2(F_U^1 + F_U^2)} \\
A_T^{\sin(2\phi-\phi_S)} &= \frac{F_T^{\sin 2\phi} - F_T^{\cos 2\phi}}{2(F_U^1 + F_U^2)}
\end{aligned}
$$

In this formalism the λ, μ and ν parameters are:

$$
\begin{aligned}
\lambda &= A_U^1 \\
\mu &= A_U^{\cos\phi} \\
\nu &= 2A_U^{\cos 2\phi}
\end{aligned}
$$

At leading order, the structure functions in the Drell-Yan cross section can be expressed as a convolution of TMD PDFs [124]. The convolution of PDF is expressed by:

$$
\mathcal{F}[w(\mathbf{k}_{Ta}, \mathbf{k}_{Tb}) f_a \bar{f}_b] = \frac{1}{N_c} \int \mathrm{d}^2\mathbf{k}_{aT} \mathrm{d}^2\mathbf{k}_{bT} \delta^{(2)}(\mathbf{q}_T - \mathbf{k}_{aT} - \mathbf{k}_{bT}) \cdot
$$

$$w(\mathbf{k}_{Ta}, \mathbf{k}_{Tb}) \times \left[f_a^q(x_a, \mathbf{k}_{Ta}^2) f_b^{\bar{q}}(x_b, \mathbf{k}_{Tb}^2) + f_a^{\bar{q}}(x_a, \mathbf{k}_{Ta}^2) f_b^q(x_b, \mathbf{k}_{Tb}^2)\right] \quad (4.61)$$

where $N_c = 3$. Defining $\mathbf{h} = \mathbf{q_T}/|\mathbf{q}_T|$, the structure functions are, at leading order in the CS frame:

$$F_U^1 = \mathcal{F}\left[f_1, \bar{f}_1\right] \quad (4.62)$$

$$F_U^2 = 0 \quad (4.63)$$

$$F_U^{\cos\phi} = 0 \quad (4.64)$$

$$F_U^{\cos 2\phi} = \mathcal{F}\left[\frac{2(\mathbf{h}\cdot\mathbf{k}_{Ta})(\mathbf{h}\cdot\mathbf{k}_{Tb}) - 2\mathbf{k}_{Ta}\mathbf{k}_{Tb}}{M_a M_b} h_1^\perp \bar{h}_1^\perp\right] \quad (4.65)$$

$$F_L^{\sin\phi} = 0 \quad (4.66)$$

$$F_L^{\sin 2\phi} = \mathcal{F}\left[\frac{2(\mathbf{h}\cdot\mathbf{k}_{Ta})(\mathbf{h}\cdot\mathbf{k}_{Tb}) - 2\mathbf{k}_{Ta}\mathbf{k}_{Tb}}{M_a M_b} h_1^\perp \bar{h}_{1L}^\perp\right] \quad (4.67)$$

$$F_T^1 = \mathcal{F}\left[\frac{(\mathbf{h}\cdot\mathbf{k}_{Tb})}{M_b} f_1 \bar{f}_{1T}^\perp\right] \quad (4.68)$$

$$F_T^2 = 0 \quad (4.69)$$

$$F_T^{\sin(\phi-\phi_S)} = 0 \quad (4.70)$$

$$F_T^{\sin(\phi+\phi_S)} = 0 \quad (4.71)$$

$$F_T^{\sin(2\phi+\phi_S)} = -\mathcal{F}\Bigg[\frac{1}{2M_a M_b^2}\Big(2(\mathbf{h}\cdot\mathbf{k}_{bT})\Big[2(\mathbf{h}\cdot\mathbf{k}_{aT})(\mathbf{h}\cdot\mathbf{k}_{bT}) - (\mathbf{k}_{aT}\cdot\mathbf{k}_{bT})\Big] - \mathbf{k}_{bT}^2(\mathbf{h}\cdot\mathbf{k}_{aT})\Big)\Bigg] h_1^\perp \bar{h}_{1T}^\perp \quad (4.72)$$

$$F_T^{\sin(2\phi-\phi_S} = -\mathcal{F}\left[\frac{\mathbf{h}\cdot\mathbf{k}_{aT}}{M_a} h_1^\perp \bar{h}_1\right] \quad (4.73)$$

Noticing that six structure functions out of twelve are zero, Eq. 4.59 simplifies in:

$$\begin{aligned}\frac{d\sigma^{LO}}{d^4q d\Omega} = \frac{\alpha^2}{Bq^2}\hat{\sigma}_U^{LO}\Big\{&(1 + D_{\sin^2\theta}^{LO} A_U^{\cos 2\phi}\cos 2\phi) \\ &+ S_L D_{\sin^2\theta}^{LO} A_L^{\sin 2\phi}\sin 2\phi \\ &+ |\mathbf{S}_T|\Big[A_T^{\sin\phi_S}\sin\phi_S + D_{\sin^2\theta}^{LO}\Big(A_T^{\sin(2\phi+\phi_S)}\sin(2\phi+\phi_S) \\ &+ A_T^{\sin(2\phi-\phi_S)}\sin(2\phi-\phi_S)\Big)\Big]\Big\}\end{aligned} \quad (4.74)$$

with

$$\hat{\sigma}_U^{LO} = F_U^1(1 + A_U^1\cos^2\theta) \quad (4.75)$$

coming from the simplification of $\hat{\sigma}_U$ and the depolarisation factor at LO:

$$D_{f(\theta)}^{LO} = \frac{f(\theta)}{1+\cos^2\theta} \tag{4.76}$$

The non-zero asymmetries are at LO:

$$A_U^{\cos 2\phi}(LO) = \frac{F_U^{\cos 2\phi}}{F_U^1} \tag{4.77}$$

$$A_L^{\sin 2\phi}(LO) = \frac{F_L^{\sin 2\phi}}{F_U^1} \tag{4.78}$$

$$A_T^{\sin \phi_S}(LO) = \frac{F_T^1}{F_U^1} \tag{4.79}$$

$$A_T^{\sin(2\phi+\phi_S)}(LO) = \frac{F_T^{\sin(2\phi+\phi_S}}{2F_U^1} \tag{4.80}$$

$$A_T^{\sin(2\phi-\phi_S)}(LO) = \frac{F_T^{\sin(2\phi-\phi_S}}{2F_U^1} \tag{4.81}$$

Therefore, with longitudinally and transversely polarised targets, it is possible to extract all the structure functions and in particular, from the measurement of asymmetries:

- $A_U^{\cos 2\phi} \rightarrow$ Boer-Mulders functions of incoming hadrons

- $A_L^{\sin 2\phi} \rightarrow$ Boer-Mulders functions of beam hadron and $h_{1L}^{\perp}$ function of the target nucleon

- $A_T^{\sin \phi} \rightarrow$ Sivers function of the target nucleon

- $A_T^{\sin(2\phi+\phi_S)} \rightarrow$ Boer-Mulders functions of beam hadron and pretzelosity function of the target nucleon

- $A_T^{\sin(2\phi-\phi_S)} \rightarrow$ Boer-Mulders functions of beam hadron and transversity function of the target nucleon

4.7.2 Extraction of asymmetries and estimation of statistical errors

The extraction of asymmetries is perfomed using Eq. 4.74. After integration over the q_T and θ the angular distribution, in (x_a, x_b) bin is:

$$\begin{aligned}\frac{\mathrm{d}N(x_a, x_b, \phi, \phi_S)}{\mathrm{d}\phi, \mathrm{d}\phi_S} = N(x_a, x_b)\Bigg\{ &\left(1 + \frac{1}{2}A_U^{\cos 2\phi}\cos 2\phi\right) \\ &+ fS_L\frac{1}{2}A_L^{\sin 2\phi}\sin 2\phi \\ &+ f|\mathbf{S}_T|\Big[A_T^{\sin\phi_S}\sin\phi_S + \frac{1}{2}\Big(A_T^{\sin(2\phi+\phi_S)}\sin(2\phi+\phi_S) \\ &+ \ A_T^{\sin(2\phi-\phi_S)}\sin(2\phi-\phi_S)\Big)\Big]\Bigg\}\end{aligned} \tag{4.82}$$

where f is the dilution factor and $N(x_a, x_b)$ is the number of events in a given (x_a, x_b) bin:

$$N(x_a, x_b) \propto \int \mathrm{d}q_T^2\mathrm{d}\phi_S\mathrm{d}\cos\theta\mathrm{d}\phi\frac{\mathrm{d}\sigma}{\mathrm{d}x_a\mathrm{d}x_b\mathrm{d}q_T^2\mathrm{d}\phi_S\mathrm{d}\cos\theta\mathrm{d}\phi} \tag{4.83}$$

Using Fourier projection, the corresponding asymmetries are:

$$A_U^{\cos 2\phi}(x_a, x_b) = 4\frac{\int \mathrm{d}\phi_S\mathrm{d}\phi\frac{\mathrm{d}N(x_a,x_b,\phi,\phi_S}{\mathrm{d}\phi\mathrm{d}\phi_S}\cos 2\phi}{N(x_a, x_b)} \tag{4.84}$$

$$A_L^{\sin 2\phi}(x_a, x_b) = \frac{4}{fS_L}\frac{\int \mathrm{d}\phi_S\mathrm{d}\phi\frac{\mathrm{d}N(x_a,x_b,\phi,\phi_S}{\mathrm{d}\phi\mathrm{d}\phi_S}\sin 2\phi}{N(x_a, x_b)} \tag{4.85}$$

$$A_T^{\sin\phi_S}(x_a, x_b) = \frac{2}{f|\mathbf{S}_T|}\frac{\int \mathrm{d}\phi_S\mathrm{d}\phi\frac{\mathrm{d}N(x_a,x_b,\phi,\phi_S}{\mathrm{d}\phi\mathrm{d}\phi_S}\sin\phi_S}{N(x_a, x_b)} \tag{4.86}$$

$$A_T^{\sin(2\phi+\phi_S)}(x_a, x_b) = \frac{4}{f|\mathbf{S}_T|}\frac{\int \mathrm{d}\phi_S\mathrm{d}\phi\frac{\mathrm{d}N(x_a,x_b,\phi,\phi_S}{\mathrm{d}\phi\mathrm{d}\phi_S}\sin(2\phi+\phi_S)}{N(x_a, x_b)} \tag{4.87}$$

$$A_T^{\sin(2\phi-\phi_S)}(x_a, x_b) = \frac{4}{f|\mathbf{S}_T|}\frac{\int \mathrm{d}\phi_S\mathrm{d}\phi\frac{\mathrm{d}N(x_a,x_b,\phi,\phi_S}{\mathrm{d}\phi\mathrm{d}\phi_S}\sin(2\phi-\phi_S)}{N(x_a, x_b)} \tag{4.88}$$

with their statistical errors:

$$\delta A_U^{\cos 2\phi}(x_a, x_b) = 2\frac{\sqrt{2}}{\sqrt{N(x_a, x_b)}} \tag{4.89}$$

$$\delta A_L^{\sin 2\phi}(x_a, x_b) = \frac{2}{fS_L}\frac{\sqrt{2}}{\sqrt{N(x_a, x_b)}} \tag{4.90}$$

$$\delta A_T^{\sin\phi_S}(x_a, x_b) = \frac{1}{f|\mathbf{S}_T|}\frac{\sqrt{2}}{\sqrt{N(x_a, x_b)}} \tag{4.91}$$

$$\delta A_T^{\sin(2\phi+\phi_S)}(x_a, x_b) = \frac{2}{f|\mathbf{S}_T|}\frac{\sqrt{2}}{\sqrt{N(x_a, x_b)}} \tag{4.92}$$

$$\delta A_T^{\sin(2\phi-\phi_S)}(x_a, x_b) = \frac{2}{f|\mathbf{S}_T|}\frac{\sqrt{2}}{\sqrt{N(x_a, x_b)}} \tag{4.93}$$

4.7.3 On the naïve T-odd Sivers and Boer-Mulders functions

One remind has to be done. In Chap. 2 it was stated that the Sivers and the Boer-Mulders TMD PDFs are naïve T-odd and their definition contains a gauge-link operator which ensures the colour-gauge invariance and makes the Sivers and the Boer-Mulders functions process dependent. Therefore it is possible to show that the $f_{1T}^{\perp}$ and the $h_1^{\perp}$ functions extracted from Drell-Yan processes and those obtained from SIDIS should have opposite signs [41]:

$$f_{1T}^{\perp}(x, \mathbf{k}_T^2)|_{SIDIS} = -f_{1T}^{\perp}(x, \mathbf{k}_T^2)|_{DY} \tag{4.94}$$

$$h_1^{\perp}(x, \mathbf{k}_T^2)|_{SIDIS} = -h_1^{\perp}(x, \mathbf{k}_T^2)|_{DY} \tag{4.95}$$

An experimental verification of the sign-reversal property of the Sivers and Boer-Mulders functions would be a test of the present understanding of QCD.

4.8 Prediction of asymmetries

Some predictions for the Sivers asymmetry in the dimuon mass range 4 GeV/c^2 < M < 9 GeV/c^2 for the Drell-Yan process $\pi p \to \mu^+\mu^- + X$ are available. They are shown in Fig. 4.11 as a function of x_F with the expected COMPASS statistical errors for the specifici mass region. As can be seen, a statistical error of 0.02 is reachable. The statistical error, however, depends on number of bins, and a size of 0.01 is reachable when only one bin is considered. In Fig. 4.11, the black solid and dashed lines come from [125]; the black dot-dashed line is described in [126]. The three upper red curves represent the asymmetry estimated in the same mass range (4 GeV/c^2 < M < 9 GeV/c^2) and q_T integrated up to 1 GeV/c, obtained in [127]: the central curve (solid line) shows the expected asymmetry value and dot-dashed lines

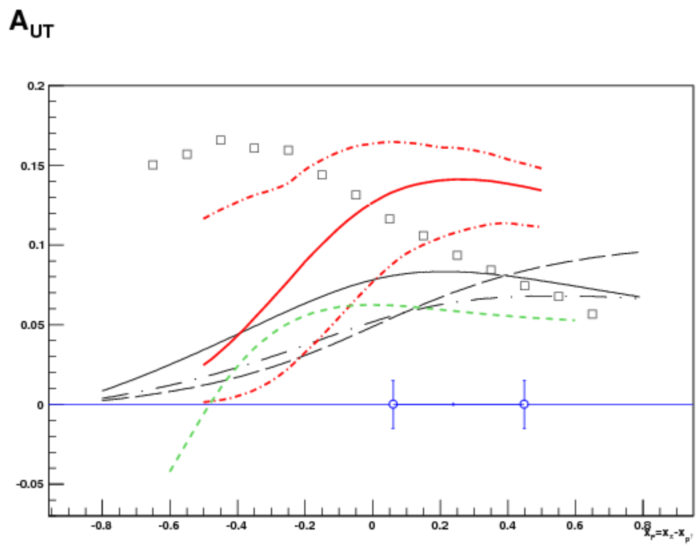

Figure 4.11: Theoretical predictions and expected statistical errors on Sivers asymmetry in Drell-Yan process $\pi p \rightarrow \mu^+\mu^- + X$ in the dimuon mass range 4 GeV/c^2 < M < 9 GeV/c^2.

represents the corridor of errors on the predicted asymmetry value. The predictions obtained in [128] and in [129] are shown by squares and green short-dashed line correspondingly.

Chapter 5

2007 and 2008 Drell-Yan beam test

At the end of runs in 2007 and 2008, two tests were performed to provide useful information about the idea of a Drell-Yan program at COMPASS. The collected data helped to understand the possibility of this measurement, suggesting solutions and allowing to test the whole apparatus in conditions as similar as possible to what is required for the Drell-Yan program.

5.1 2007 beam test

The test performed in 2007 had the aim to see how the spectrometer behaves for Drell-Yan measurement. However, the length of the test could not allow to see any Drell-Yan event because of the low cross-section and therefore the J/ψ peak was taken as a reference. Still, it was very important because the NH_3 polarised target was installed and in operation, and thus, continuosly monitoring the target temperature, it has been possible to check the effect of a hadron beam passing through the target.

5.1.1 Experimental conditions

The test was scheduled for the very last 24 hours of the 2007 run, on the 11^{th} and 12^{th} November. Two days were not enough to modify the spectrometer in an important way. The configuration was the same as for the muon transversity data taking. So all the detectors were present, in particular the six BMS were installed in the beam line and were measuring beam particle momenta at the end of the beam line. The beam consisted of negative pions with momentum of 160 Gev/c, the spill was adjusted to 9.8 s length and the intensity was 1-2$\times 10^7$ pions/spill. The intensity was increased from 8×10^6 pions/spill to 2×10^7 pions/spill keeping under control the response of spectrometer and of the data acquisition system. Once the running conditions looked stable and all checks were fine, the data acquisition started: 36 runs were collected and produced. Tab. 5.1 summarizes the information about analysed runs.

5.1.2 The trigger

The ideal trigger for Drell-Yan events is capable to recognise a pair of muons arising from the target region. Such a kind of trigger does not exist in the COMPASS apparatus, therefore the existing triggers had to be modified. The available COMPASS trigger, already discussed in Sec. 3.8, is able to identify tracks of muons coming from the target region, but only for muons that cross the second half of the spectrometer, thus leaving uncovered the *Large Angle Spectrometer*. The solution was to use the hadronic calorimeter in the first spectrometer to trigger on muons, using it with two thresholds, at 0.7 MIPS and 2.5 MIPS: signals in this window were considered coming from muons. A beam trigger was also available.
All trigger signals were arranged to get the following kind of triggers:

1. beam trigger
    - Bit 7
2. one muon in the SAS
    - Bit 0: ladder trigger (LT)
    - Bit 4: outer trigger (OT)
    - Bit 8: middle trigger (IT)
3. one muon in the SAS and one muon in LAS
    - Bit 2: LT and H_μ
    - Bit 3: OT and H_μ
    - Bit 1: MT and H_μ

More clever triggers were not implemented. The case of both muons in SAS was covered by the trigger type 2; the case of both muons in LAS was not implemented. The three trigger types were pre-scaled in order to have the same event sample from each of them, respectively 30, 30 and 5 for type 1, 2 and 3. Fig. 5.1 shows the composition in trigger bit of all reconstructed events for all the available data.

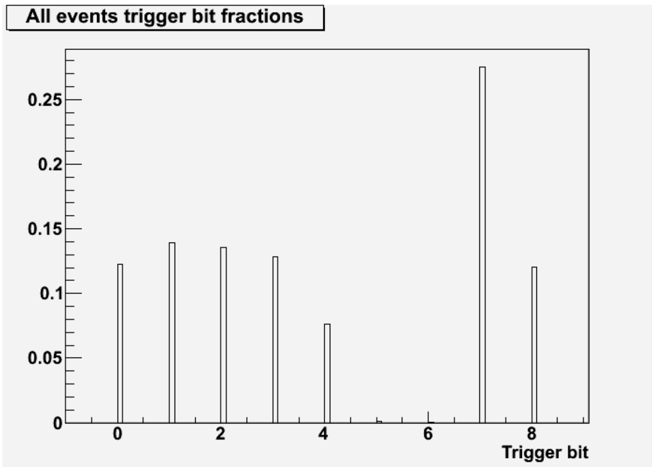

Figure 5.1: Trigger bit composition of all reconstructed Drell-Yan events for 2007 beam test.

5.1.3 The collected data

The data were analysed twice, but only the second processing will be discussed here, since it was the one used for the analysis. In total 95223873 events were analysed, organized in 36 runs and 1881 spills. All informations are summarised in Tab. 5.1.

5.1.4 Analysis of data

Out of 95223873 events, only 92973 were tagged as Drell-Yan events; from them 86574 muon pairs were identified and satisfied selection rules. Criteria for pre-selecting events required the reconstruction of at least one $\mu^+\mu^-$ pair.

Rules for choosing di-muons were the following:

- if only one di-muon is found, keep it

run #	flux	# events	# spills	# tagged	# di-muons
64358	4.87E+007	332240	3	307	282
64359	5.23E+007	394124	3	409	372
64360	1.15E+007	78378	1	91	85
64361	5.35E+007	380968	3	381	355
64362	7.52E+008	1744847	25	1939	1774
64363	1.41E+009	2176594	32	2145	1965
64364	2.22E+009	3441698	59	3787	3507
64365	1.14E+008	528098	8	591	531
64373	3.88E+007	14145	5	12	10
64374	5.12E+007	717606	8	648	593
64375	2.31E+008	2279817	33	2345	2205
64376	6.46E+008	2102414	30	2047	1932
64377	2.41E+009	4624246	82	4656	4320
64378	3.02E+009	5062505	90	5029	4728
64379	4.27E+003	1550	6	0	0
64380	3.90E+007	345846	6	358	323
64381	3.55E+009	5520766	100	5705	5304
64382	2.98E+009	5026641	100	4972	4647
64383	7.25E+008	1910212	34	1866	1723
64384	7.85E+008	2038299	39	2026	1913
64385	1.06E+009	2853351	54	2780	2577
64386	1.19E+008	822847	18	826	756
64387	2.86E+009	4584472	100	4626	4318
64388	2.90E+009	4618302	100	4388	4108
64391	2.84E+009	4702012	100	4613	4298
64392	2.72E+009	4489625	100	4330	4022
64393	4.91E+008	1708024	35	1553	1441
64395	2.88E+009	4765028	100	4574	4294
64396	1.26E+008	882949	19	851	773
64397	2.22E+009	4735221	100	4403	4092
64398	2.19E+009	4770947	100	4454	4150
64399	1.88E+009	4229933	91	3966	3696
64401	4.52E+007	347071	6	332	299
64405	1.39E+009	8906588	200	8231	7705
64407	4.60E+008	3135404	70	2881	2677
64408	1.32E+008	951105	21	851	799
TOTAL	4.35E+010	95223873	1881	92973	86574

Table 5.1: Runs used in 2007 DY beam analysis

- otherwise, if more than one di-muon is found then:
  - take the *BestPrimaryVertex* primary vertex, if it has at least one di-muon
  - otherwise, take the primary vertex with at least one di-muon with lowest χ^2
  - otherwise, since no primary vertexes were found, take all secondary vertexes with di-muons

In addition the vertexes were required to be inside the target volume. The target volume was identified with a 140 cm long cylinder with 2 cm radius, centered in $z = 0$.

The low statistics could not allow to introduce any trigger selection.

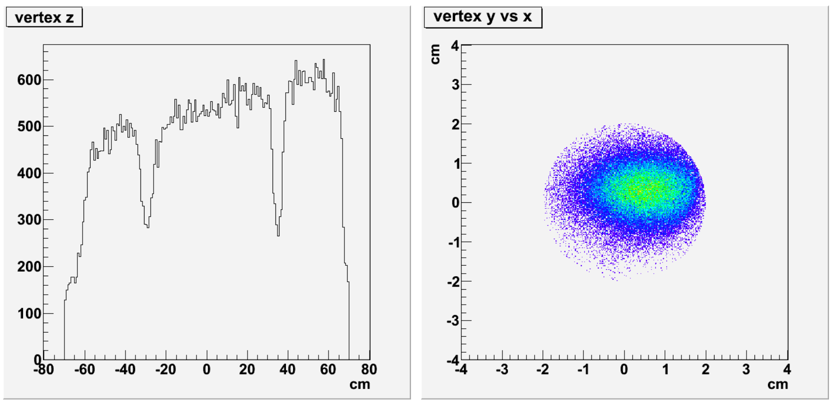

(a) (b)

Figure 5.2: (a) z position and (b) y vs x position of reconstructed vertexes with at least one $\mu^+\mu^-$ pair.

Out of 84300 recontructed vertexes, one has:

- 82102 with 1 di-muon (97.4%)
- 2141 with 2 di-muons (2.5%)
- 40 with 3 di-muons
- 16 with 4 di-muons
- 0 with 5 di-muons

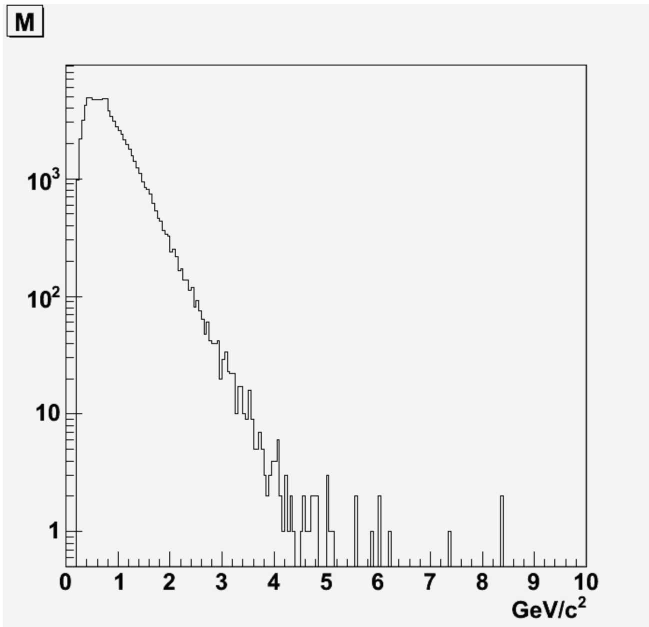

Figure 5.3: Di-muon invariant mass distribution pre-selected events.

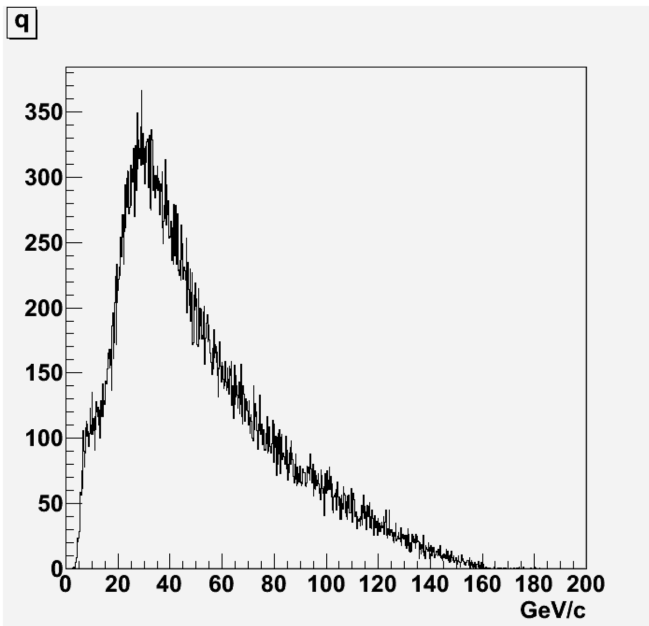

Figure 5.4: Di-muon momentum distribution pre-selected events.

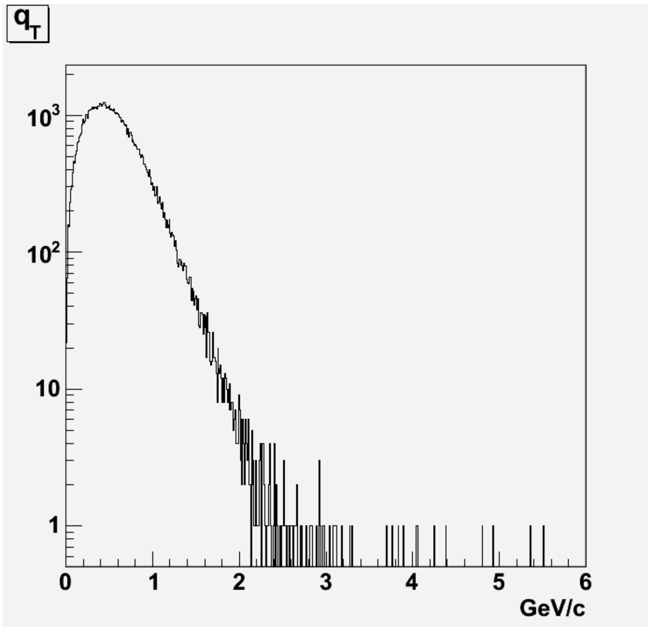

Figure 5.5: Di-muon transverse momentum distribution pre-selected events.

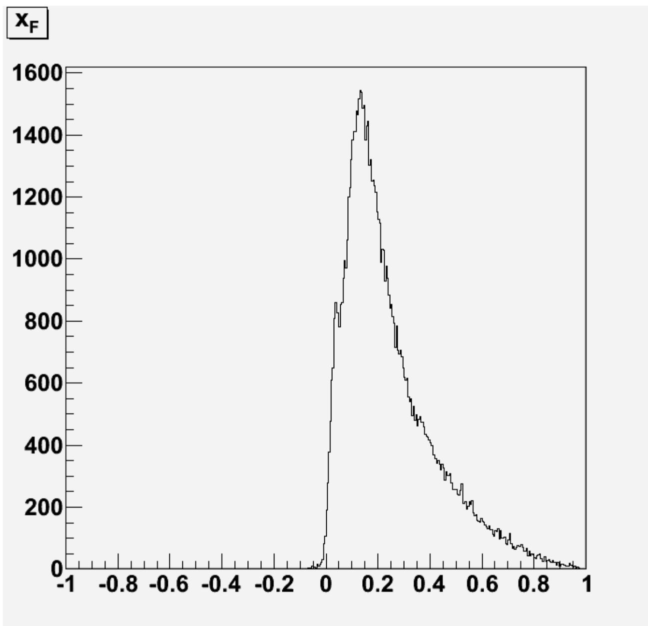

Figure 5.6: x_F variable distribution pre-selected events.

- 1 with 6 di-muons

The kinematic variables for the Drell-Yan events were calculated and plotted. Figs. 5.3, 5.4, 5.5 and 5.6 show the reconstructed photon invariant mass, its momentum q, its transverse momentum q_T and the x_F distribution. The quantities x_F, $x_a \equiv x_\pi$ and $x_b \equiv x_p$ were calculated using the following non approximated formula were used:

$$x_\pi = \frac{M}{\sqrt{s}} \frac{q_0 + q_L}{\sqrt{q_T^2 + M^2}} \tag{5.1}$$

$$x_p = \frac{M}{\sqrt{s}} \frac{q_0 - q_L}{\sqrt{q_T^2 + M^2}} \tag{5.2}$$

$$x_F = \frac{2q_L}{\sqrt{2}} \frac{1}{\sqrt{1 + \frac{M^2}{q_T^2}}} \tag{5.3}$$

where q_0, q_L, q_T and M are the energy, the longitudinal and the transverse momentum and the mass of the di-muon and $\sqrt{s}$ is the available energy in the center of mass frame. Indeed the collinear approximation cannot be used in the COMPASS kinematic region, where transverse effects are not negligible. For value of s^2 below 300-350 GeV^2/c^4 the q_T distribution, as well as the $x_{\pi,p}$ variables, start to become sensible to the intrinsic parton momentum. The best M region to study the Drell-Yan process is the one far from resonances, indeed the region for M between 4 GeV/c^2 and 9 GeV/c^2, avoiding the J/ψ and the Υ resonances. However in Fig. 5.3 few events are in this region; this is resonable because of the smallness of the Drell-Yan cross section and because of the shortness of the test. Therefore the Jψ peak was taken as a reference point to estimate the Drell-Yan event rate.
In the M distribution, the J/ψ peak can be hardly seen and the analysis proceeded in the direction of trying to decrease the background and enhance the searched signal. The following cuts were applied:

1. z coordinate of last meaured point of each μ tracks greater than 1495 cm (ZLast > 1495)

2. z coordinate of reconstructed vertex greater than -62 cm (vx_z > -62)

3. transverse momentum of each muon of the pair greater than 0.1 GeV/c ($p_T > 0.1$)

4. number of radiation length crossed by each muon greater than 30 (XX0 > 30)

5. $\alpha = \frac{p_L^{\mu^+} - p_L^{\mu^-}}{p_L^{\mu^+} + p_L^{\mu^-}}$ > -0.6

The cuts have the following explanations.
Cut 1 and cut 4 apply two strong requirements for muon identification and they are based on the MuonWall1 detector: the combination of these two enforce the fact that muon tracks have crossed the absorber in MuonWall1 and produced hits in its second half.
Cut 2 removes reconstructed vertexes coming from interaction of beam in material in front of the target (see Fig. 5.2(a).
Cut 3 was introduced to remove a peak present in the transverse momentum distribution of muons; these particles were probably beam particles misidentified as muons and therefore with low transverse momentum (see Fig. 5.7)
Cut 5 is understandable when looking at the Armenteros plot of the di-

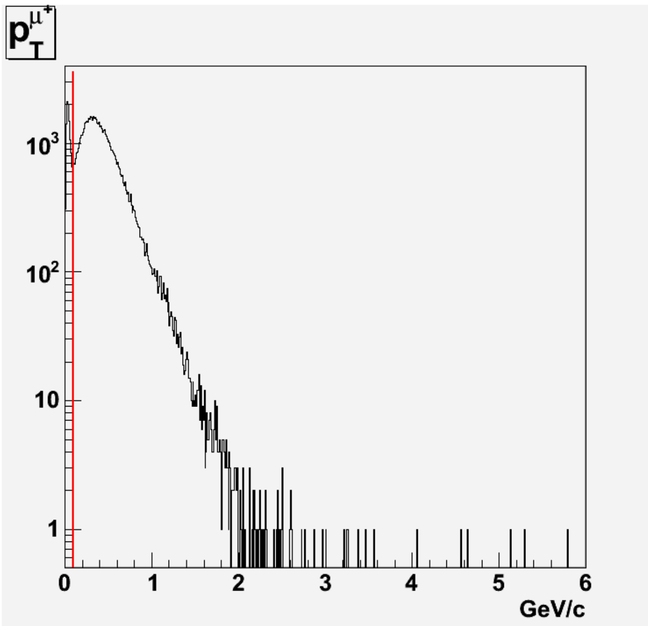

Figure 5.7: Transverse momentum distribution of positive muons. The vertical red line shows Cut 3.

muon pairs (see Fig. 5.8): it is possible to distinguish a region for values of α below -0.6 more populated and with no correspondance at positive α. Being the variable α constructed as the difference of longitudinal momentum of positive muon and longitudinal momentum of negative muon over the sum, it appears that lot of combinations comes with the negative particle carrying a bit momentum, while nothing similar exists for positive ones. This is consistent with the fact that negative muons are contaminated with misidentified beam particles. Thus, being this background in this regione to high, the cut was introduced. The invariant mass and the transverse

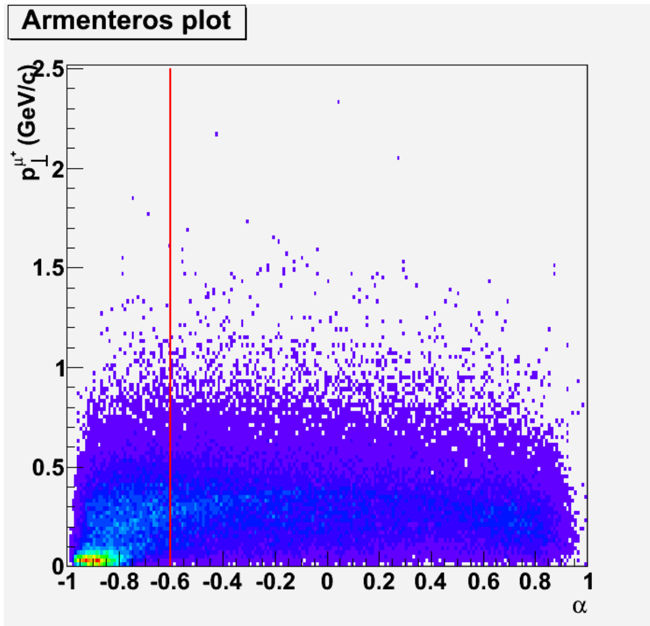

Figure 5.8: Armenteros plot of the di-muon pairs. The vertical red line shows Cut 4.

	# di-muons	%
Before cuts	86574	100%
ZLast > 1495	71401	82.5%
vx_z > -62	69922	80.8%
$p_T > 0.1$	65133	75.2%
XX0 > 30	40493	46.8%
$\alpha >$ -0.6	25200	29.1%

Table 5.2: Di-muon population after each cut.

momentum distributions of di-muons are shown in Figs. 5.9 and 5.10. The x_F, x_π and x_p distributions are shown in Figs. 5.11, 5.12(a) and 5.12(b).

A fit was performed on the invariant mass distribution with a decreasing

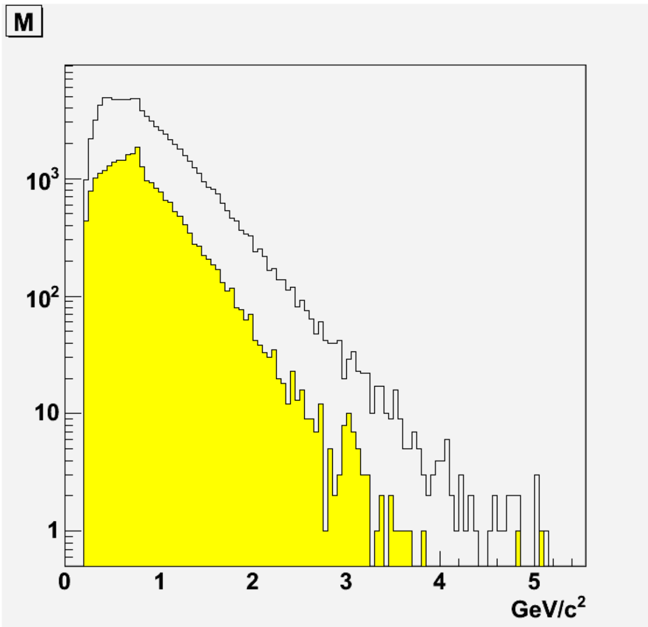

Figure 5.9: Di-muon invariant mass distribution for pre-selected events and after all cuts (yellow).

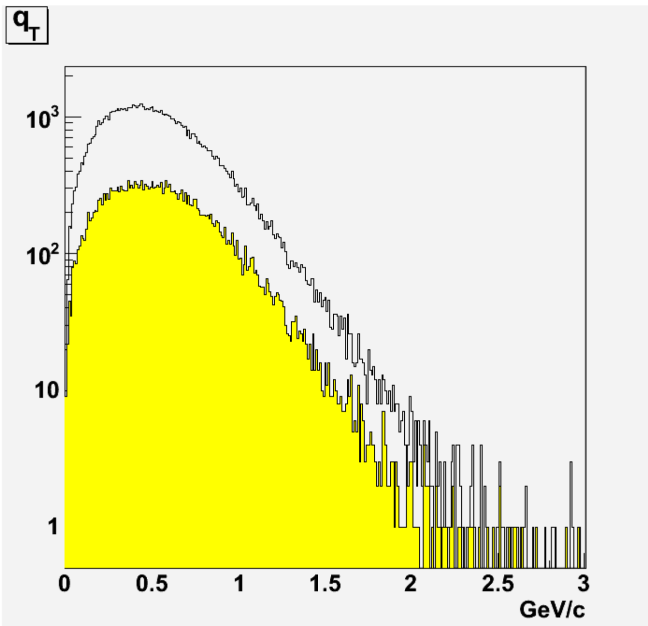

Figure 5.10: Di-muon transverse momentum distribution for pre-selected events and after all cuts (yellow).

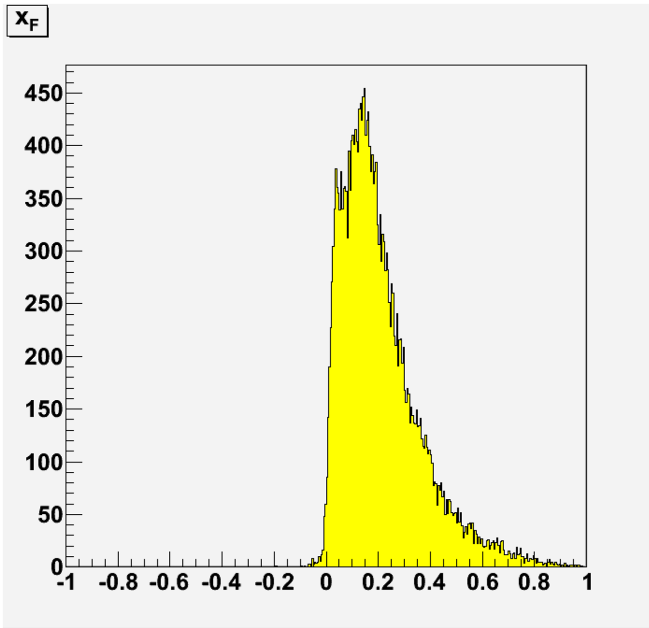

Figure 5.11: x_F variable distribution after all cuts.

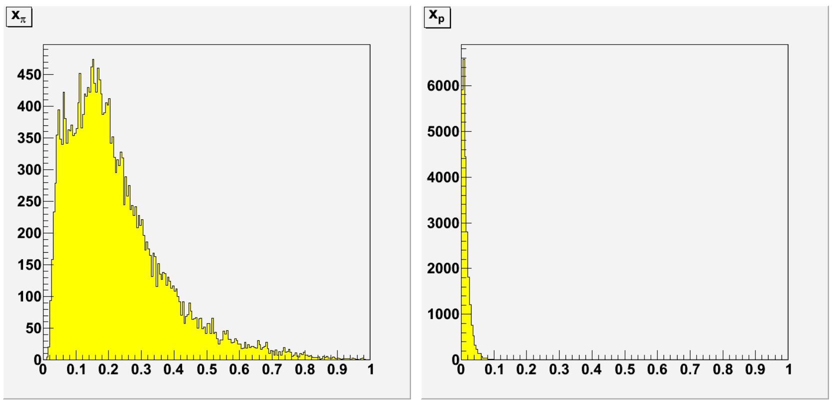

(a) (b)

Figure 5.12: x_π (a) and x_p distributions after all cuts.

exponential and a Gaussian curve over the range 1.5 GeV/c^2 < M < 3.8 GeV/c^2 with binned likelihood method to take into account the low statistics in the bins close to the upper range limit. The exponential curve fits the background, while the Gaussian fits the J/ψ peak. The formula used is:

$$\frac{N}{50\ MeV/c^2} = p_0 e^{p_1 \cdot M} + \frac{p_2 \cdot 0.05}{\sqrt{2\pi} p_4} e^{-\frac{1}{2}\left(\frac{M-p_3}{p_4}\right)^2} \tag{5.4}$$

The result of the fit is (21 $\pm$ 6) J/ψ; the mass and the width of the J/ψ are

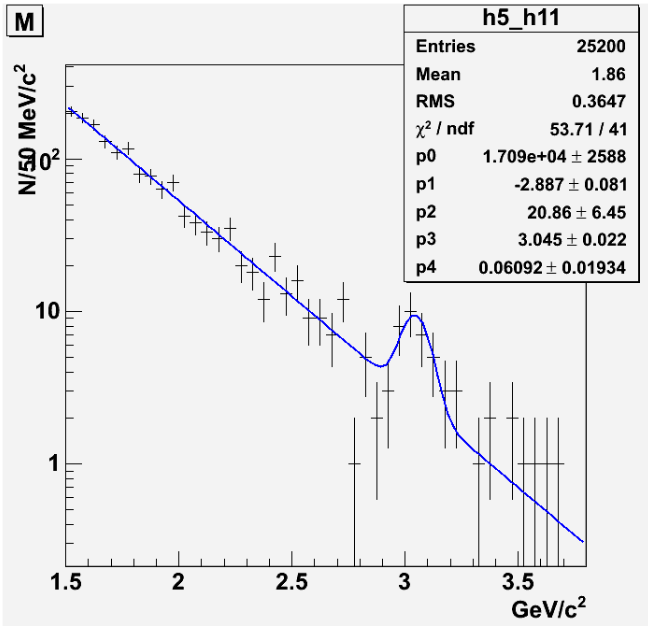

Figure 5.13: Fit on the invariant mass distribution between 1.5 GeV/c^2 < M < 3.8 GeV/c^2.

(3.05 $\pm$ 0.02) GeV/c^2 and (61 $\pm$ 10) MeV/c^2. The position of the J/ψ is in good agreement with the PDG value, while the width is entirely determined by the resolution of the spectrometer in this mass range in the configuration of the test.

5.1.5 Comparison with the expected number of J/ψ.

The number of expected Jψ can be computed and compared with the fitted number. However the number of expected J/ψ used for the comparison is not the one extracted in the previous subsection, but the number fitted when it is required that the event was triggered by the type 3 trigger, which

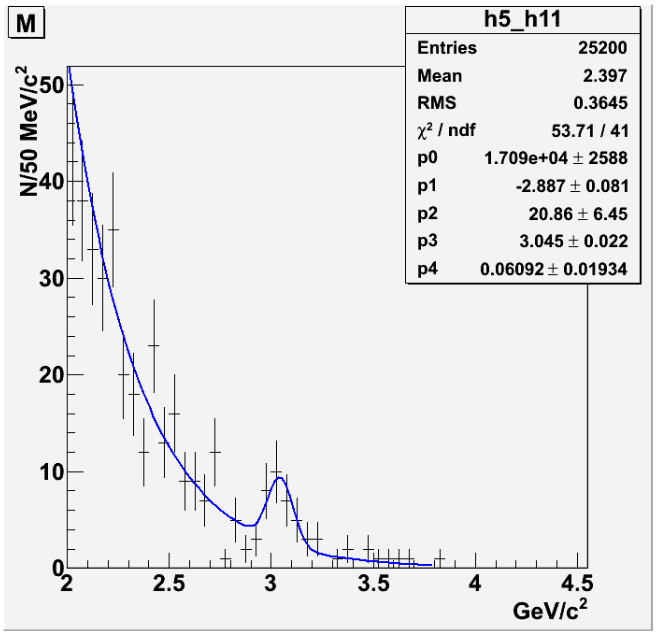

Figure 5.14: Zoom on the invariant mass distribution and fitted curve.

indicate the presence of two muons. Fig. 5.15 shows the distribution of the di-muon invariant mass and the fitted curve; the number of J/ψ is 15 $\pm$ 5. The cross section for Jψ production from pion beam on a fixed target can be found in literature and it is $\sigma_{\pi p} = (6.5 \pm 0.9)$ nb/proton [130]. Then the event rate can be computed using:

$$R_{J/\psi} = L\sigma_{\pi p} d_{spill} n_{spill} \epsilon \tag{5.5}$$

where L is the luminosity, d_{spill} is the effective duration of the spill, n_{spill} is the number of spills per day. ϵ is the total efficiency:

$$\epsilon = \Omega \epsilon_{rec} \epsilon_{trig} \epsilon_{SPS} \epsilon_{spectro} \tag{5.6}$$

where Ω is the COMPASS geometrical acceptance for di-muon events (see Sec. 6.6.3), ϵ_{rec}, ϵ_{trig}, ϵ_{SPS}, $\epsilon_{spectro}$ are respectively the estimated efficiencies for the reconstruction, the trigger, the beam delivery and the spetromecter. The values of these parameters are summarised in Tab. 5.3. The luminosity for a beam intensity of $6 \cdot 10^7$ π^-/s, which is the beam intensity proposed for the Drell-Yan program, is $L = 1.67 \cdot 10^{33}$ cm^{-2}s^{-1} for a 120 cm long NH_3 target. Assuming all the mentioned values, one can compute a rate of 37233

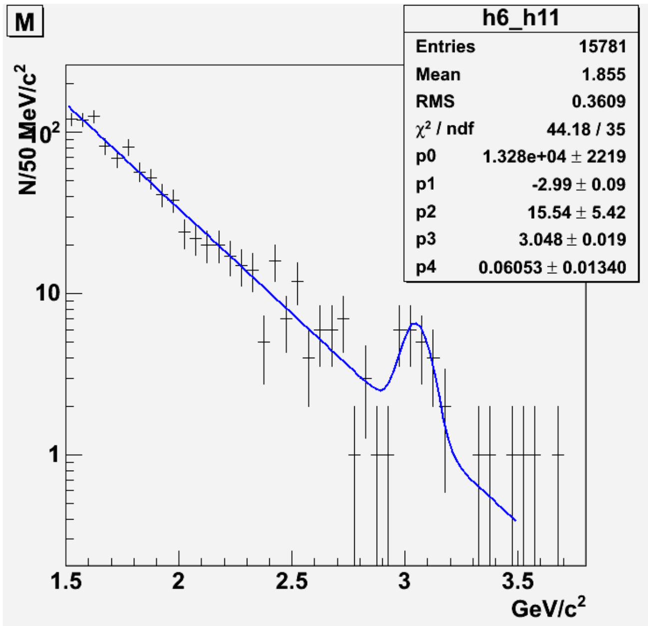

Figure 5.15: Fit on the invariant mass distribution between 1.5 GeV/c^2 < M < 3.8 GeV/c^2 with type 3 trigger request.

	Value
Ω	0.4
ϵ_{rec}	0.8
ϵ_{trig}	0.9
ϵ_{SPS}	0.8
$\epsilon_{spectro}$	0.6
n_{spill}	5000 day^{-1}
d_{spill}	4.9 s

Table 5.3: Summary of values used to compute the Jψ event rate.

J/ψ/day. Thus a prediction for the observed J/ψ can be carried out using the integrated flux computed from the analysis (Tab. 5.1). In addition, one has to take into account a few more factors:

- 40%: effectiveness of the di-muon trigger (from simulation)
- $\frac{1}{5}$: prescaling factor
- $\frac{1}{0.8}$: this factor corrects ϵ_{SPS}
- 0.8: correction to ϵ_{trig}

The result of the computation leads to the total number of expected J/ψ for the whole data taking, with the specified trigger selection:

$$37233 \cdot 0.4 \cdot \frac{1}{5} \cdot \frac{1.43 \cdot 10^{10}}{6 \cdot 10^{7} \cdot 5000 \cdot 4.9} \cdot \frac{1}{0.8} 0.8 = 29 \tag{5.7}$$

The major contribution of error comes from the flux and can be estimated around 30%. This comes from inconstencies in the flux computation from the first and the second production of data. Thus the error is 10.
This number can be directly compared with 15 $\pm$ 5. The agreement is not perfect but the two values are consistent.

5.2 2008 beam test

At the end of the run of year 2008, a second test run was performed. One aim of this test was a better study of the response of the spectrometer to Drell-Yan events. The test was limited by the absence of a hadron absorber placed after the target to reduce the total particle flux. Another aim of the test was a radioprotection measurement by the CERN radioprotection group to study the effects of a high intensity beam in the experimental hall.

5.2.1 Experimental conditions

The test was foreseen for the end of run 2008, in November. However the run was stopped in advance as a consequence of the intervention for the LHC accident. The North Area was not involved directly in the accident, but repair work required access along the beam line delivering proton to the primary target where the COMPASS beam is produced. Therefore the test

was anticipated to the beginning of October and lasted less than one day (from 3 pm 3^{rd} October to 8 am 4^{th} October) and no special setup could be prepared.
In 2008 COMPASS started data taking with hadron beams and liquid H_2 target in search of exotics and the spectrometer was configured for hadron data taking, whose main differences from muon data taking are: presence of a Recoil Proton Detector (RPD) around the target; unpolarised liquid hydrogen target; movement of detectors located after the RICH more downstream.
A one interaction long polyethylene ($[CH_2CH_2]_n$) target was positioned in front of the hydrogen target to simulate the foreseen target for Drell-Yan program. Beam consisted of a negative pion with momentum of 190 GeV/c.

5.2.2 The trigger

The trigger was not arranged like in 2007 test run. For the spectroscopy run only LT and MT were available as well as beam trigger. This means that the trigger was only able to identify events with one muon in SAS. This non ideal configuration results in the fact that a lower number of di-muons is present in the data with respect to 2007 beam test.

5.2.3 Analysis of data

The pre-selection of events and di-muons followed critearia similar to those of the 2007 data analysis. Vertexes were required to be inside the volume of the hydrogen target and of the polyethylene target.

- polyethylene target: -245 cm < vx_z < -227 cm, r < 2
- liquid hydrogen target: -68.5 cm < vx_z < -28.5 cm, r < 1.75

The relevant numbers are summarised in Tab. 5.4: 254337733 events were collected and 29533 di-muon pairs were reconstructed.
As expected the statistics is low and it is not possible to produce an analysis similar to what was done with 2007 data. Moreover the cuts, which are used to enforce the muon idenfication (Cut 1 and Cut 4) decrease the statistics to about 24000 di-muons.
In the Figs. 5.17, 5.18 and 5.19 distributions of M, q and q_T are shown.
Fig. 5.17 shows that above 4 GeV/c^2, the distribution of the invariant mass

run #	flux	# events	# spills	# tagged	# di-muons
71366	3.14E+09	12975085	66	2609	1712
71367	8.28E+08	6499456	32	1531	1031
71368	1.51E+09	7302649	33	1557	1042
71370	1.96E+09	7116690	36	1282	891
71371	3.73E+09	13548466	63	2380	1649
71372	5.06E+09	18417365	83	3269	2163
71377	5.35E+09	17741086	89	1781	1373
71378	1.28E+09	4701008	22	875	554
71381	2.02E+09	6767550	36	1084	686
71382	3.73E+08	1257207	7	239	172
71383	9.43E+09	31606838	160	4908	3196
71384	1.19E+10	39899793	201	7703	4993
71385	7.91E+09	26607108	135	4779	3190
71386	7.19E+09	24206933	124	4350	2857
71389	1.06E+09	3565477	18	424	285
71390	9.49E+08	3175810	17	605	385
71393	5.60E+08	1809168	10	297	194
71400	4.28E+08	1442696	14	170	113
71401	2.81E+09	9448887	51	1600	1084
71405	1.98E+08	662951	4	36	22
71407	4.65E+09	15585510	90	2909	1941
TOTALE	7.23E+10	254337733	1291	44388	29533

Table 5.4: Runs used in 2008 DY beam analysis

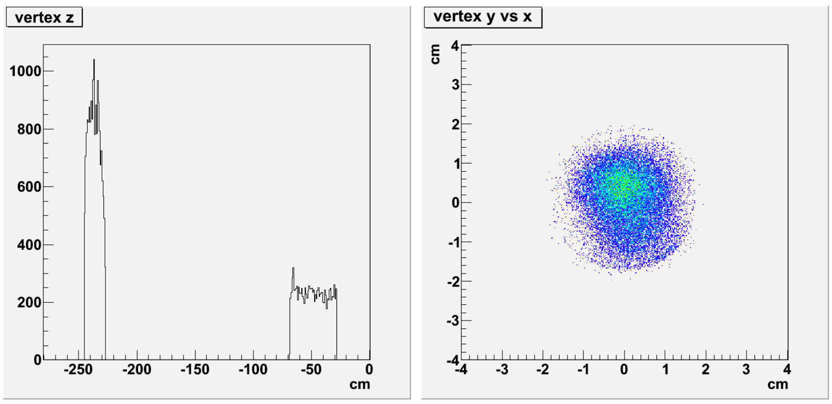

(a) (b)

Figure 5.16: (a) z position and (b) y vs x position of reconstructed vertexes with at least one $\mu^+\mu^-$ pair.

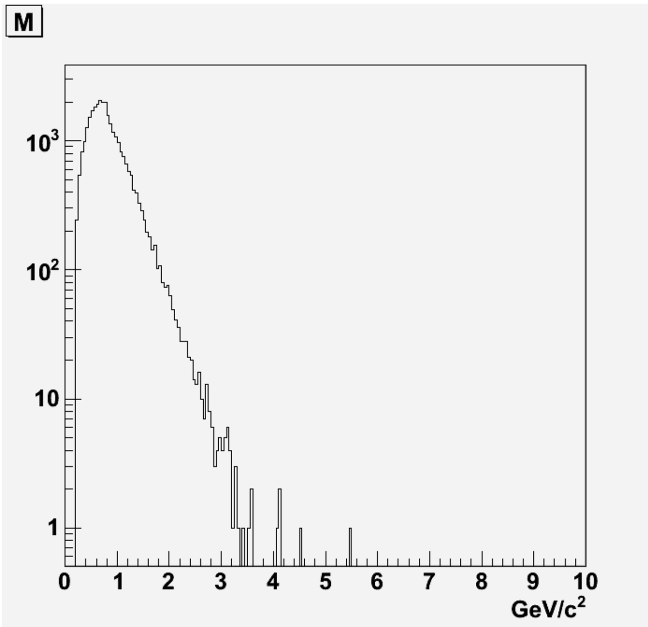

Figure 5.17: Di-muon invariant mass distribution pre-selected events from 2008 data.

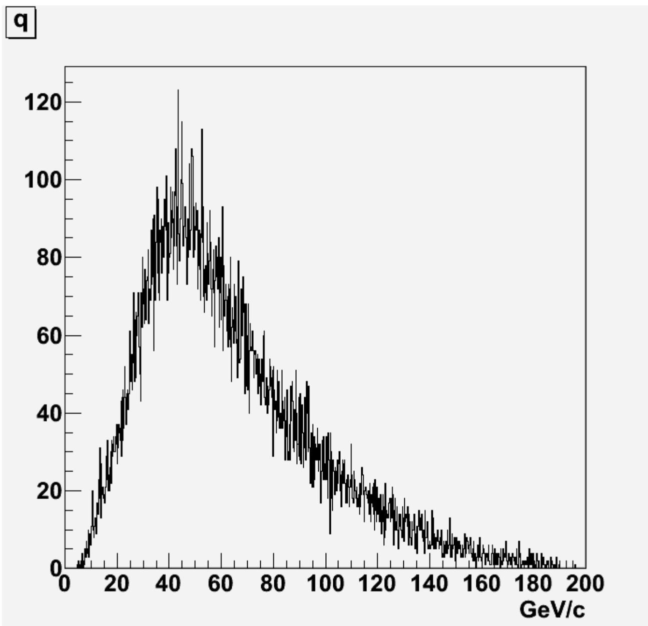

Figure 5.18: Di-muon momentum distribution pre-selected events from 2008 data.

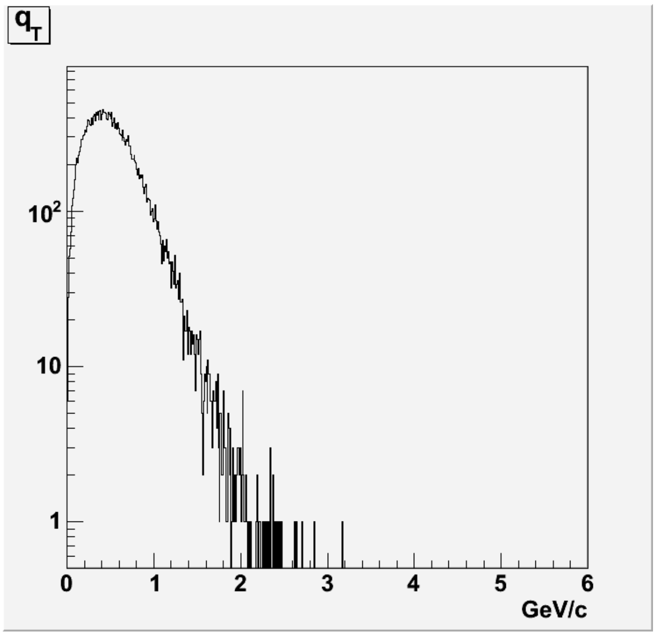

Figure 5.19: Di-muon transverse momentum distribution pre-selected events from 2008 data.

is empty, thus confirming that a dedicated trigger for Drell-Yan events in LAS is needed.

5.2.4 2008 test: conclusions

The 2008 Drell-Yan test heavily suffered the lack of preparation due to the unforeseen end of run which forced the test to be anticipated of more than a month. From a physics point of view, the lack of a muon trigger which would have helped directly resulted in a lower di-muon statistic, despite the total number of recorded data, which counts more than twice the 2007 statitics. As for 2007, the number of expected J/ψ statistics can be computed. The following naive estimation can be done starting from the number of the expected J/ψ in 2007. The main differences between 2007 and 2008 are taken into account by the following factors:

- 1.66: the flux in 2008 was higher than in 2007
- $\frac{0.01}{0.4}$: ratio correcting the effectiveness of the trigger. Only 1% of di-muon events are contained in the SAS

- $10.4^{0.925}$: correction for the different target material. J/ψ producetion cross section has an atomic mass dependence A^{α} with $\alpha = 0.925$ [103]; the polyethylene effective atomic mass is 10.4.

All other contributions are not considered; efficiencies are assumed to be the same as the ones in 2007. From [130] cross section value does not change when beam momentum changes from 160 GeV/c to 190 GeV/c. Thus, correcting the value for 2007, for 2008 one gets (11 ± 5) expected J/ψ for the whole data taking. The collected statistic does not justify a rigorous fit to the invariant mass distribution showed in Fig. 5.17, but the number is not in disagreement with the few events in the region around 3 GeV/c^2.

Chapter 6

Monte Carlo studies

In this chapter the work on the Monte Carlo simulation for the Drell-Yan proposal at COMPASS is presented. It covers different topics and it represents the starting point to estimate the spectrometer capabilities and expectations for the Drell-Yan program. Hovewer simulations are still on going and the work presented here is not to be considered definitive.

6.1 Introduction

At COMPASS, the Drell-Yan process will be studied with a negative pion beam on the polarised NH_3 target. The program requires changes to the experimental setup. These changes are few and invasive but important to this specific project. Among them, one has a large impact on the spectrometer: a hadron absorber is needed to reduce the particle flux after the target. Another important needed upgrade to the spectrometer is a dedicated trigger, to be positioned in the first part of the apparatus, whose aim is to identify di-muon pairs coming from the target region and possibly separate events coming from the absorber, where also Drell-Yan events are produced.
The reasons of inserting a hadron absorber can be found in the cross section for this reaction which is very small. The obvious solution is to get a higher luminosity by increasing the beam intensity. As a common result, all detectors of any experiments will have a high occupancy, coming from the flux of particles produced by all the other interactions occurring between beam and all the material along the beam line.

The trigger plays an important role, too. The higher the luminosity, the higher the event rate that a data acquisition system has to digest. Planes of hodoscopes can be arranged to create a trigger pointing to the target region from where, if a hadron absorber separates target and spectrometer, likely only muon pairs emerge. In this way a second motivation for the absorber is highlighted: it helps the muon identification.
However the use of absorber and trigger does not guarantee that all di-muon events are true Drell-Yan events because other reactions have the same signal and they produce two muons in the final state. The main contributions come from:

- decays of D mesons from open-charm production
- di-lepton decays of $\rho(770)$, $\omega(782)$, ...
- Bethe-Heitler muon pairs
- accidental coincidences with muons from π decay

The beam itself contributes to the background due to its muon component. In particular in COMPASS, the pion beam is a secondary beam which is driven by a long line to the experimental hall and along the beam line pion can decay in flight.
Moreover, the invariant mass distribution of di-muon pairs is characterised by the presence of the two resonances J/ψ and Υ, respectively at about 3-3.5 GeV/c^2 and around 9.5 GeV/c^2 invariant masses. The resonance peaks represent a disturbing signal and a safe choice is to reject events from those regions of invariant mass.

6.2 The hadron absorber and multiple scattering

The presence of a hadron absorber has nevertheless a negative impact on the tracking of muons which cross it. The multiple scattering makes harder the event reconstruction and can also deteriorate it. Muons, being charged particles, when traversing a medium, are deflected by many small-angle scatterings. These deflections are due to the Coulomb scattering off the nuclei of the medium. The Coulomb scattering distribution is well represented by the theory of Molière [131] and it is roughly a Gaussian. Its sigma θ_0, which is equivalent to the mean scattering angle θ^{rms}_{plane} in a plane of a particle passing trough a x thickness of material can written as [132]:

$$\theta_0 = \frac{13.6MeV}{\beta cp} z \sqrt{\frac{l}{X_0}} \left[1 + 0.038 \ln\left(\frac{l}{X_0}\right)\right] \tag{6.1}$$

where p, βc and z are the momentum, velocity and charge number of the incident particle and $\frac{l}{X_0}$ is the thickness of the scattering medium in radiation lenghts. For thin layers and light materials the expression for θ_0 can be improved [133], but it is not the case in this work. The value of θ_0 coming from Eq. 6.1 is accurate to 11% or better for a $10^-3 < \frac{l}{X_0} < 100$.
The angular distribution, when projected to planes, is given by:

$$\frac{\mathrm{d}N}{\mathrm{d}\theta_{plane}} \frac{1}{\sqrt{2\pi}\theta_0} e^{-\frac{\theta^2_{plane}}{2\theta_0^2}} \tag{6.2}$$

The mean deviations projected to the axis perpendicular to the original direction of motion of the particle are:

$$x^{rms}_{plane}, y^{rms}_{plane} = \frac{1}{\sqrt{3}} l\theta_0 \tag{6.3}$$

Deflections into the two ortogonal planes are independent.
The absorber has to stop as much as possible hadrons coming from all interaction in the target region. Anyhow muons passing through it have multiple scattering. Therefore, looking at Eq. 6.1, one understands that the material used to build the absorber must have the bigger ratio of number of interaction lenghs and number of radiation lengths, in order to maximise its stopping power while avoiding to introduce too much scattering on muons. In Tab. 6.1 values of radiation lenght X_0 and interaction lenght λ_I are reported for different materials. To get an idea of quantities let compute the value of θ_0 for 1 meter of iron, aluminum oxide and berillium for a particle with 10 GeV/c of momentum, $c = 1$ and $\beta \approx 1$. One gets respectively 11.8 mrad, 5.6 mrad and 4 mrad. The ratios between the number of pion interaction lenght and radiation lenght are 0.086, 0.216 and 0.59. The expectation that lighter materials give smaller deflection is correct, but they are too light, and a large thickness is needed to get enough stopping power. Then the ideal choice is a big thickness of a light material to attenuate particle flux and not deteriorate muon tracks. Hovewer space is limited in

Medium	ρ g/cm^3	Nuclear λ_I (cm)	Pion λ_I (cm)	X_0 (cm)
Be	1.848	42.10	59.47	35.28
C graphite	2.21	38.83	53.30	19.32
Fe	7.87	16.77	20.42	1.757
W	19.3	9.946	11.33	0.3504
Concrete	2.30	42.39	55.92	11.55
Al_2O_3	3.97	24.79	32.57	7.038

Table 6.1: Values of radiation lenght X_0, nuclear and pion interaction lenght λ_I for different materials.

the COMPASS geometry and only 2 m are available for an absorber. Light material are not dense enough to stop hadrons and they cannot be chosen as absorber. Some compounds can solve the problem with an higher density but keeping deflection small. Therefore it has been decided to choice aluminum oxide (Al_2O_3) as the material to build the absorber. However it has been found that a fully Al_2O_3 absorber it is not enough to stop hadrons and also stainless steel will be used for the absorber.

6.3 Resolutions of di-muon mass and vertexes

In the previous section, some aspect of the impact of the absorber were analysed, in particular the effect of the multiple scattering of particles passing trough it. A direct consequence is the decrease of the resolution of the coordinates of the vertex where the Drell-Yan interaction occours. The capability of assigning events inside one cell or the other one is closely related to the way asymmetries are extracted, since the analysis directly uses the number of events assigned to each cells. Clearly, if events are wrongly assigned to cells, any asymmetry can potentially be diluted.
Another requirement which needs to be satisfied is a good resolution on the di-muon mass. As already stated, the mass distribution is characterised by the presence of the resonance peak J/ψ and Υ. A good resolution on the invariant mass is needed to safely identify Drell-Yan events by selecting the region between the resonances, without rejecting to many events.
Therefore the resolutions of di-muon mass and primary vertex coordinates are of particular interest in this work.

6.4 Description of the geometry

The setup of the apparatus has been adapted to the mentioned upgrades using the 2007 geometry as a starting point. The study of this configuration has been pursued and it has evolved step by step, approaching an optimal configuration with a feed-back mechanism. The main modification are listed:

- to make room for the absorber, the whole platform which houses the polarised target and cryogenics stuff, as well as beam trackers, is moved up of 260 cm upstream along the beam line
- as a consequence of the previous point, the geometric acceptance of the apparatus decreased and the momentum of beam was increased from 160 GeV/c to 190 GeV/c to recover part of it, exploiting the Lorentz boost
- two hodoscope planes are placed in the Large Angle Spectrometer, the first one soon after SM1, the second one before SM2

6.4.1 Target: position and shape

The target is the COMPASS polarised target, which has the possibility of polarise in opposite directions contiguos cells containing the material. It appear from Monte Carlo that cells must be spaced by at least 20 cm (see Sec. 6.6.4). A three cells configuration would waste too much space and therefore a two cells solution is needed. Two 55 cm long cylindrical cells, spaced by 20 cm, fit the 130 cm long target container. The diameter of cells is 4 cm. The target center is locate at z = -260 cm. At this distance, the spectrometer has a geometric acceptance of about 110 mrad. The material is NH_3 and it counts for $\sim$0.9 interaction lenghts.

6.4.2 Geometry of the hadron absorber

A candidate for the absorber is described. The absorber has to cover the full acceptance of the spectrometer, which is equal to 110 mrad in case of target centered at z = -260 cm. Its transverse dimensions depend on the relative position with respect to the target. It is made of seven contigous layers placed along the beam line, each one 30 cm thick. The first five layers are made of aluminum oxide (Al_2O_3) and their transverse area is 100 $\times$ 100 cm^2; the last two are made of stainless steel with a transvere area of 110 $\times$ 110 cm^2. All the layers are centered on the beam line and the first block is 115 cm away from the nearest edge of the target. In the inner part of the absorber a beam dump is positioned to stop the beam which does not interact with the target. The dump is made of six tungsten cylinders with radius of 2.16 cm, 2.64 cm, 3.12 cm, 3.60 cm, 4.08 cm and 4.56 cm. The first layer of the absorber has a cylindrical hole with 2.16 cm radius; the other six layers have the tungsten cylinder placed in order of increasing radius as they are farther from the target. In such a way the beam dump covers a conical solid angle of 16 mrad and it provides 13.2 interaction lenghts to stop essencially all the beam particles. Fig. 6.1 shows the structure of the absorber. The empty volume in the first layer makes the beam start interacting with the dump inside the absorber, thus helping in containing the radiation dose. No other radioprotetion aspects will be discuss in this work, but it is reasonable to think that a real implementation of the hadron absorber will consider a design where the absorber is surrounded by additional shielding concrete blocks. Another advantage of having more space between target cells and dump is that it makes it easy to separate events from target and absorber during analysis and it relaxes requirements on the pitch of the trigger hodoscope planes. The absorber, in total, counts 7.5 interaction lenghts and 55.5 radiation lenghts. The number of interaction lenghts satisfy the request of reducing the hadron flux to 0.5%.

6.4.3 Geometry of trigger hodoscopes

A dedicated trigger for the Drell-Yan program is needed since no muon trigger exist in the Large Angle Spectrometer. The development of the hodoscope planes, used to implement this trigger, has been done satisfying the request of the transversity physics program, to which the 2010 COMPASS run is dedicated, and of the DVCS program, which is another physics program proposed for COMPASS.

The hodoscope planes are intended to be placed in the first part of the spectrometer, soon after the first magnet (H1H at z = 570 cm) and between the Muon Filter 1 and the second magnet (H2H at z = 1570 cm), thus having the biggest available lever arm to point tracks back to the target region. The two hodoscope planes share the same geometry, but the first one is smaller, scaled to allow target pointing. H1H is 230 cm long, 192 cm high

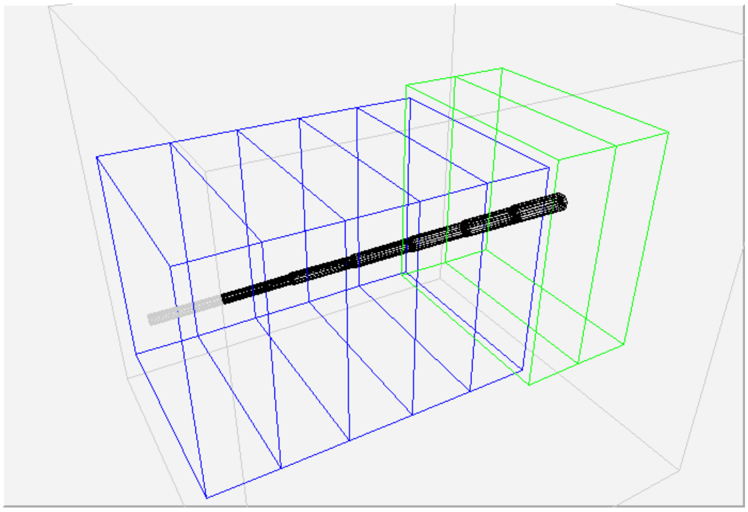

Figure 6.1: Assonometric view of the absorber. The aluminum oxide layers are blue, the steel ones are green. The absorber has a beam dump in the inner part (black). The first layer has a cylindrical hole (grey) to lower the radiation dose and keep it inside the absorber.

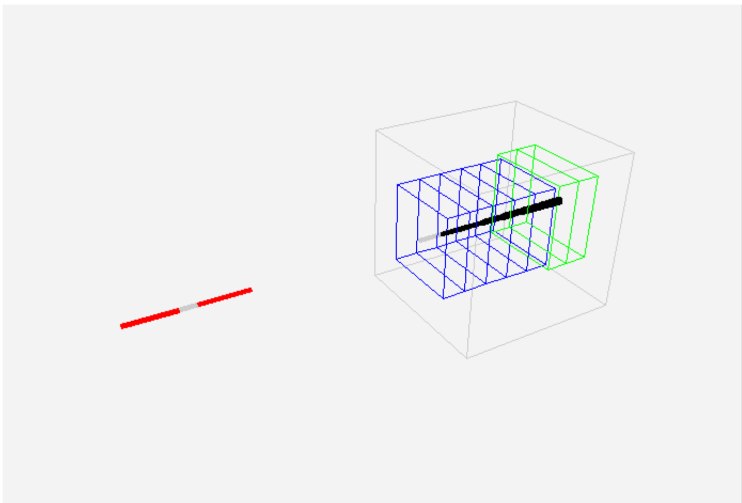

Figure 6.2: Assonometric view of the absorber and the two cells of the target (red).

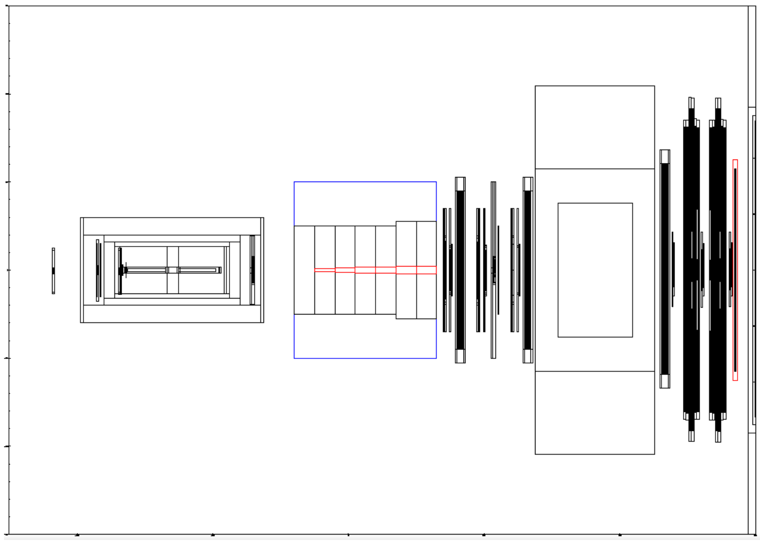

Figure 6.3: Side projection of the LAS spectrometer. This image, taken with the COMPASS Monte Carlo program, shows the position of the target platform (left) and the absorber (center). Tracking detectors around the SM1 magnet are clearly visible (right).

and 2 cm thick. H1H, has 32 horizontal strips: 26 full length strips, below and above the hole, and 6 shorter strips with central light air guide, to fit the hole width. Each strip is 6.2 cm wide, but with a overlap of 0.2 cm with the adjacent ones (0.1 per each side). The full height of H1H (192 cm) comes out exactly multiplying the total number of strips along the vertical direction, i.e 32, times their pitch, which is 6 cm. To allow the overlapping of adjacent slabs, they have been displaced along the z axis by $\pm$ 0.5 cm with respect to the central plane. Each strip is read-out from the two sides. The size of the central hole is 68 cm $\times$ 36 cm.
H2H is located very close to the MuonWall1 and it has a similar size. It is 500 cm $\times$ 419 cm, with a central hole of 150 cm $\times$ 78.5 cm. Each slab is 13 cm wide with an overlap of 0.5 cm. The longest slabs (5 m long) are divided in two to have good time resolution. Each slab is read from the two sides.

6.5 Generators of Drell-Yan events

Two event generators were used to produce Drell-Yan events: the PYTHIA generator [134], version 6.4.18, and the DY_AB generator [135], version 5.4. PYTHIA is a generator often used in Monte Carlo simulations; it has been

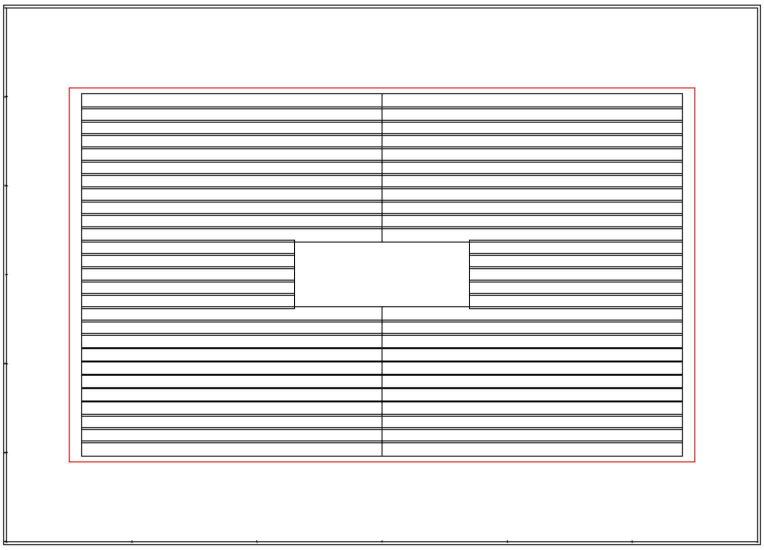

Figure 6.4: Front view of the two hodoscope planes. H1H and H2H share the same geometry, but H1H is smaller to allow track point to target region.

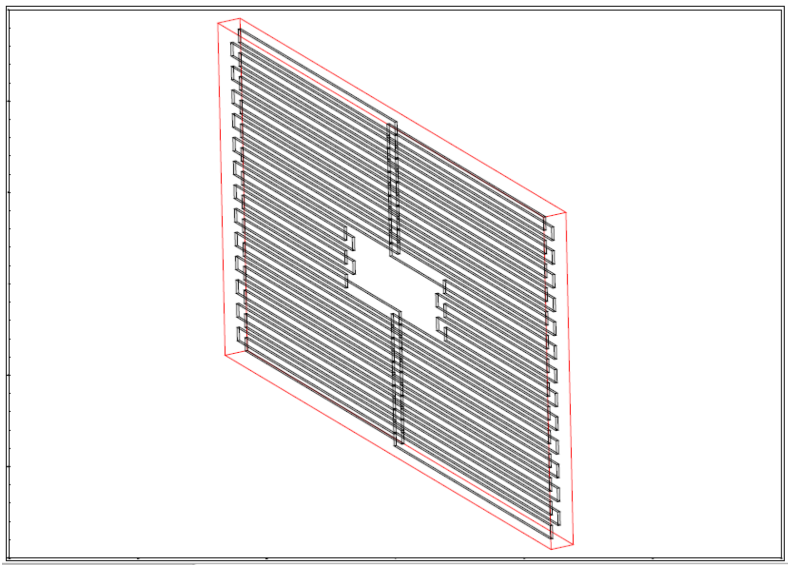

Figure 6.5: View of the second hodoscope plane (H2H) placed at z = 1570 cm. All long slabs are divided in two pieces and all scintillators are read from both sides to get a reasonable time resolution.

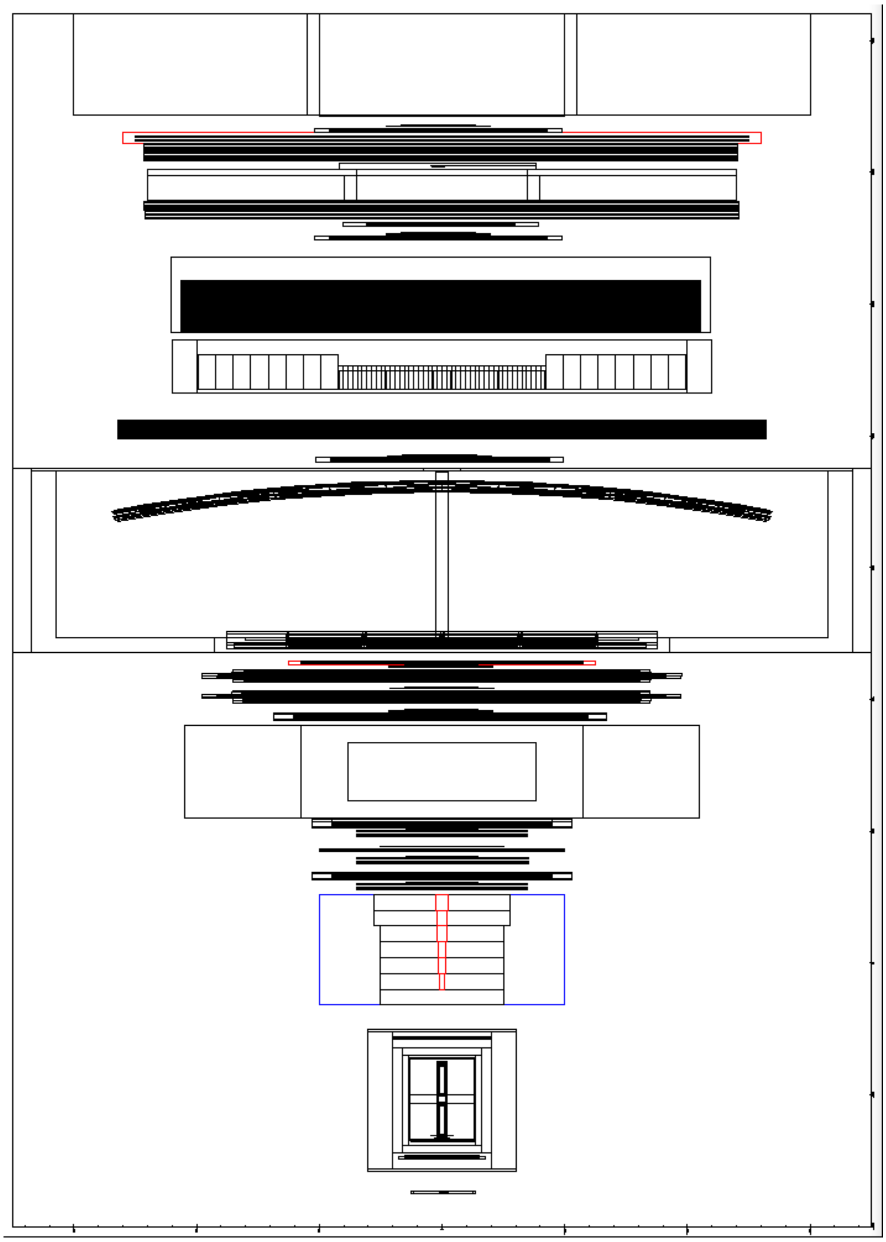

Figure 6.6: Projection of the LAS. The target and the absorber are visible in the left side. H1H and H2H are drawn in red.

	H1H	H2H
x size (cm)	230	500
y size (cm)	192	419
z position (cm)	570	1570
slab width (cm)	6.2	13.5
slap overlap (cm)	0.2	0.4
hole x size (cm)	68	150
hole y size (cm)	36	78.5

Table 6.2: Summary of H1H and H2H properties.

configured to generate Drell-Yan process in the reaction $\pi^- p \rightarrow \mu^+\mu^- + X$. PYTHIA is not capable to generate event with polarised hadron beam or target, even if a modified version of the generator was developed to include longitudinally polarised proton beams [136]. PYTHIA Drell-Yan cross section does not apply any K-factor correction. PDF set in PYTHIA has been provided by LHAPDF library [137], version 5.4.1.
DY_AB generator has been considered since it is capable to generate unpolarised, single polarised and double polarised Drell-Yan events. The DY_AB generator has parametrisation for Boer-Mulders and Sivers functions, which can be tuned by the user. Also parameters of unpolarised quark distribution can be adjusted. This generator has K-factor correction and it is capable to reproduce cross sections measured in past Drell-Yan experiments [135].
The main Drell-Yan sample count more than 500000 events, which is a number greater by a factor of 2 than the statistic the Drell-Yan program foresee to collect. Larger sample may be used resulting in smaller statistical errors. The mass range is between 4 and 9 GeV/c^2. A lower cut on the transverse momentum q_T of di-muons is set at 0.1 GeV/c. No other cuts were applied.

6.5.1 Pythia settings

The Drell-Yan event generation of $\pi^- p \rightarrow \mu^+\mu^- + X$ with PYTHIA has been done with the following settings:

- MSEL = 11 : it selects $\gamma \rightarrow 2$ processes
- MSTP(32) = 4 : it imposes the definition of $Q^2 \equiv M^2$
- MSTP(43) = 3 : full interference between γ and Z (not relevant at

this energy)

- CKIN(1) = 4. (GeV/c^2) : lower mass limit
- CKIN(2) = 9. (GeV/c^2) : higher mass limit
- CKIN(5) = 0.1 (GeV/c) : lower q_T limit
- CKIN(6) = 10. (GeV/c) : upper q_T limit (such a high value does not affect the transverse momentum distribution)
- PARP(111) = 0.1 (GeV/c^2): lower cut for available mass for remnant part of the reaction which does not include Drell-Yan; any reasonable value below 0.3 GeV/c^2 does not put any upper cut in x_F distribution

A special parametrisation is used for the description of the parton intrinsic transvere momentum:

- MSTP(91) = 1 : Gaussian primordial k_T distribution of hadrons, parametrised as $e^{\frac{k_T^2}{\sigma^2}} k_T$
- PARP(91) = 0.8 (GeV/c) : width of the Gaussian primordial k_T distribution of hadrons, PARP(91)^2 $= < k_T^2 >$
- PARP(93) = 3. (GeV/c) : upper cut-off for k_T distribution of hadrons

The value of the width of the Gaussian is larger than what can be explained in perturbative terms and it also appears to be larger than values usually put in parameterisation. A larger value compensate for imperfections in the perturbative or modeling description and it has a energy and a process dependance. Thus it has to vary for an optimal description. The values are set according to the prescription coming from NA50 comparisons of simulation with Pythia and data [138].
The generation of event used the so-called “new model”. The PDFs used for the proton and pion are GRV98-LO

6.5.2 DY_AB settings

The DY_AB generator was not extensively used and no polarisation features were turned on. The configuration used was the one as close as possible to the Pythia case. The reaction $\pi^- p \to \mu^+ \mu^- + X$ was properly configured:

- int N_repeat = 1
- bool Collins_Soper_21 = 1
- int Spin_Verse = 1
- Dilepton Lepton_Pair = muon
- Particle Projectile = pion_minus
- double Esse_GeV_Quadri = 357 (GeV^2/c^4)
- double Massa_Lower_Cut_Off = 4.00 (GeV/c^2)
- double Massa_Upper_Cut_Off = 9.00 (GeV/c^2)
- double PT_Lower_Cut_Off = 0.1 (GeV/c)
- double PT_Upper_Cut_Off = 10. (GeV/c)
- double XF_Cutoff = 0.98
- double Theta_Lower_Cut_Off = 0
- double Theta_Upper_Cut_Off = M_PI

The DY_AB generator has some options to set the target material and the dilution factor. These configurations can be adjusted using the ratios of atomic mass and atomic number of the materials and the composition of unpolarised, single and double polarised Drell-Yan events, with the options:

- double ZA_No_Pol
- double ZA_Single_Pol
- double ZA_Double_Pol
- int N_Events_No_Pol
- int N_Events_Single_Pol
- int N_Events_Double_Pol

6.5.3 Comparisons of Pythia and DY_AB

A comparison of the two generator is presented here. Distributions of some quantities are compared. In Figs. 6.7, 6.8, 6.9, 6.10, 6.11, 6.12, 6.13 distributions coming from PYTHIA are blue, while the ones from DY_AB are blue. The distributions are normalised so the missing k-factor in the PYTHIA generator will not strogly affect the comparison.

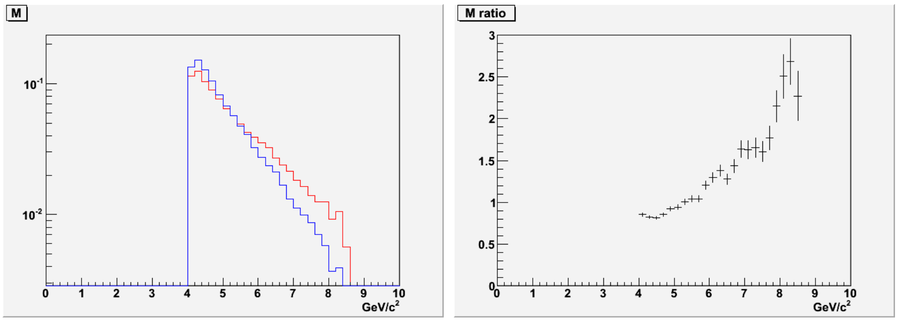

(a) (b)

Figure 6.7: (a) Di-muon invariant mass distribution, PYTHIA red, DY_AB blue. (b) Ratio of the distributions of panel (a).

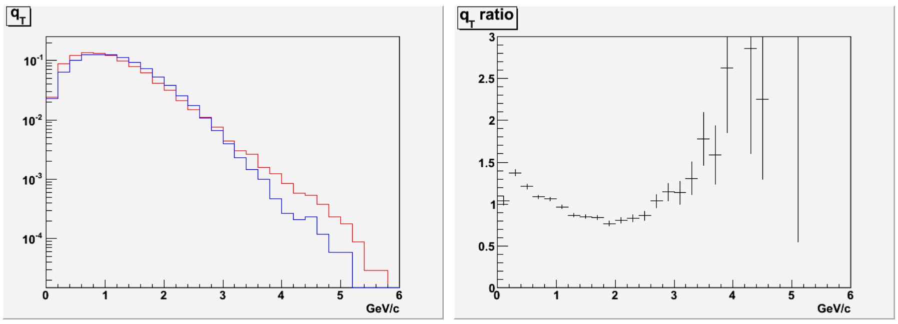

(a) (b)

Figure 6.8: (a) Di-muon transverse momentum distribution, PYTHIA red, DY_AB blue. (b) Ratio of the distributions of panel (a).

The two generators do not perfectly agree, but they do not show big differences. This is not a surprise, because they implement different models. This is understandable, for example, for the shapes of the parton distributions, which are different because of different parameterisations. What is noticeable is that DY_AB produces distributions of transverse momentum

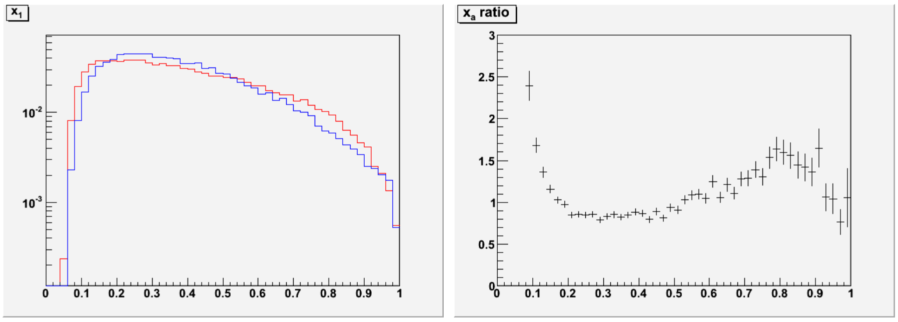

(a) (b)

Figure 6.9: (a) x_a variable distribution, PYTHIA red, DY_AB blue. (b) Ratio of the distributions of panel (a).

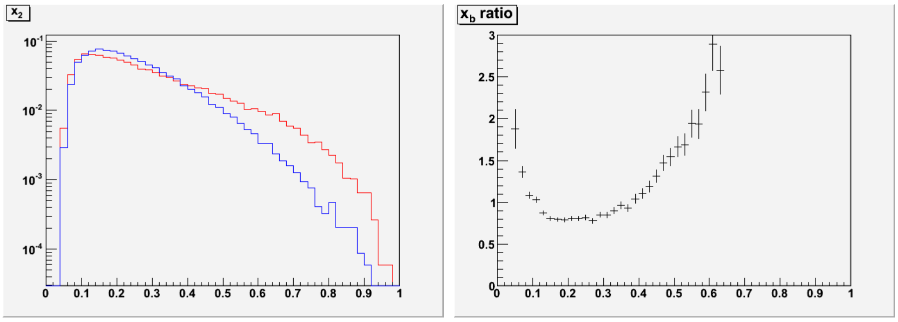

(a) (b)

Figure 6.10: (a) x_b variable distribution, PYTHIA red, DY_AB blue. (b) Ratio of the distributions of panel (a).

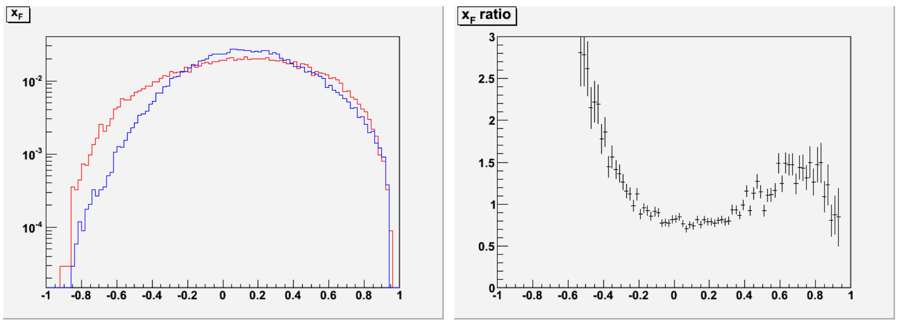

(a) (b)

Figure 6.11: (a) x_F distribution, PYTHIA red, DY_AB blue. (b) Ratio of the distributions of panel (a).

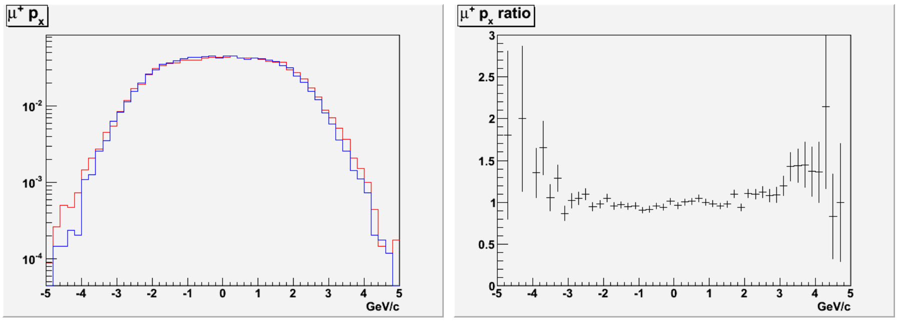

(a) (b)

Figure 6.12: (a) x component of positive muon momentum distribution, PYTHIA red, DY_AB blue. (b) Ratio of the distributions of panel (a).

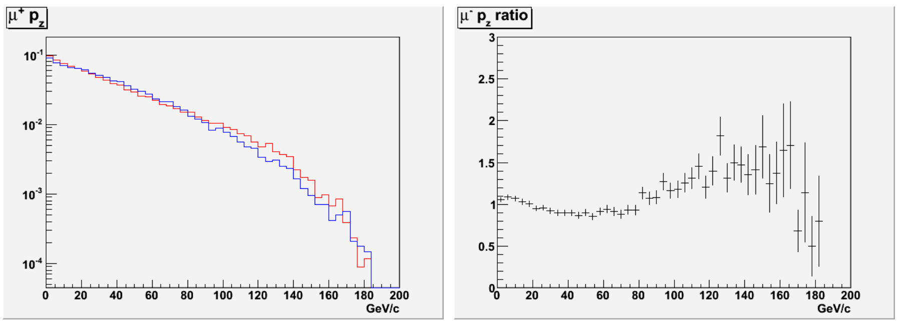

(a) (b)

Figure 6.13: (a) longitudinal component of positive muon momentum distribution, PYTHIA red, DY_AB blue. (b) Ratio of the distributions of panel (a).

of di-muons and muons larger than Pythia ones. This finds a motivation in the better tuning of DY_AB generator to experiment data, which show this behaviour in those distributions.
If not specified, Pythia has been used to generate Drell-Yan events.

6.6 Monte Carlo simulations

The commonly used simulation tool in the COMPASS framework is the code COMGeant. The COMGeant program is an interface to GEANT 3.21 simulation package. It has been used for the WA89 experiment and it has been upgraded to be used for the COMPASS experiment. The geometry data should be stored in external data files in the FFREAD format. COMGeant contains calls to certain kinematic packages like JETSET (PYTHIA and FRITIOF) and it is also possible to use external generator. All types of plane detectors are properly treated: MWPC, DC, silicon micro-strips, scintillator hodoscopes. The hit information can be written out and are used by the reconstrution program, CORAL, which offers the same framework for reconstruction of real data and Monte Carlo data.
The implementation of the description of the geometry has been done modifying FFRED files, according to the user manual.

6.6.1 Generated Drell-Yan sample

A large sample of 500000 events has been produced in the di-muon invariant mass range 4-9 GeV/c^2. The motivation of this choice have already been explained in previous sections. Plots for the invariant mass (Fig. 6.14), transverse (Fig. 6.15) and total momentum (Fig. 6.16) of virtual photon, x_a (Fig. 6.17), x_b (Fig. 6.18) and x_F (Fig. 6.19) variables are shown. Also the x_b versus x_a plot (Fig. 6.20) is shown.

6.6.2 Spreading of DY events along the target

The output of both Pythia and DY_AB generator is composed by the energies and momenta of the two leptons. This is the natural output of DY_AB generator; the output of Pythia has been adapted to filter all informations but the muons parameters. This has been considered enough since the Drell-Yan process is the objective of this investigation.

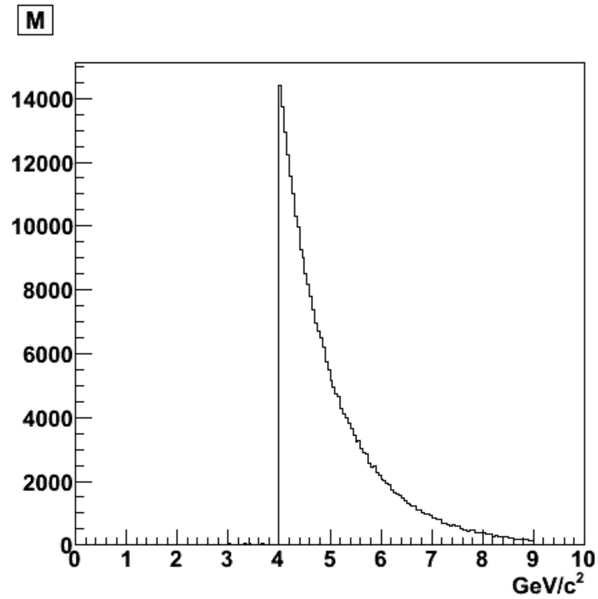

Figure 6.14: Virtual photon invariant mass distribution generated with PYTHIA.

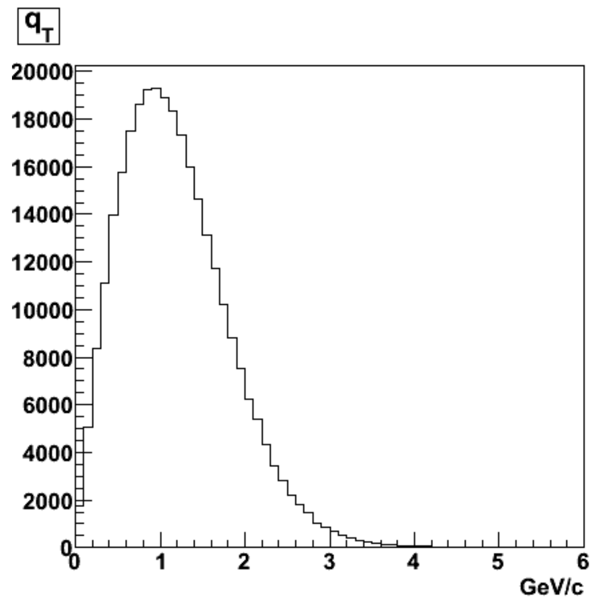

Figure 6.15: Virtual photon transverse momentum distribution generated with PYTHIA.

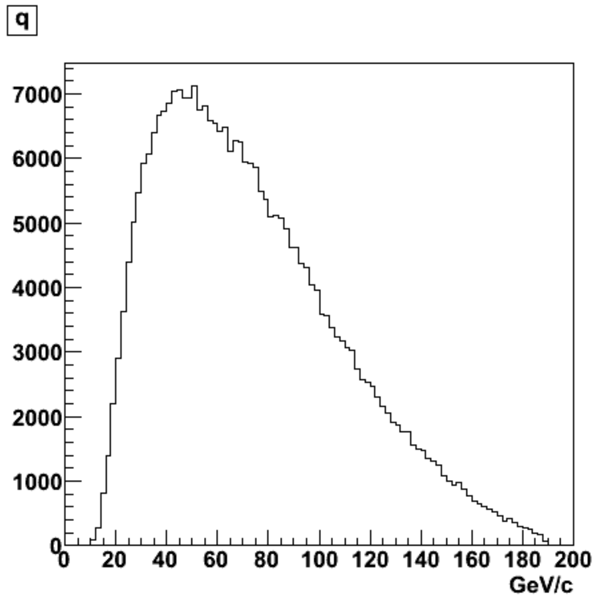

Figure 6.16: Virtual photon momentum distribution generated with Pythia.

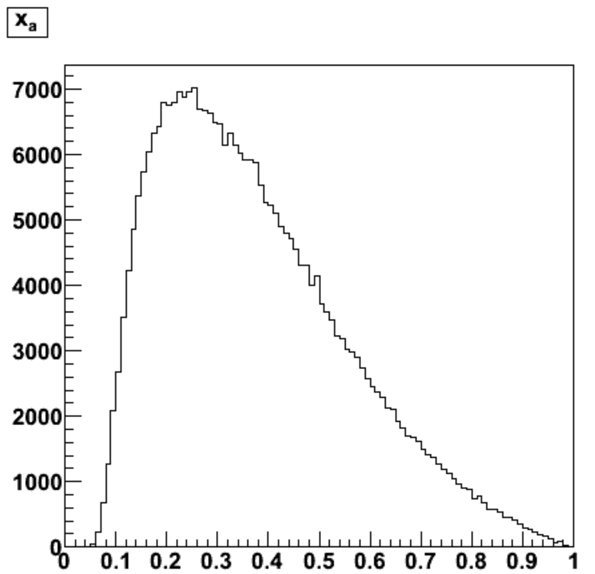

Figure 6.17: x_a variable distribution generated with Pythia.

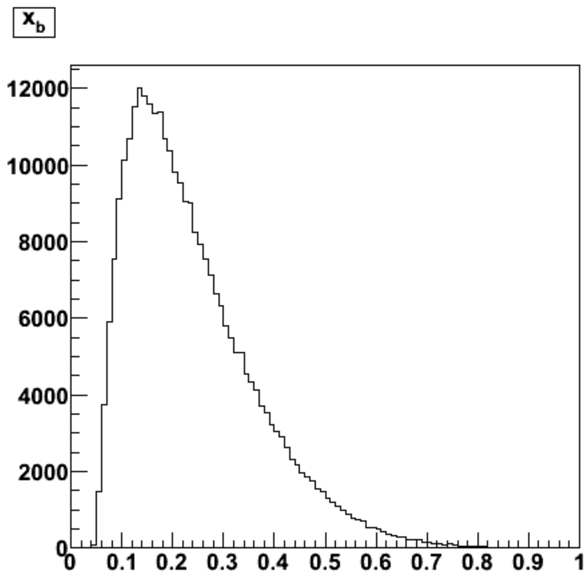

Figure 6.18: x_b variable distribution generated with Pythia.

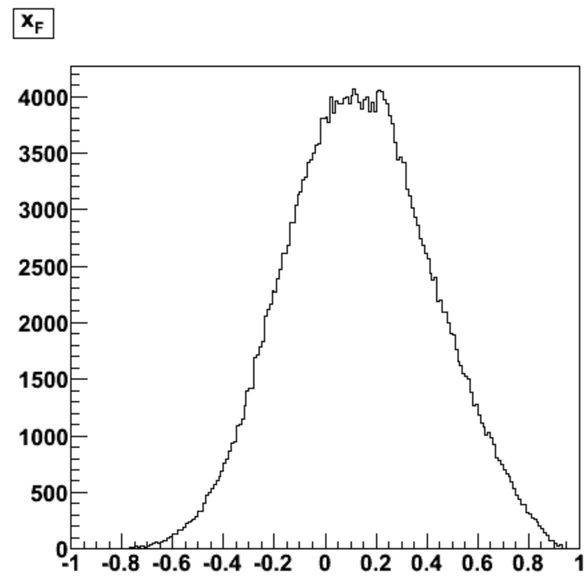

Figure 6.19: x_F variable distribution generated with Pythia.

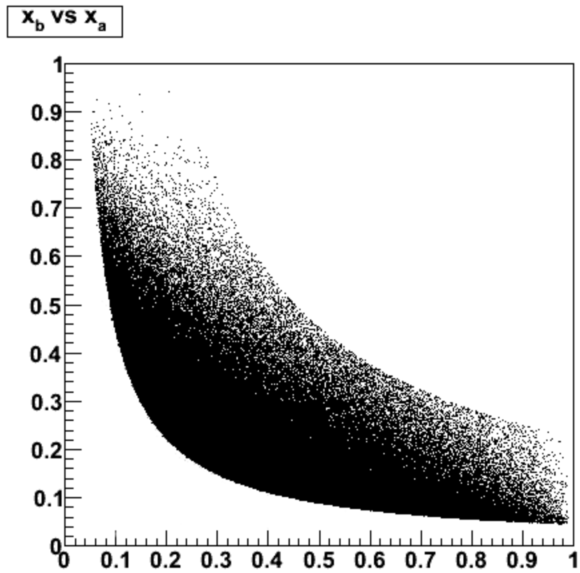

Figure 6.20: x_b versus x_a scatter plot generated with PYTHIA.

Events are then spreaded inside the target volume using a program which creates primary vertexes. The transverse coordinates of vertexes follow a Gaussian distribution with a sigma of 0.3 cm. This value has been chosen accordlying to the foreseen beam spot size. The distribution along the beam line follows a decreasing exponential, whose exponent is the effective interaction lenght of the target material. Figs. 6.21(a) and 6.21(b) show the distribution of vertex z coordinate and the scatter plot of vertex x and y coordinates.

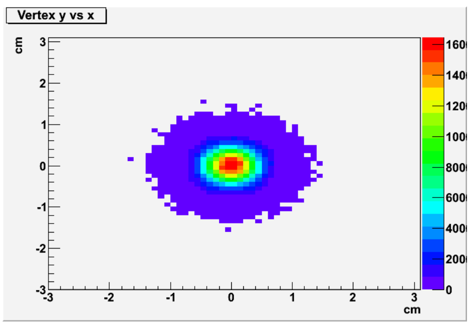

(a)

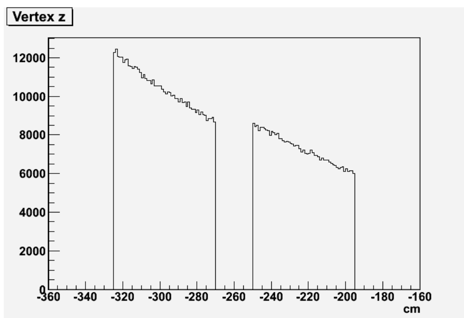

(b)

Figure 6.21: (a) Trasverse profile of vertex coordinates. (b) Distributions of vertex z coordinate.

6.6.3 Acceptances

Acceptance of the spectrometer to Drell-Yan events is defined by the capability to track muons. Two different criteria exist to accept tracks in the spectrometer since the apparatus is divided in LAS and SAS. A muon is tracked in the LAS if its track has at least 5 hits in the second half of MuonWall1 (MA02); if it has at least 7 hits in MuonWall2 (MB) or 5 in MWPC-B (PB), then it can be tracked in the SAS. Obviously both muons must be tracked in order to have the complete Drell-Yan event in acceptance. Rules are applied in the following order:

- check if both muons are accepted in LAS;
- check if both muons are accepted in SAS;
- check if positive muon is tracked in LAS, the negative in SAS;
- same as previous rule, with exchanged electric charge.

When rules are applied, the resulting fractions of Drell-Yan events are:

- 34.5% of all Drell-Yan events are in the spectrometer acceptance;

The accepted events are distributed:

- 66% both muons are tracked in LAS;
- ∼33% events have one muon in LAS, the other in SAS;
- ∼1% both muons are tracked in SAS;

From distributions of significant quantities obtained from events in acceptance the acceptance plots have been obtained dividing these distributions by the ones of all generated events bin by bin. Figs. 6.22, 6.23, 6.24, 6.25, 6.26, 6.27. shows acceptances. Acceptances are flat for di-muons invariant mass and di-muon transverse momentum; this is expected as there exist no particular reason in the spectrometer to prevent different mass region not to be in the acceptance, at this beam energy. Acceptance is also flat for the the transverse momentum of the virtual photon.
Acceptances are not flat for the partons variables x_a and x_b, and also for x_F. The acceptance for this quantities is limited by the nature of the experimental apparatus, a fixed target experiment. In such kind of spectrometer the

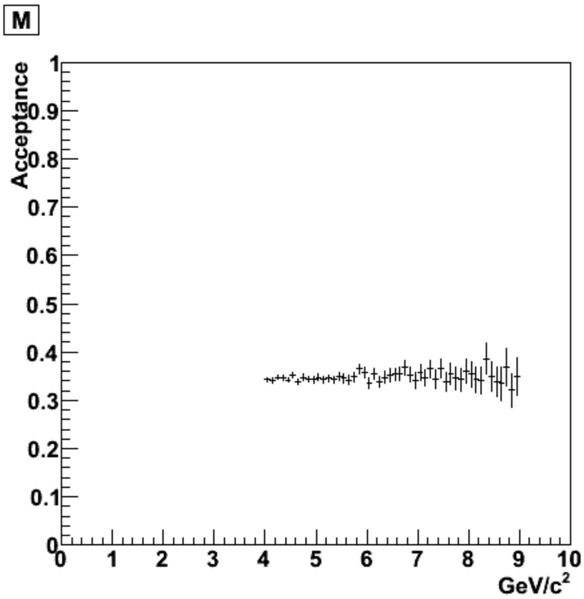

Figure 6.22: Di-muon invariant mass acceptance: ratio of distributions from accepted and generated events.

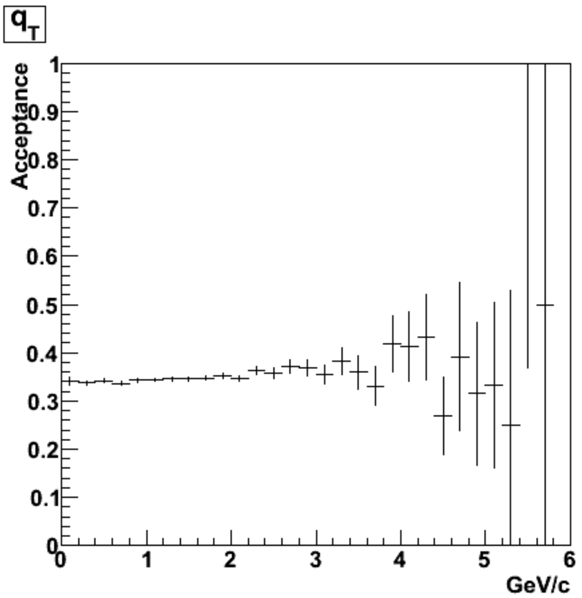

Figure 6.23: Di-muon trasverse momentum acceptance: ratio of distributions from accepted and generated events.

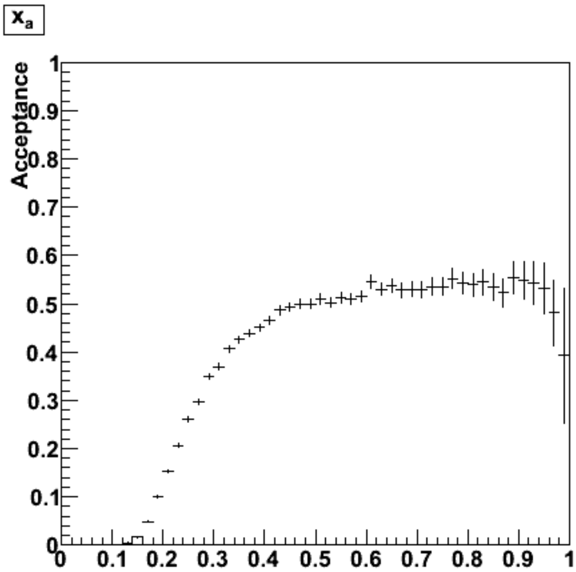

Figure 6.24: x_a acceptance: ratio of distributions from accepted and generated events.

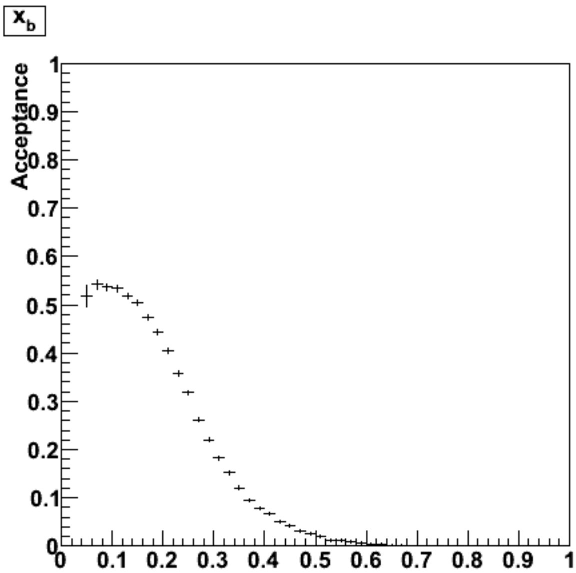

Figure 6.25: x_b acceptance: ratio of distributions from accepted and generated events.

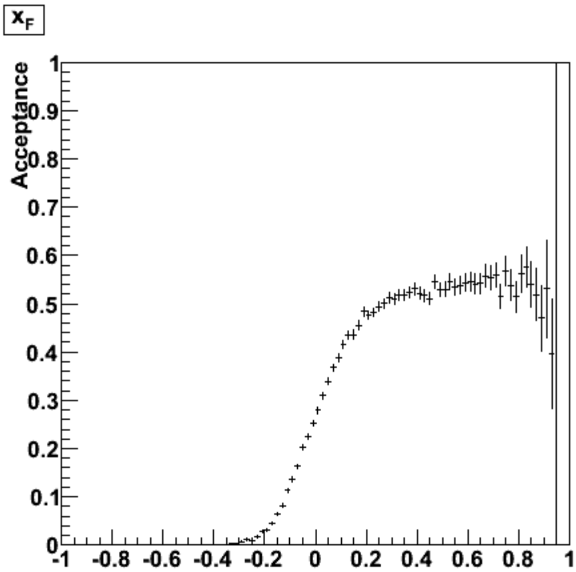

Figure 6.26: x_F acceptance: ratio of distributions from accepted and generated events.

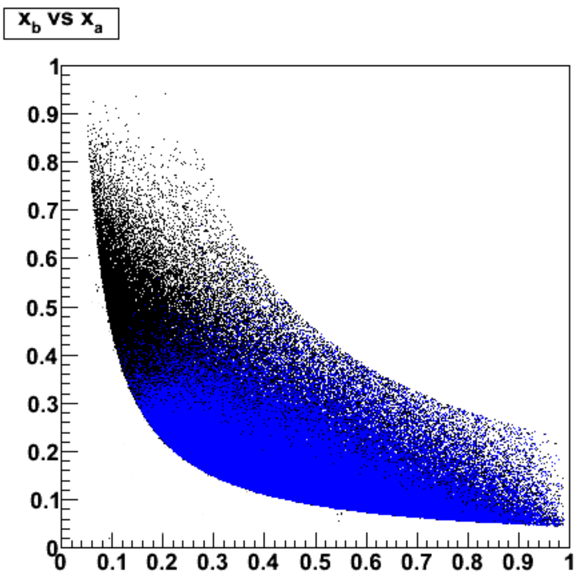

Figure 6.27: x_b vs x_a region in acceptance (blue) superimposed over all generated region (black).

acceptance is limited by geometric factor to essentianlly positive values of x_F. However one thing of great importance is that the acceptances for the x_b variable, which refers to the proton, has still its maximum in the quark valence region, between 0.01 and 0.3.
The acceptance for two other variables should be checked: the acceptance for the ϕ_{CS} and θ_{CS} angles. Some comments can be made for the ac-

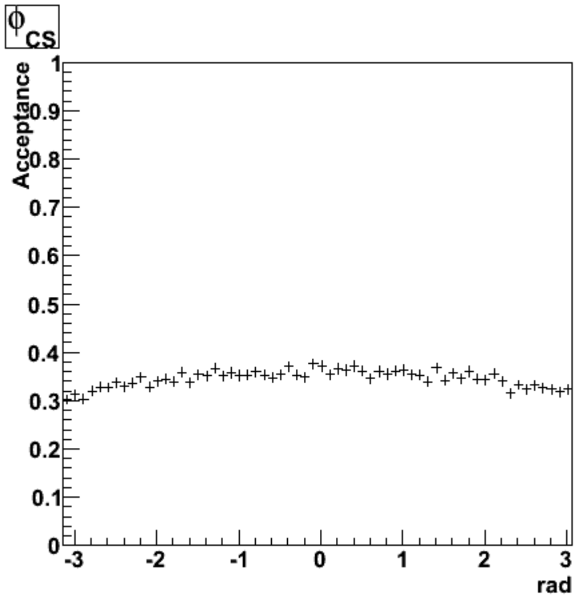

Figure 6.28: ϕ_{CS} acceptance: ratio of distributions from accepted and generated events.

ceptance of the two lepton angles ϕ_{CS} and θ_{CS}. The acceptance for θ_{CS} differs significantly from being flat. This is also not a suprise because of the limited acceptance for polar angle of the spectrometer. The acceptance for ϕ_{CS} is not flat and this has to be treated carefully since it can introduce fake asymmetries which can disturb real ones depending on ϕ_{CS}. Such a study is foreseen in near future.

6.6.4 Estimation of resolutions

In Sec. 6.3 the topic of the resolutions on reconstructed vertex coordinates and virtual photon invariant mass has been introduced. A study about it has been performed. First a hypotetical experiment has been simulated, leaving the spectrometer geometry with no modification as it was in 2007.

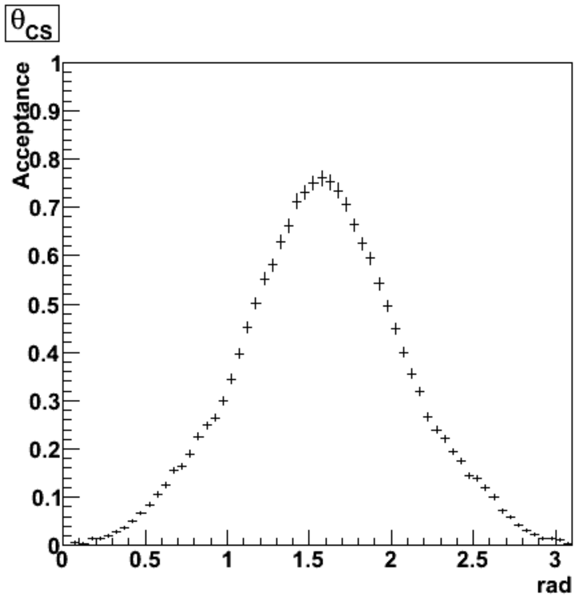

Figure 6.29: θ_{CS} acceptance: ratio of distributions from accepted and generated events.

Then Drell-Yan events were spreaded along the three cells target and resolutions were studied.
The study has been performed for the new geometry but in two steps: in the first, the target has been moved upstream of 260 cm; then the absorber was inserted in geometry. Resolutions have been studied in both setup, aiming to disantangle the effects of movement of the target and of the absorber. In fact it is reasonable to believe that the reconstruction efficiency may deteriorate by a change in the geometry and by the presence of absorber. Recostruction code has been developed in the hypothesis that particles may be tracked in open space free of materials and with detectors positioned close to the interaction region.
The estimation of resolution has been perfomed by comparing the simulated values with the reconstructed one. The difference (delta) has been plotted and fitted with a Gaussian curve. In first approximation the Gaussian models the distribution of the reconstruction error. Its mean values is expected to be centered at zero. Hovewer one must notice that the width of the Gaussian carries an information of all the possible motivations of error without the possibility to distinguish between real and reconstruction contributions.

2007 geometry case

The hypotetical case of a 2007 spectrometer has been investigated without going deeply in details. The distributions of differences ($\equiv \Delta$) between true and reconstructed value of invariant mass of di-muon, vertex x position and vertex z position are respectively shown in Figs. 6.30, 6.31 and 6.32. These plots have been obtained for all the reconstructed Drell-Yan events, with no consideration for the vertex position. It can be appreciated that the fit on the mass distribution difference gives a width of about 15 MeV. This value is of the same size of the bin size used for a J/ψ analysis on muon data (see Fig. 6.33). The width for vertex x and z positions are respectively less than 0.1 cm and ∼0.5 cm. As expected, a separation of 5 cm is enough to separate cells and correctly assign vertexes to one or another cells.

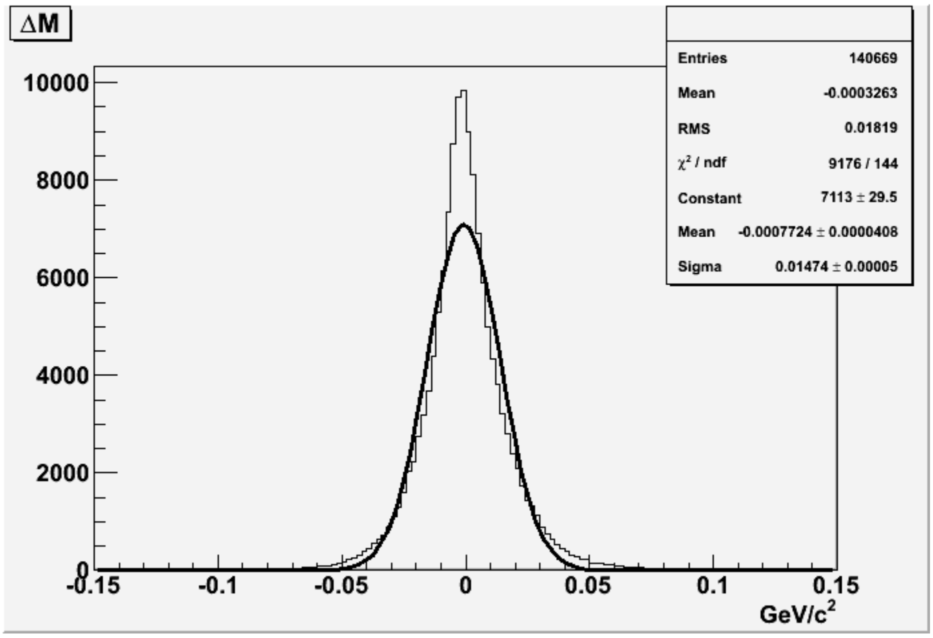

Figure 6.30: Distribution of differences between true and reconstructed mass for 2007 geometry case.

Shifted target case

For the case of the geometries in which the movement of the target platform has been implemented (260 cm upstream), a different, more sistematic approach has been taken. Samples of Drell-Yan events at a fixed di-muon

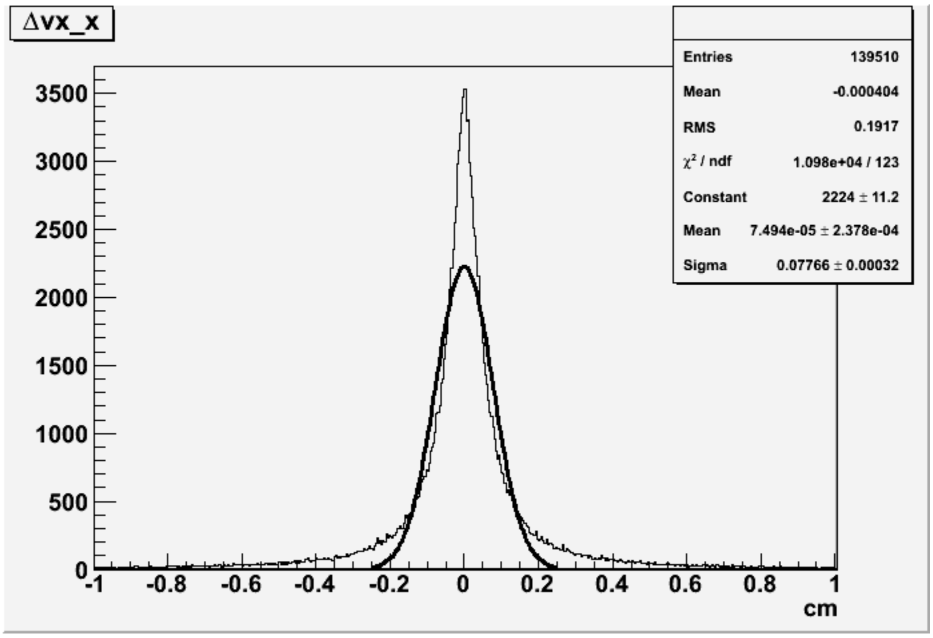

Figure 6.31: Distribution of differences between true and reconstructed vertex x position for 2007 geometry case.

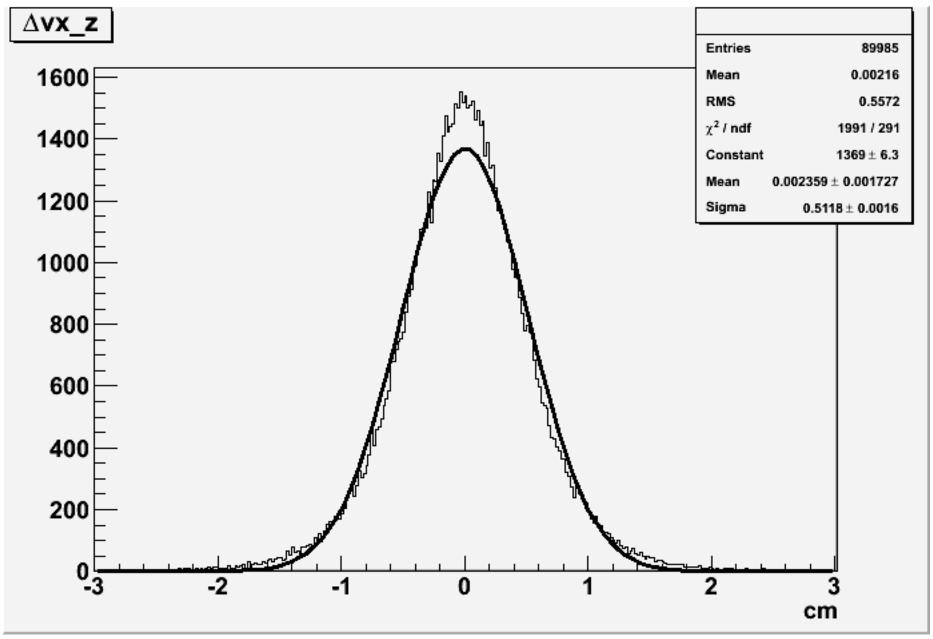

Figure 6.32: Distribution of differences between true and reconstructed vertex z position for 2007 geometry case.

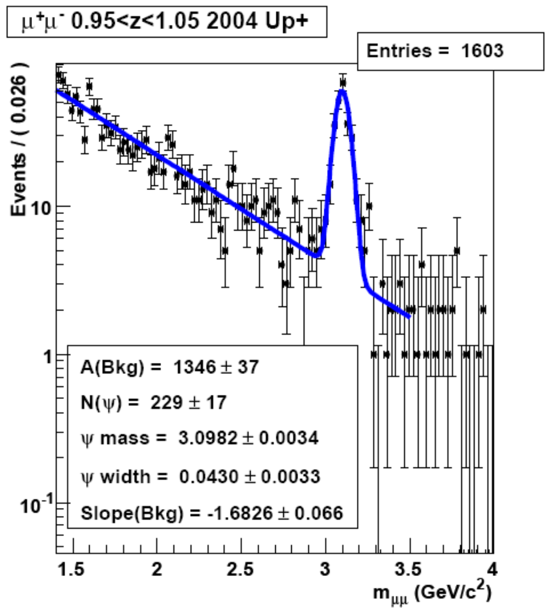

Figure 6.33: J/ψ peak from muon data. The binning of the mass distribution is of the same size of the resolution estimated.

invariant mass have been generated, from 3 to 9 GeV/c^2, with 1 GeV/c^2 step. Each sample has been distributed at a specific vertex z coordinates, while x and y coordinates have been left Gaussian distributed. Vertexes were distributed at beginning and end of each cells, at z = -325 cm, -270 cm, -250 cm and -195 cm. The reason of this approach is to study rigorously the dependance of resolution on mass and vertex on the z position at different masses; for vertex coordinates x and y, this exercise has not been done because of the cylindrical symmetry, therefore no dependence has been postulated.

The study has been performed for both geometries, with and without absorber.

In Figs. 6.34, 6.35, 6.36, 6.37 and in Tabs. 6.3, 6.4, 6.5, 6.6 results are summarised for the geometry without absorber: the tables report per each mass at each vertex z coordinate the differences of reconstructed and true mass, x and z coordinates, and the ratio RC of reconstructed events and events in acceptance. The delta quantities for y coordinate are very similar to the ones for x and they are omitted.

The action of moving the target implies tangible effects on the re-

Mass (GeV/c^2)	ΔM (MeV/c^2)	ΔV_x (cm)	ΔV_z (cm)	% RC
3	71.4 ± 0.6	0.0160 ± 0.0002	0.52 ± 0.01	34.8%
4	84 ± 1	0.0180 ± 0.0002	0.52 ± 0.01	40.6%
5	107 ± 1	0.0192 ± 0.0003	0.49 ± 0.01	48.4%
6	136 ± 1	0.0212 ± 0.0003	0.478 ± 0.004	55.6%
7	176 ± 1	0.0232 ± 0.0003	0.456 ± 0.004	61.1%
8	218 ± 2	0.0248 ± 0.0003	0.443 ± 0.004	67.0%
9	274 ± 2	0.0280 ± 0.0003	0.428 ± 0.003	70.7%

Table 6.3: Deltas from geometry without absorber, all vertexes at z = -195 cm.

Mass (GeV/c^2)	ΔM (MeV/c^2)	ΔV_x (cm)	ΔV_z (cm)	% RC
3	194 ± 1	0.0343 ± 0.0005	0.92 ± 0.01	33.8%
4	199 ± 1	0.0353 ± 0.0005	0.78 ± 0.01	40.8%
5	217 ± 1	0.0357 ± 0.0005	0.692 ± 0.006	48.0%
6	243 ± 2	0.0369 ± 0.0004	0.622 ± 0.005	53.9%
7	276 ± 2	0.0386 ± 0.0004	0.580 ± 0.005	60.0%
8	317 ± 2	0.0394 ± 0.0004	0.543 ± 0.004	65.5%
9	368 ± 3	0.0411 ± 0.0004	0.528 ± 0.004	69.1%

Table 6.4: Deltas from geometry without absorber, all vertexes at z = -250 cm.

Mass (GeV/c^2)	ΔM (MeV/c^2)	ΔV_x (cm)	ΔV_z (cm)	% RC
3	244 ± 2	0.0379 ± 0.0006	1.05 ± 0.01	34.2%
4	246 ± 2	0.0381 ± 0.0005	0.840 ± 0.009	40.5%
5	263 ± 2	0.0388 ± 0.0005	0.719 ± 0.007	46.9%
6	289 ± 2	0.0398 ± 0.0004	0.649 ± 0.006	53.8%
7	319 ± 2	0.0406 ± 0.0004	0.600 ± 0.005	58.8%
8	366 ± 3	0.0409 ± 0.0004	0.561 ± 0.005	64.2%
9	410 ± 3	0.0423 ± 0.0004	0.547 ± 0.004	67.4%

Table 6.5: Deltas from geometry without absorber, all vertexes at z = -270 cm.

Mass (GeV/c^2)	ΔM (MeV/c^2)	ΔV_x (cm)	ΔV_z (cm)	% RC
3	388 ± 3	0.0476 ± 0.0007	1.23 ± 0.02	32.5%
4	381 ± 3	0.0441 ± 0.0005	0.98 ± 0.01	38.1%
5	390 ± 3	0.0429 ± 0.0005	0.824 ± 0.008	44.8%
6	408 ± 3	0.0442 ± 0.0005	0.747 ± 0.007	49.5%
7	443 ± 3	0.0438 ± 0.0004	0.671 ± 0.006	53.9%
8	481 ± 3	0.0445 ± 0.0004	0.624 ± 0.005	57.4%
9	524 ± 4	0.0457 ± 0.0004	0.608 ± 0.005	59.9%

Table 6.6: Deltas from geometry without absorber, all vertexes at z = -325 cm.

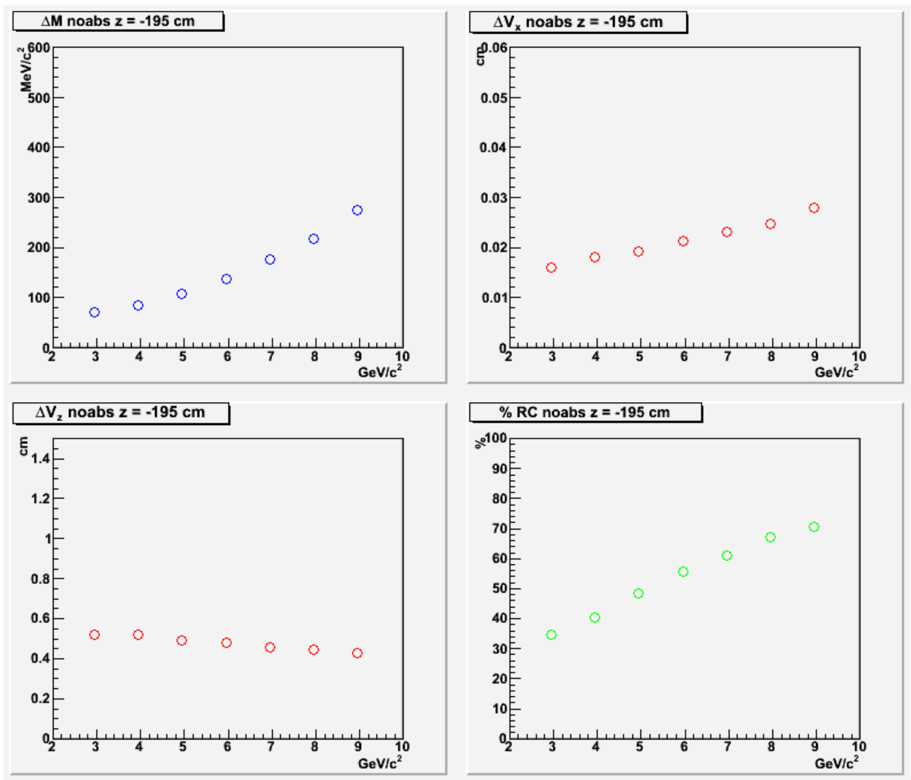

Figure 6.34: Deltas from geometry without absorber, all vertexes at z = -195 cm.

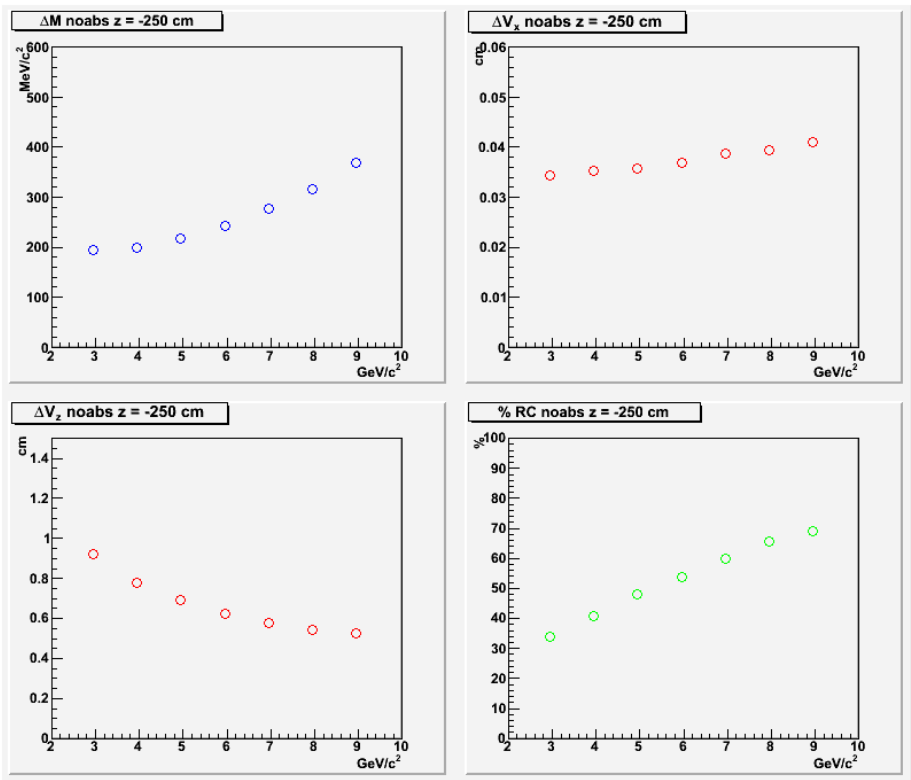

Figure 6.35: Deltas from geometry without absorber, all vertexes at z = -250 cm.

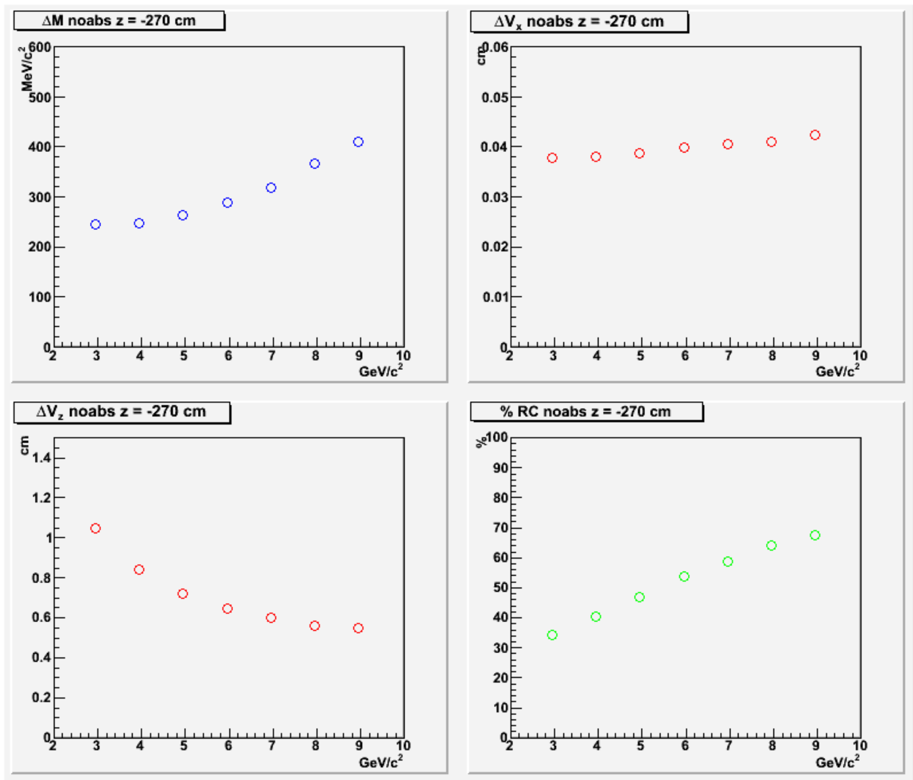

Figure 6.36: Deltas from geometry without absorber, all vertexes at z = -270 cm.

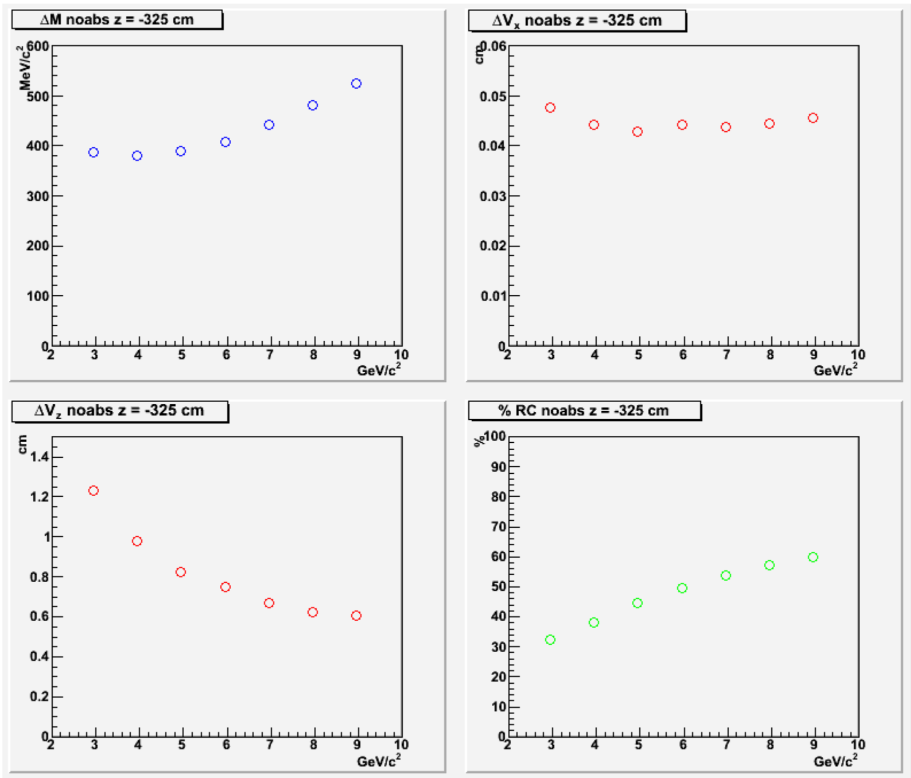

Figure 6.37: Deltas from geometry without absorber, all vertexes at z = -325 cm.

constructed quantities. The distributions of differences of all quantities get wider. It is reasonable to hypothesize that the reconstruction algorithms suffer this movement, due to a large distance that extrapolation code have to cover to find the vertex from which muon tracks arise. A reconstruction effect on mass, ranging from 2% to 7%, is visible, with the higher impact at most negative values of z and lower masses. It has to be stressed, however, that the vertex resolution ΔV_z is still good enough to separate events produced in different target cells.

Complete geometry case

Figs. 6.38, 6.39, 6.40, 6.41 and Tabs. 6.7, 6.8, 6.9, 6.10 summarize the results for the geometry with absorber, similarly to previous tables.

Mass (GeV/c^2)	ΔM (MeV/c^2)	ΔV_x (cm)	ΔV_z (cm)	% RC
3	257 ± 4	0.68 ± 0.02	13.4 ± 0.6	22.1%
4	260 ± 3	0.50 ± 0.01	11.4 ± 0.3	27.8%
5	274 ± 3	0.430 ± 0.009	9.3 ± 0.1	34.5%
6	297 ± 3	0.404 ± 0.007	7.81 ± 0.09	41.4%
7	317 ± 3	0.362 ± 0.006	7.01 ± 0.07	48.3%
8	345 ± 3	0.336 ± 0.005	6.17 ± 0.05	55.3%
9	383 ± 3	0.307 ± 0.004	5.52 ± 0.04	60.0%

Table 6.7: Deltas from geometry with absorber, all vertexes at z = -195 cm.

Mass (GeV/c^2)	ΔM (MeV/c^2)	ΔV_x (cm)	ΔV_z (cm)	% RC
3	294 ± 4	0.68 ± 0.02	18 ± 1	18.6%
4	293 ± 4	0.63 ± 0.01	14.8 ± 0.6	23.7%
5	311 ± 3	0.552 ± 0.008	12.0 ± 0.3	30.0%
6	329 ± 3	0.532 ± 0.007	9.8 ± 0.2	36.0%
7	349 ± 3	0.494 ± 0.005	8.2 ± 0.1	43.7%
8	383 ± 3	0.477 ± 0.005	7.44 ± 0.07	49.9%
9	418 ± 3	0.448 ± 0.004	6.73 ± 0.06	55.3%

Table 6.8: Deltas from geometry with absorber, all vertexes at z = -250 cm.

With the insertion of the absorber, effects on the reconstructed quantities

Mass (GeV/c^2)	ΔM (MeV/c^2)	ΔV_x (cm)	ΔV_z (cm)	% RC
3	319 $\pm$ 4	0.73 $\pm$ 0.02	19 $\pm$ 2	17.4%
4	337 $\pm$ 4	0.67 $\pm$ 0.01	13.7 $\pm$ 0.5	22.5%
5	344 $\pm$ 4	0.600 $\pm$ 0.009	11.7 $\pm$ 0.3	28.7%
6	363 $\pm$ 3	0.559 $\pm$ 0.007	10.1 $\pm$ 0.2	34.8%
7	392 $\pm$ 3	0.531 $\pm$ 0.006	8.8 $\pm$ 0.1	42.0%
8	415 $\pm$ 3	0.497 $\pm$ 0.005	7.78 $\pm$ 0.08	48.1%
9	458 $\pm$ 4	0.476 $\pm$ 0.004	7.04 $\pm$ 0.06	53.4%

Table 6.9: Deltas from geometry with absorber, all vertexes at z = -270 cm.

Mass (GeV/c^2)	ΔM (MeV/c^2)	ΔV_x (cm)	ΔV_z (cm)	% RC
3	403 $\pm$ 6	0.82 $\pm$ 0.02	16 $\pm$ 2	15.2%
4	442 $\pm$ 5	0.76 $\pm$ 0.01	14.9 $\pm$ 0.9	20.1%
5	442 $\pm$ 4	0.69 $\pm$ 0.01	11.7 $\pm$ 0.4	25.9%
6	464 $\pm$ 4	0.622 $\pm$ 0.008	10.5 $\pm$ 0.2	30.4%
7	490 $\pm$ 4	0.596 $\pm$ 0.007	9.2 $\pm$ 0.1	35.8%
8	521 $\pm$ 4	0.575 $\pm$ 0.006	8.6 $\pm$ 0.1	41.2%
9	562 $\pm$ 5	0.539 $\pm$ 0.005	7.44 $\pm$ 0.08	45.1%

Table 6.10: Deltas from geometry with absorber, all vertexes at z = -325 cm.

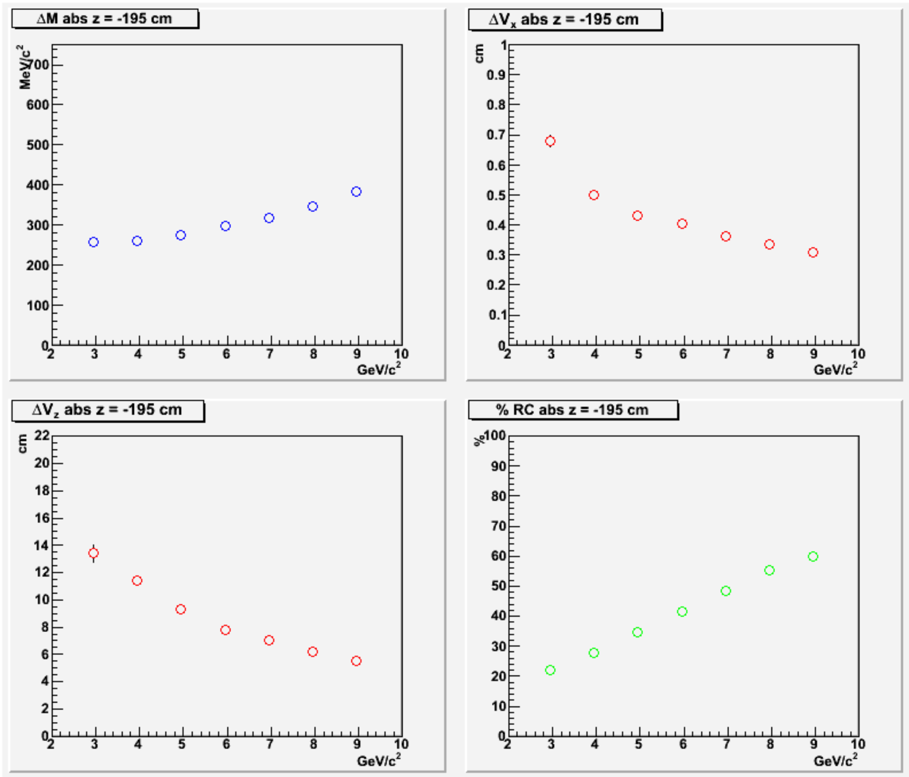

Figure 6.38: Deltas from geometry with absorber, all vertexes at z = -195 cm.

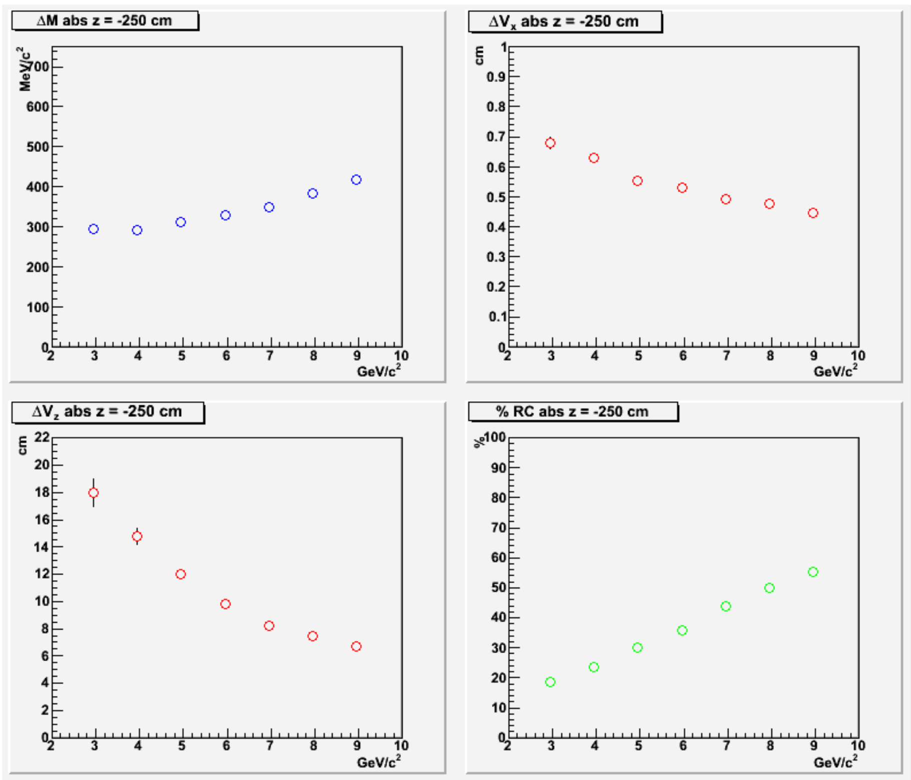

Figure 6.39: Deltas from geometry with absorber, all vertexes at z = -250 cm.

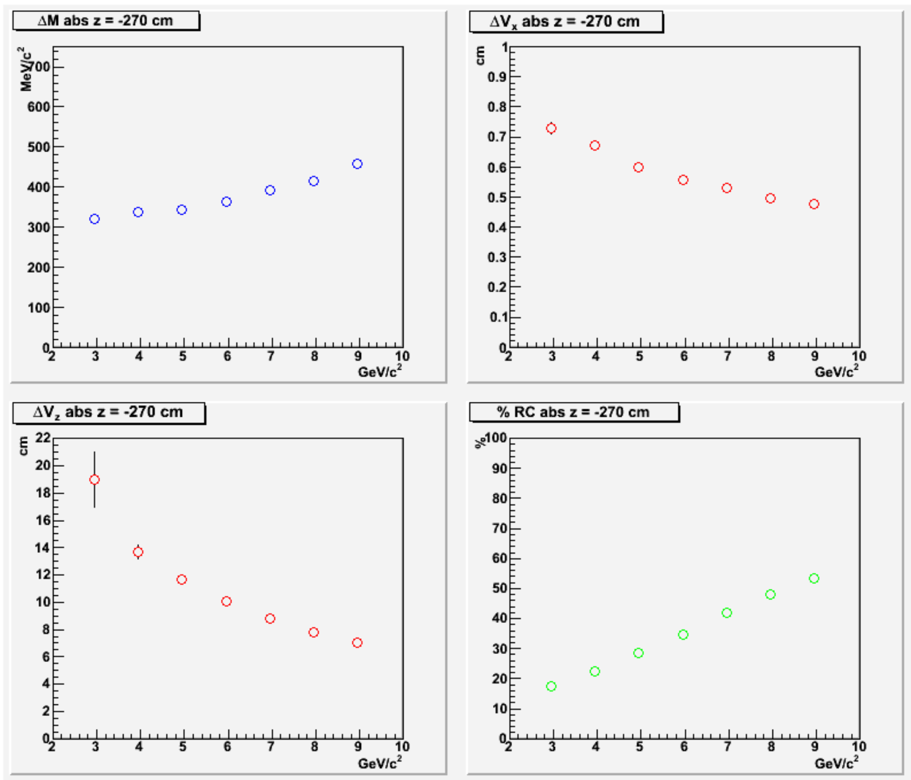

Figure 6.40: Deltas from geometry with absorber, all vertexes at z = -270 cm.

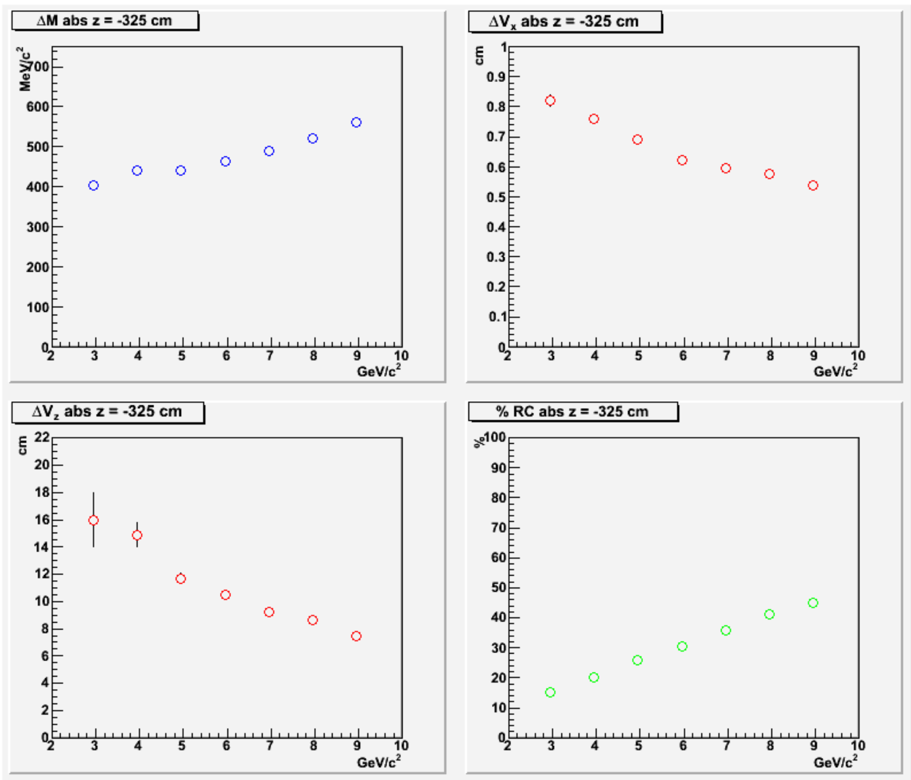

Figure 6.41: Deltas from geometry with absorber, all vertexes at z = -325 cm.

are more visibile and the distributions of differences of all quantities get even more wider; that is not surprising and the reconstruction differences on mass range from 5% to 10% with, also in this case, the higher impact at most negative values of z and lower masses.

Some considerations

Lower masses events suffer some reconstruction problem, that manifests in the percentage of reconstructed events which is lower for those masses. This is a direct consequence of dependence on mass: in fact events with higher masses have a better reconstruction as the absorber has less impact on tracking. This explains the fact that the ratio of reconstructed events is higher for 7-9 GeV/c^2 masses.
The absorber is a big problem for reconstruction algorithms which are forced to extrapolate track back for several meters through a dense medium till primary vertexes. The efficiency drops but one problem is the computation of the energy loss in the medium which depends on the energy of particles which cross it. A map for energy loss is provided to the analysis program but no momentum correction is implemented, thus muons with 2 GeV/c or 90 GeV/c momentum receive the same energy correction which translate easily in few hundreds of MeV of error in the reconstructed di-muon mass. In future modification in the code are certainly needed. Other approach may be to relax quality parameters for tracks and vertexes finding, but a limit must be put to ensure a minimal quality of reconstruction.
Another problem is the poor resolution with which the z coordinate of the interaction vertex can be reconstructed, which is not sufficient, in the present simulation, to separate events in different cells. This problem can only be solved by improvements in the tracking, by placing more tracking detectors in between the target and the absorber.

6.6.5 Trigger hodoscopes

In this chapter it has been said that hodoscopes have been introduced in the simulation. This argument will not be covered extensively but some plots can be shown and some comments can be added.
The sizes of hodoscopes have been computed from the x and y distributions

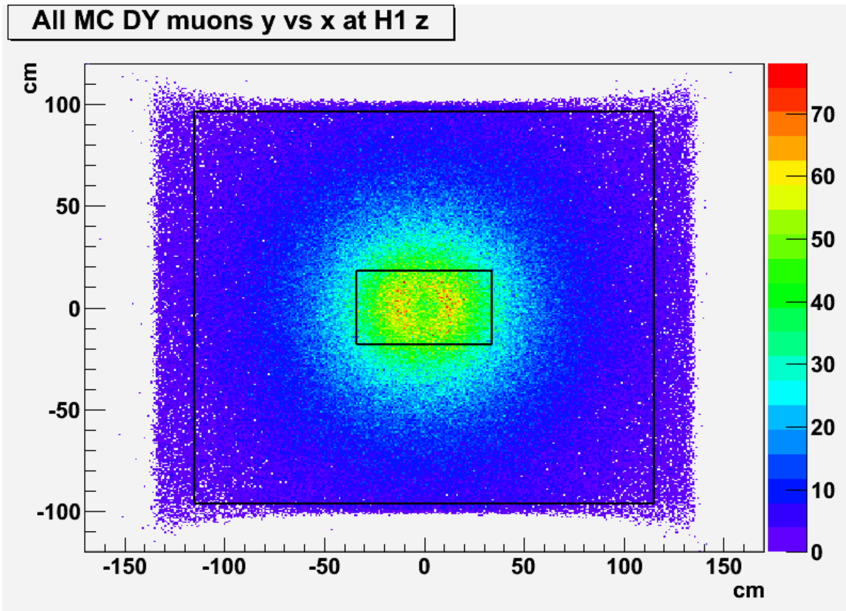

Figure 6.42: Distribution x-y of muon tracks from Monte Carlo Drell-Yan events at $z = 570$ cm, where H1H will be placed. H1H has been drawn in black.

of muons from Drell-Yan events at the z wanted for the detector. Slab sizes have been computed almost geometrically to allow pointing of tracks to target region. Fig. 6.42 and 6.43 show the profile x-y of muon tracks belonging to simulated Drell-Yan events at the z position foreseen for the two hodoscopes. The hodoscope planes covers well the area crossed by tracks. In Fig. 6.43 a red square shows the projection of the beam dump at the z coordinate of the hodoscope. Both profiles are characterised by a depletion of tracks in the center due to the presence of the beam dump which removes, not only beam particles, but also muons.

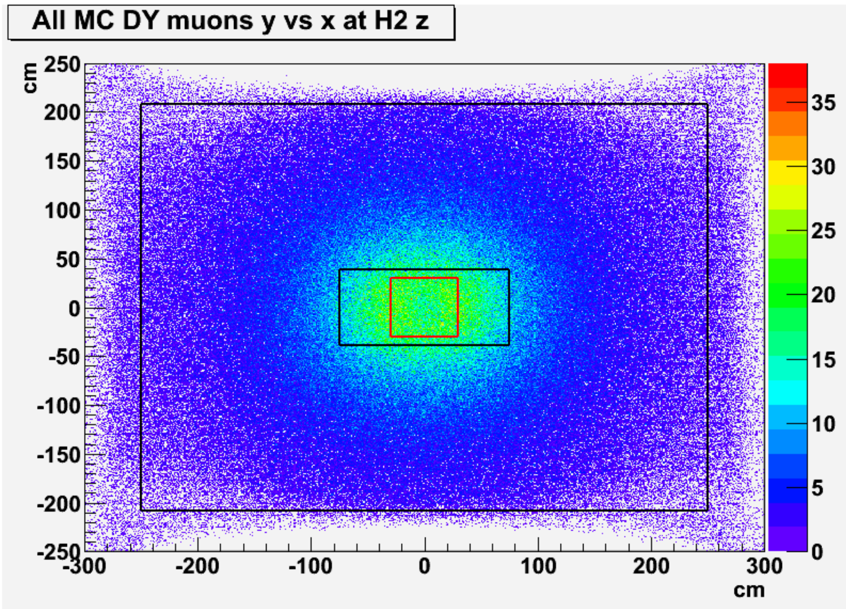

Figure 6.43: Distribution x-y of muon tracks from Monte Carlo Drell-Yan events at $z = 1570$ cm, where H2H will be placed. H2H has been drawn in black. The red square inside the hole of H2H indicates the projection of the beam dump at the same z of the hodoscope.

Chapter 7

2009 beam test

In this chapter a short presentation of the 2009 Drell-Yan test is reported. The test was performed at the end of the run of year 2009, using the last five days from the 18^{th} November. During this time the spectrometer has been significantly modified to get as close as possible to the configuration which is thought to be used for a possible Drell-Yan program at COMPASS. In the following the experimental apparatus is described and some preliminary result are reported, focusing on those topic which received contribution from the Monte Carlo study presented in the previous chapter and from my personal contribution.

7.1 The 2009 Drell-Yan beam test

The 2009 test had the aim to see how the spectrometer behaves when most of the modification, needed for Drell-Yan measurement, are introduced. Therefore five days were requested and obtained to perform the test: two days were scheduled for all installations and the remaining were used for data taking.

7.1.1 Experimental conditions

During the installation the area around the target was heavily modified. The situation of the spectrometer was the one used for the hadron run, with the spectrometer arranged for 190 GeV/c beam, with the hydrogen target and Recoil Proton Detector (RPD) in the target area.

The installation can be summarised in the following main steps:

- removal of RPD and hydrogen target
- insertion of an absorber downstream the target
- insertion of concrete shielding structure around absorber
- insertion of a dummy target

The beam was set up for 190 GeV/c negative pion and its transverse dimension were reduced as much as possible in order to have the smallest spot on the dump and have the hadronic shower fully contained in it.

The absorber

The absorber was designed to be as close as possible to the one simulated. Materials were stainless steel and concrete, which substituted aluminum oxide, and tungsten for the beam dump. Al_2O_3 was not easily available, mainly because of its excessive cost, and thus concrete was used. The absorber was 2 m long. 10 equal layers were placed along the beam line and centered on it. The first 5 layers were made of concrete, while the remainig meter was done of stainless steel. Transverse area was 80 $\times$ 80 cm^2. A beam dump was present in the inner part of the layers, along the beam line; it was made up by cylinders of tungsten, with radius ranging from 1 cm to 2.5 cm that were inserted from the third layer to the last one. The first two layers had empty (air) cylindrical volumes to reduce back scattering from the beam. Fig. 7.1 shows absorber in the setup. The survey, done after the insertion of this huge object, reported a shift of only -3 cm along z axis of all installation with respect to positions in Fig. 7.1. Transverse positioning was accurate to within $\pm$1 mm.

The target

The target was made of two polyethylene cylinders, with radius of 2.5 cm and lenght of 40 cm. They were separeted by 20 cm and the downstream edge of the second cylinder was 20 cm far from the absorber.

7.1.2 The trigger

The trigger was arranged in a way similar to the trigger used in 2007 (see Subsec. 5.1.2). The only significant difference was suggested by the Monte

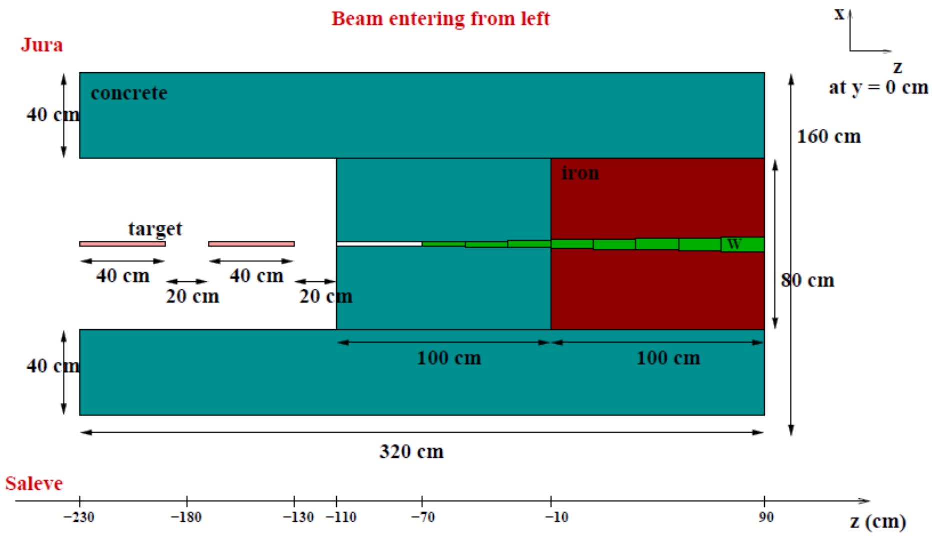

Figure 7.1: Schematic view of the absorber and target installed for the 2009 test. They are all surrounded by a concrete cover for radioprotection purposes. Surveyors reported that all actual positions were shifted of -3 cm along z axis.

Carlo studies here presented: half of the acceptance for pairs of muons lays in the Large Angle Spectrometer, for which no trigger was available. Following a suggestion of mine, the COMPASS trigger group succeded in the implementation of a di-muon trigger in the LAS. The di-muon trigger in the LAS was realised by requiring two clusters from at least 0.7 MIPS in the HCAL1 and vetoing all over the hadron calorimeter for signals greater than 2.5 MIPS. The trigger was then composed by (only relevant trigger bits):

1. beam trigger
    - Bit 7
2. one muon in the SAS
    - Bit 0: ladder trigger (LT)
    - Bit 8: middle trigger (MT)
    - Bit 10: outer trigger (OT)
3. one muon in the SAS and one muon in LAS
    - Bit 1: MT and H_μ

- Bit 2: LT and H_μ
- Bit 3: OT and H_μ

4. two muons in LAS

- Bit 4

7.2 First result

7.2.1 Beam profile

The beam was monitored online during the first phases of data acquisition. Its dimensions were measured looking at the profiles of SciFi and Silicons detectors of the beam telescope. On x and y projection of SciFi 1, Silicon 1 and Silicon 3 a Gaussian fit has been done, and through the pitch the transverse dimension of beam were measured. Results are listed in Tab. 7.1; all profiles are shown in Figs. 7.2, 7.3 and 7.4. The sigmas of Gaussian

Detector	z position (cm)	Beam transverse size (mm)
FI01X1	-759.9	3.28 ± 0.02
FI01Y1	-758.3	6.15 ± 0.03
SI01X1	-378.715	3.14 ± 0.01
SI01Y1	-378.730	2.29 ± 0.01
SI03X1	-278.755	3.05 ± 0.01
SI03Y1	-278.770	2.01 ± 0.01

Table 7.1: Sigmas of Gaussian fit performed on the profile of detectors upstream the target.

fit on x profiles is constant and it is about 3 mm. For y profiles, the fits suggest a similar size, with sigmas going from 6 mm to 2 mm, but with some spread.

7.2.2 Trigger effectiveness

The trigger, as it was used for the 2007 test, is known to behave well. What is unknown is the effectiveness of the trigger for two muons in LAS (Trigger 4). Since this trigger was not ready during the first part of the test, it is possible to compare run with and without this triggger. Run 82224 and run

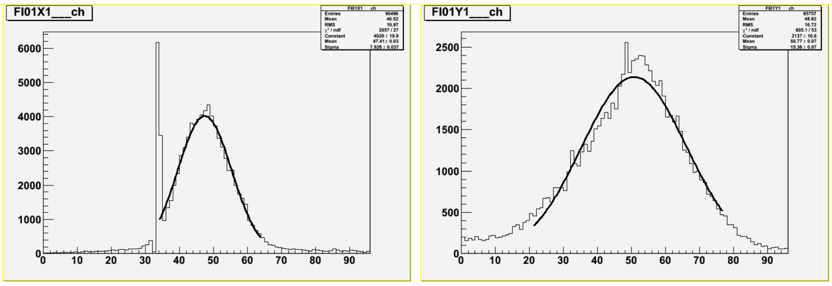

(a) (b)

Figure 7.2: Beam profile on SciFi 1 during 2009 DY test.

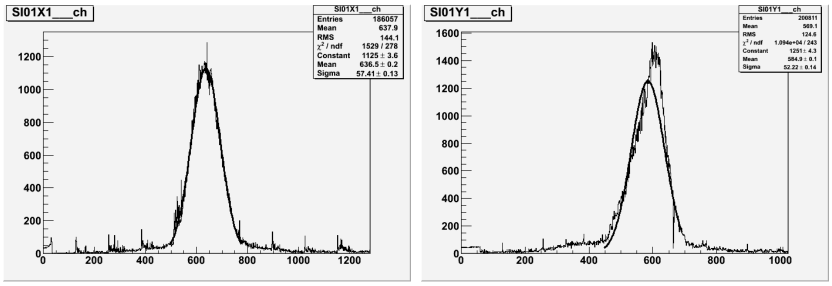

(a) (b)

Figure 7.3: Beam profile on Silicon Station 1 during 2009 DY test.

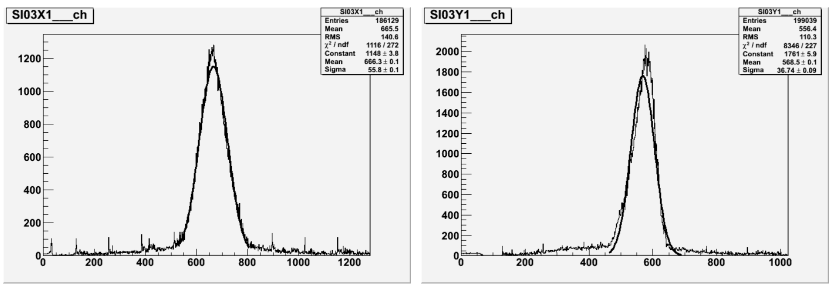

(a) (b)

Figure 7.4: Beam profile on Silicon Station 3 during 2009 DY test.

82266 are considered, the first one without the new trigger and the second one with it. Apart from this difference, these two runs are very similar, with lenghts of 174 spills for run 82224 and 200 for run 82266. Therefore scaling by a factor 200/174 one can compute the expected ratio of numbers of trigger rate and of di-muon pairs. A very preliminary and inaccurate analysis has been performed, looking for di-muon pairs, fixing the energy loss by adding 2 GeV/c to each track emerging from absorber. Results are summarised in Tab. 7.2. From Tab. 7.2, it clearly appears that the number of triggered

		Run 82266	
	Run 82224	Expected	Real
# spills	174	×	200
# Di-muon events	$24.5 \cdot 10^6$	×	$41.1 \cdot 10^6$
# Di-muon events trigger 2	168500	193700	195300
# Scale factor trigger 2	1	×	1
# Di-muon events trigger 4	×	×	$8.8 \cdot 10^6$
# Di-muon events trigger 2 M> 2.5 GeV/c^2	48	55	52
# Di-muon events trigger 4 M> 2.5 GeV/c^2	×	×	4211

Table 7.2: Trigger and event rates for run 82224 and 82266. Expected value for run 82266 are also shown, computed from run 82224. × indicates if a value is not available.

events increases. In particular, when looking at di-muon pairs with mass greater than 2.5 GeV/c^2 one sees that most of them come from events in which this trigger is fired. This happens for two reasons. The trigger of two muons in LAS enlarge the acceptance roughly by a factor of two. Moreover events that are trigger by the other trigger have a significant probability that one muon traverses the dump, thus making the reconstruction harder. It is reasonable to think that the combinations of the two effects can increase the total di-muon statistic by a factor ranging from 2 to 4.

A first confirmation comes from preliminary analysis, which provided the distributions of invariant mass for the two runs. He performed fits on the J/ψ resonances obtaining 170 J/ψ for run 82224 and around 700 for run 82266 (see Figs. 7.5 and 7.6). The gain in statistics is almost a factor of 4. Also, the width computed from the fits seems to be compatible with the

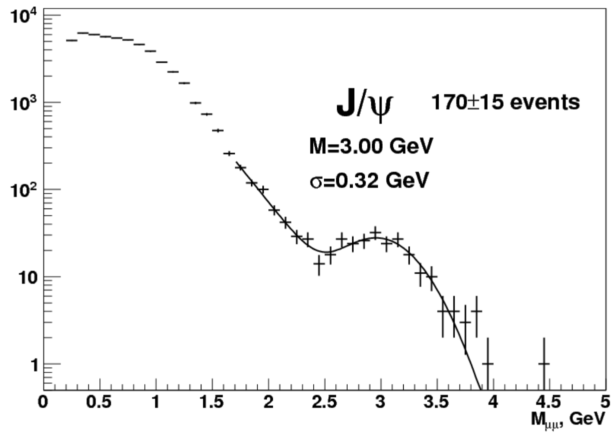

Figure 7.5: J/ψ fit on di-muon invariant mass distribution for run 82224.

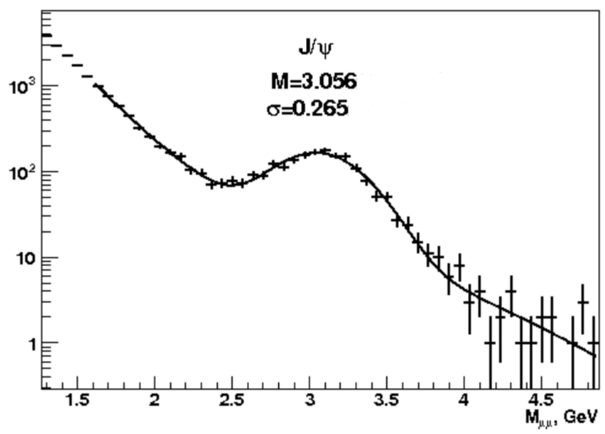

Figure 7.6: J/ψ fit on di-muon invariant mass distribution for run 82266.

reconstruction errors given by the simulations (see Subsec. 6.6.4).

7.2.3 Event size

One aspect that also has to be considered is the total event size. This value affects the capability of the data acquisition to sustain the data flux. This is not the only parameter, but however it must considered to understand if event builders can digest data or not. On the other hand, a small event size may allow to increase the data rate are acquired, compatibly with other existing limit. The event size for Drell-Yan event is expected to be not large due to the presence of the absorber which reduces the particle flux after it and makes detectors not to produce too many data. That was evident

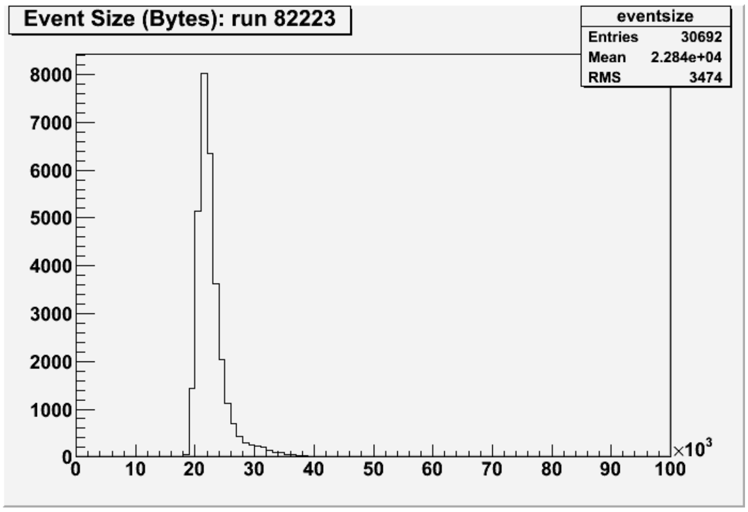

Figure 7.7: Event size from a 2009 Drell-Yan run. Mean value is around 20 kB.

during the test and it can be seen if Fig. 7.7: the mean value of event size is $\sim$ 20 kB. It can be noticed that the distribution is quite different from the one obtained during a muon run (see Fig. 7.8), which is wider, with a greater mean value (twice the Drell-Yan one) and a long tail.

7.2.4 Conclusions

The Drell-Yan 2009 beam test has been performed to study the COMPASS spetrometer as close as possible to the wanted Drell-Yan configuration for a future scientific program. From first looks to the collected data and from on-line observation it can be stated that the test went very well and satistied all expectations. Moreover I had the possibility to contribute to the test by providing the knowledge I had acquired from the simulation studies.

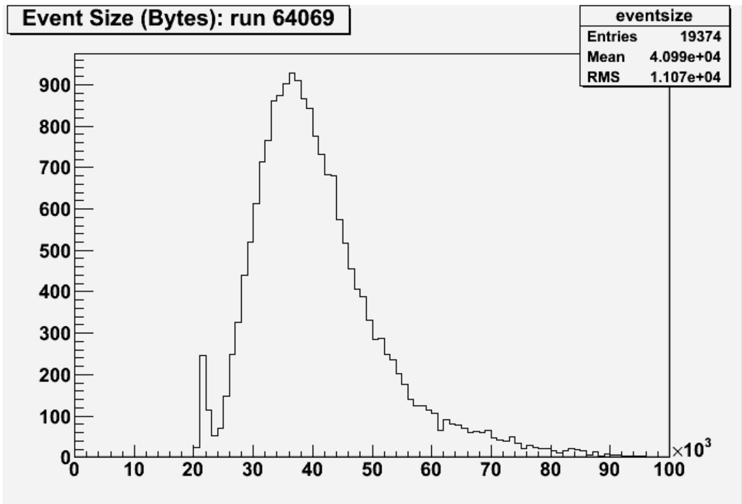

Figure 7.8: Event size from a muon run. Mean value is around 41 kB.

Chapter 8

Conclusions and outlooks

A Proposal for future measurements using the COMPASS spectrometer has been written during the year 2009 and it will be submitted to the Super Proton Synchrotron Committee (SPSC) in 2010. Among the projects being considered, one of them covers the study of transverse momentum dependent (TMD) parton distribution functions (PDF) via the Drell-Yan process. These arguments have been discussed in the first part of this thesis. Other topics were developed: analysis of data acquired during test runs and Monte Carlo studies to understand the feasibility of a Drell-Yan measurement at COMPASS and consequently the optimization and tuning of the apparatus. The information gained from the test and from the simulations have been very useful in writing the Drell-Yan part of the Proposal. Moreover some suggestions had already been useful for the last test done at the end of run 2009.

What appears from Monte Carlo study and tests is that the COMPASS spectrometer is capable to stand and fulfill a Drell-Yan program. However it is clear that upgrades are needed: a hadron absorber is needed (like all other past Drell-Yan experiments) and an upgrade of the trigger is also compulsory. The impact of placing such a large object requires the rearrangement of the area around the target, which implies not only an abvious movement of the target platform, but also a redesign of it. The target itself will probably receive modification, being re-organised in two cells. All changes will obey limits that come from the existing structure and geometry which, for example, makes it impossible to have a hadron absorber longer than about two meters.

That is from hardware point of view. It seems that some improvements can come from analysis program too. The recostruction program seems to suffer all the modification done in the target region. This can find reasons in the algorithms which were not written having in mind that tracks might cross big amount of materials placed between the interaction zone and the spectrometer. However, going back to the hardware, new detectors inserted between the target and the absorber will significantly improve the situation: two pairs of x-y spatial projections can help fixing trajectory. The simulation of this upgraded geometry has not been done yet and it will be done in the future, in a second phase of simulations. At a later time, when the geometry will be definively fixed, study of false asymmetries induced by the spectrometer will be performed as well as the extraction of asymmetries using a dedicated Drell-Yan event generator.

Chapter 9

Appendix

.1 Derivation of Drell-Yan cross section

The Drell-Yan cross section can be calculated and it has the general expression:

$$\sigma\left(H_a + H_b \to \mu^+\mu^- + X\right) = \sum_q \int \mathrm{d}x_a \int \mathrm{d}x_b f_a\left(x_a\right) f_b\left(x_b\right)\, \hat{\sigma}\left(q\bar{q} \to \mu^+\mu^-\right) \tag{1}$$

The cross section is the product of the partonic cross section with the two parton distribution functions, $f_a\left(x_a\right)$ and $f_b\left(x_b\right)$ averaged over quark flavors and spins. $f_a\left(x_a\right)$ and $f_b\left(x_b\right)$ can be interpreted as the probability of finding a quark carrying a fraction x of the momentum of its parent hadron.
The elementary cross section $\hat{\sigma}$ can be computed from first principles. In the partonic center of mass frame (Fig. 1), the $q\bar{q} \to \mu^+\mu^-$ process leads:

$$\begin{aligned} x_a P_a^\mu &= (E_1, 0, 0, E_1) \\ x_b P_b^\mu &= (E_1, 0, 0, -E_1) \\ k_a^\mu &= (E, E\sin\theta, 0, E\cos\theta) \\ k_b^\mu &= (E, -E\sin\theta, 0, -E\cos\theta) \end{aligned}$$

where k_a and k_b are the momenta of the two leptons such that $\left(k_a + k_b\right)^2 = Q^2$ and, for energy conservation law, $Q^2 \equiv \hat{s}$; particles are considered mass-

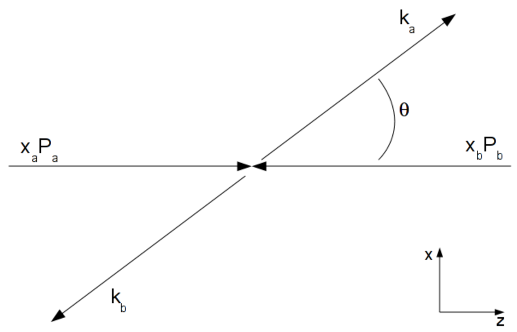

Figure 1: $q\bar{q} \to \mu^+\mu^-$ in partonic center of mass system.

less. The partonic cross section is then:

$$\mathrm{d}\hat{\sigma} = \frac{1}{2\hat{s}} \frac{\mathrm{d}^3 k_a}{(2\pi)^3 \, 2k_a^0} \frac{\mathrm{d}^3 k_b}{(2\pi)^3 \, 2k_b^0} (2\pi)^4 \;\; \delta^4 \left(x_a P_a + x_b P_b - k_a - k_b\right) \times |\bar{M}|^2 \quad (2)$$

Computing $\hat{s}$ and Q^2, one finds:

$$\hat{s} = \left(x_a P_a^\mu + x_b P_b^\mu\right)^2 = 4E_1^2 \quad (3)$$

$$Q^2 = \left(k_a^\mu + k_b^\mu\right)^2 = 4E^2 \quad (4)$$

We can rewrite the phase space appearing in Eq. 2. In the parton center of mass frame, we get:

$$\begin{aligned}
&\frac{1}{2\hat{s}} \frac{\mathrm{d}^3 k_a}{(2\pi)^3 \, 2k_a^0} \frac{\mathrm{d}^3 k_b}{(2\pi)^3 \, 2k_b^0} (2\pi)^4 \;\; \delta^4 \left(x_a P_a + x_b P_b - k_a - k_b\right) = \\
&= \frac{1}{2\hat{s}} \frac{\mathrm{d}E \mathrm{d}\cos\theta \mathrm{d}\phi}{16\pi^2} \; \delta\left(x_a P_a^0 + x_b P_b^0 - k_a^0 - k_a^0\right) \\
&= \frac{1}{16\pi\hat{s}} \mathrm{d}E \mathrm{d}\cos\theta \; \delta\left(\sqrt{\hat{s}} - \sqrt{Q^2}\right) \\
&= \frac{1}{32\pi\hat{s}} \mathrm{d}Q^2 \mathrm{d}\cos\theta \; \delta\left(\hat{s} - Q^2\right) \\
&= \frac{1}{32\pi\hat{s}^2} \mathrm{d}Q^2 \mathrm{d}\cos\theta \; \delta\left(1 - \frac{Q^2}{\hat{s}}\right) \quad (5)
\end{aligned}$$

The squared matrix element of eq. 2 can be written:

$$\begin{aligned}
|\bar{M}|^2 &= \frac{1}{4N_C}\frac{e^4 e_q^2}{Q^4} \cdot L_{\mu\nu}H^{\mu\nu} = \\
&= \frac{1}{4N_C}\frac{e^4 e_q^2}{Q^4}\, 4\left(k_a^\mu k_b^\nu + k_a^\nu k_b^\mu - g^{\mu\nu} k_a \cdot k_b\right) \cdot \\
&\qquad 4\, x_a x_b \left(P_{a\mu}P_{b\nu} + P_{a\nu}P_{b\mu} - g^{\mu\nu} P_a \cdot P_b\right) = \\
&= \frac{4e^4 e_q^2}{N_C Q^4} Q^4 x_a x_b \left(2k_a \cdot P_a k_b \cdot P_b + 2k_a \cdot P_b k_b \cdot P_a\right) = \\
&= \frac{4e^4 e_q^2}{N_C Q^4} Q^4 2E^2 E_1^2 \left[(1+\cos\theta)^2 + (1-\cos\theta)^2\right] = \\
&= \frac{\hat{s}}{N_C} e^4 e_q^2 \frac{1}{Q^2} \cdot \left(1+\cos^2\theta\right)
\end{aligned} \tag{6}$$

where N_C is the number of colours and $L_{\mu\nu}$ and $H^{\mu\nu}$ are respectively the leptonic and partonic tensors. Putting together results in eq. 2 and differentiating it:

$$\begin{aligned}
\frac{\mathrm{d}\hat{\sigma}}{\mathrm{d}Q^2} &= \frac{1}{32\pi\hat{s}^2}\,\delta\left(1-\frac{Q^2}{\hat{s}}\right)\frac{1}{Q^2}\frac{\hat{s}}{N_C}\, e^4 e_q^2 \int_{-1}^{1} \mathrm{d}\cos\theta \left(1+\cos^2\theta\right) = \\
&= \frac{\pi}{2}\alpha^2\, e_q^2 \frac{1}{\hat{s}Q^2}\frac{1}{N_C}\,\delta\left(1-\frac{Q^2}{\hat{s}}\right)\frac{8}{3} = \\
&= \frac{1}{N_C}\frac{4\pi\alpha^2}{3\hat{s}Q^2}\, e_q^2 \delta\left(1-\frac{Q^2}{\hat{s}}\right)
\end{aligned} \tag{7}$$

Then, the prediction for the Drell−Yan cross section, computed from first principles, is:

$$Q^2\frac{\mathrm{d}\sigma}{\mathrm{d}Q^2} = \sum_q e_q^2 \frac{1}{N_C}\frac{4\pi\alpha^2}{3s}\int \frac{\mathrm{d}x_a}{x_a}\frac{\mathrm{d}x_b}{x_b} f_a(x_a)\, f_b(x_b) \cdot \delta\left(1-\frac{Q^2}{x_a x_b s}\right) \tag{8}$$

The prediction can be carried out for the double differential cross section $\frac{\mathrm{d}^2\sigma}{\mathrm{d}Q^2\mathrm{d}y}$. From eq. 8 fixing the rapidity, i.e. inserting a δ function:

$$\begin{aligned}
Q^2\frac{\mathrm{d}^2\sigma}{\mathrm{d}Q^2} &= \sum_q e_q^2 \frac{1}{N_C}\frac{4\pi\alpha^2}{3s}\int \frac{\mathrm{d}x_a}{x_a}\frac{\mathrm{d}x_b}{x_b} f_a(x_a)\, f_b(x_b) \cdot \delta\left(1-\frac{Q^2}{x_a x_b}\right) \\
&\quad \cdot \int \delta\left(y - \frac{1}{2}\ln\frac{x_a}{xb}\right)\mathrm{d}y
\end{aligned} \tag{9}$$

Using:

$$\delta\left(1-\frac{Q^2}{x_a x_b s}\right)=x_a\delta\left(x_a-\frac{Q^2}{x_b s}\right) \tag{10}$$

and

$$\delta\left(y-\frac{1}{2}\ln\frac{Q^2}{x_b^2 s}\right)=x_b\;\delta\left(x_b-\sqrt{\frac{Q^2}{s}}\right) \tag{11}$$

the two integrals in eq. 9 can be done getting:

$$Q^2\frac{\mathrm{d}^2\sigma}{\mathrm{d}Q^2\mathrm{d}y}=\frac{4\pi\alpha^2}{9s}\sum_q e_q^2 f_a\left(x_a\right)f_b\left(x_b\right) \tag{12}$$

List of Figures

Bibliography

[1] J. Ashman et al. An investigation of the spin structure of the proton in deep inelastic scattering of polarized muons on polarized protons. *Nucl. Phys.*, B328:1, 1989.

[2] F. Close. WHERE IS THE PROTON'S SPIN? *AIP Conf. Proc.*, 187:169–176, 1989.

[3] G. Bunce et al. Lambda0 Hyperon Polarization in Inclusive Production by 300-GeV Protons on Beryllium. *Phys. Rev. Lett.*, 36:1113–1116, 1976.

[4] D. L. Adams et al. Analyzing power in inclusive pi+ and pi- production at high x(F) with a 200-GeV polarized proton beam. *Phys. Lett.*, B264:462–466, 1991.

[5] John P. Ralston and Davison E. Soper. Production of Dimuons from High-Energy Polarized Proton Proton Collisions. *Nucl. Phys.*, B152:109, 1979.

[6] Xavier Artru and Mustapha Mekhfi. Transversely Polarized Parton Densities, their Evolution and their Measurement. *Z. Phys.*, C45:669, 1990.

[7] R. L. Jaffe and Xiang-Dong Ji. Chiral odd parton distributions and polarized Drell-Yan. *Phys. Rev. Lett.*, 67:552–555, 1991.

[8] M. Anselmino, A. Efremov, and E. Leader. The theory and phenomenology of polarized deep inelastic scattering. *Phys. Rept.*, 261:1–124, 1995.

[9] Vincenzo Barone, Alessandro Drago, and Philip G. Ratcliffe. Transverse polarisation of quarks in hadrons. *Phys. Rept.*, 359:1–168, 2002.

[10] S. Chekanov et al. Measurement of the neutral current cross section and F2 structure function for deep inelastic e+ p scattering at HERA. *Eur. Phys. J.*, C21:443–471, 2001.

[11] S. Chekanov et al. High-Q**2 neutral current cross sections in e+ p deep inelastic scattering at s**(1/2) = 318-GeV. *Phys. Rev.*, D70:052001, 2004.

[12] C. Adloff et al. Deep-inelastic inclusive e p scattering at low x and a determination of alpha(s). *Eur. Phys. J.*, C21:33–61, 2001.

[13] C. Adloff et al. Measurement and QCD analysis of neutral and charged current cross sections at HERA. *Eur. Phys. J.*, C30:1–32, 2003.

[14] L. W. Whitlow, E. M. Riordan, S. Dasu, Stephen Rock, and A. Bodek. Precise measurements of the proton and deuteron structure functions from a global analysis of the SLAC deep inelastic electron scattering cross-sections. *Phys. Lett.*, B282:475–482, 1992.

[15] A. C. Benvenuti et al. A High Statistics Measurement of the Proton Structure Functions F(2) (x, Q**2) and R from Deep Inelastic Muon Scattering at High Q**2. *Phys. Lett.*, B223:485, 1989.

[16] M. R. Adams et al. Proton and deuteron structure functions in muon scattering at 470-GeV. *Phys. Rev.*, D54:3006–3056, 1996.

[17] M. Arneodo et al. Measurement of the proton and deuteron structure functions, F2(p) and F2(d), and of the ratio sigma(L)/sigma(T). *Nucl. Phys.*, B483:3–43, 1997.

[18] C. Amsler et al. Review of particle physics. *Phys. Lett.*, B667:1, 2008.

[19] P. L. Anthony et al. Deep Inelastic Scattering of Polarized Electrons by Polarized ^{3}He and the Study of the Neutron Spin Structure. *Phys. Rev.*, D54:6620–6650, 1996.

[20] K. Abe et al. Measurements of the proton and deuteron spin structure functions g1 and g2. *Phys. Rev.*, D58:112003, 1998.

[21] K. Abe et al. Precision determination of the neutron spin structure function g1(n). *Phys. Rev. Lett.*, 79:26–30, 1997.

[22] P. L. Anthony et al. Measurement of the deuteron spin structure function g1(d)(x) for 1-(GeV/c)**2 ¡ Q**2 ¡ 40-(GeV/c)**2. *Phys. Lett.*, B463:339–345, 1999.

[23] P. L. Anthony et al. Measurements of the Q**2 dependence of the proton and neutron spin structure functions g1(p) and g1(n). *Phys. Lett.*, B493:19–28, 2000.

[24] X. Zheng et al. Precision measurement of the neutron spin asymmetries and spin-dependent structure functions in the valence quark region. *Phys. Rev.*, C70:065207, 2004.

[25] A. Airapetian et al. Measurement of the proton spin structure function g1(p) with a pure hydrogen target. *Phys. Lett.*, B442:484–492, 1998.

[26] K. Ackerstaff et al. Measurement of the neutron spin structure function g1(n) with a polarized He-3 internal target. *Phys. Lett.*, B404:383–389, 1997.

[27] B. Adeva et al. Spin asymmetries A(1) and structure functions g1 of the proton and the deuteron from polarized high energy muon scattering. *Phys. Rev.*, D58:112001, 1998.

[28] B. Adeva et al. Spin asymmetries A(1) of the proton and the deuteron in the low x and low Q**2 region from polarized high energy muon scattering. *Phys. Rev.*, D60:072004, 1999.

[29] E. S. Ageev et al. Measurement of the spin structure of the deuteron in the DIS region. *Phys. Lett.*, B612:154–164, 2005.

[30] Curtis G. Callan, Jr. and David J. Gross. High-energy electroproduction and the constitution of the electric current. *Phys. Rev. Lett.*, 22:156–159, 1969.

[31] J. Ashman et al. A measurement of the spin asymmetry and determination of the structure function g(1) in deep inelastic muon proton scattering. *Phys. Lett.*, B206:364, 1988.

[32] Guido Altarelli and Graham G. Ross. The Anomalous Gluon Contribution to Polarized Leptoproduction. *Phys. Lett.*, B212:391, 1988.

[33] R. L. Jaffe and Xiang-Dong Ji. Chiral odd parton distributions and Drell-Yan processes. *Nucl. Phys.*, B375:527–560, 1992.

[34] V. Barone and P. G. Ratcliffe. Transverse spin physics. River Edge, USA: World Scientific (2003) 294 p.

[35] Jacques Soffer. Positivity constraints for spin dependent parton distributions. *Phys. Rev. Lett.*, 74:1292–1294, 1995.

[36] Alessandro Bacchetta et al. Semi-inclusive deep inelastic scattering at small transverse momentum. *JHEP*, 02:093, 2007.

[37] John C. Collins. Fragmentation of transversely polarized quarks probed in transverse momentum distributions. *Nucl. Phys.*, B396:161–182, 1993.

[38] Dennis W. Sivers. Single Spin Production Asymmetries from the Hard Scattering of Point-Like Constituents. *Phys. Rev.*, D41:83, 1990.

[39] Dennis W. Sivers. Hard scattering scaling laws for single spin production asymmetries. *Phys. Rev.*, D43:261–263, 1991.

[40] Daniel Boer and P. J. Mulders. Time-reversal odd distribution functions in leptoproduction. *Phys. Rev.*, D57:5780–5786, 1998.

[41] John C. Collins. Leading-twist Single-transverse-spin asymmetries: Drell- Yan and Deep-Inelastic Scattering. *Phys. Lett.*, B536:43–48, 2002.

[42] A. Airapetian et al. Single-spin asymmetries in semi-inclusive deep-inelastic scattering on a transversely polarized hydrogen target. *Phys. Rev. Lett.*, 94:012002, 2005.

[43] Markus Diefenthaler. HERMES measurements of Collins and Sivers asymmetries from a transversely polarised hydrogen target. 2007.

[44] M. Alekseev et al. Collins and Sivers asymmetries for pions and kaons in muon-deuteron DIS. *Phys. Lett.*, B673:127–135, 2009.

[45] M. Anselmino et al. Sivers Effect for Pion and Kaon Production in Semi- Inclusive Deep Inelastic Scattering. *Eur. Phys. J.*, A39:89–100, 2009.

[46] Guenter Baum et al. COMPASS: A Proposal for a Common Muon and Proton Apparatus for Structure and Spectroscopy. CERN-SPSLC-96-14.

[47] D. Thers et al. Micromegas as a large microstrip detector for the COMPASS experiment. *Nucl. Instrum. Meth.*, A469:133–146, 2001.

[48] C. Bernet et al. The 40-cm x 40-cm gaseous microstrip detector Micromegas for the high-luminosity COMPASS experiment at CERN. *Nucl. Instrum. Meth.*, A536:61–69, 2005.

[49] F. Sauli. GEM: A new concept for electron amplification in gas detectors. *Nucl. Instrum. Meth.*, A386:531–534, 1997.

[50] M. C. Altunbas et al. Construction, test and commissioning of the triple-GEM tracking detector for COMPASS. *Nucl. Instrum. Meth.*, A490:177–203, 2002.

[51] F. W. Brasse, G. Falley, K. Thiele, and P. Warnecke. Construction of a Large Drift Chamber and Test Measurements. Hamburg Desy - INTERNAL REPORT F21-76-02 (76,REC.SEP) 49p.

[52] E. Iarocci. Plastic Streamer Tubes and their Applications in High-Energy Physics. *Nucl. Instrum. Meth.*, 217:30–42, 1983.

[53] V. Yu. Alexakhin et al. Simulation of the First Muon Filter for the COMPASS spectrometer. COMPASS Note 1998-6.

[54] G. Alexeev. et al. RICH WALL detector of the Compass spectrometer. COMPASS Note 2002-10.

[55] D. Adams et al. Spin structure of the proton from polarized inclusive deep-inelastic muon proton scattering. *Phys. Rev.*, D56:5330–5358, 1997.

[56] N. Doble, L. Gatignon, G. von Holtey, and F. Novoskoltsev. The Upgrated muon beam at the SPS. *Nucl. Instrum. Meth.*, A343:351–362, 1994.

[57] A. Abragam et al. "principles of dynamic nuclear polarisation". *Rep. Prog. Phys.*, 41:395–467, 1978.

[58] K. Kondo et al. Polarization measurement in the COMPASS polarized target. *Nucl. Instrum. Meth.*, A526:70–75, 2004.

[59] J. Ball et al. First results of the large COMPASS Li^6D polarized target. *Nucl. Instrum. Meth.*, A498:101–111, 2003.

[60] N. Doshita et al. Target material data of 2002 run. COMPASS Note 2003-5.

[61] N. Doshita et al. Target material data of run 2003. COMPASS Note 2003-5.

[62] N. Doshita et al. Performance of the COMPASS polarized target dilution refrigerator. *Nucl. Instrum. Meth.*, A526:138–143, 2004.

[63] E. S. Ageev et al. A new measurement of the Collins and Sivers asymmetries on a transversely polarised deuteron target. *Nucl. Phys.*, B765:31–70, 2007.

[64] K. Gustafsson. Computation of the Dilution Factor for the Year 2002 COMPASS Data. COMPASS Note 2003-3.

[65] N. Doshita et al. The COMPASS polarized target in 2006 and 2007. *AIP Conf. Proc.*, 980:307–311, 2008.

[66] I. Daito et al. Time resolution of multi-cladding scintillating fiber hodoscope. *Nucl. Instrum. Meth.*, A433:587–591, 1999.

[67] J. Bisplinghoff et al. A scintillating fibre hodoscope for high rate applications. *Nucl. Instrum. Meth.*, A490:101–111, 2002.

[68] O. Denisov et al. Monte Carlo simulations for the RICH WALL as a preshower for the ECAL1. COMPASS Note 2005-10.

[69] E. Albrecht et al. Status and characterisation of COMPASS RICH-1. *Nucl. Instrum. Meth.*, A553:215–219, 2005.

[70] P. Abbon et al. The COMPASS Experiment at CERN. *Nucl. Instrum. Meth.*, A577:455–518, 2007.

[71] P. Abbon et al. The COMPASS RICH-1 fast photon detection system. *Nucl. Instrum. Meth.*, A595:23–26, 2008.

[72] G. Braun et al. TDC chip and readout driver developments for COMPASS and LHC experiments. 1998.

[73] O. P. Gavrishchuk et al. Calorimeter for detection of hadrons in the energy range 10-GeV - 100-GeV. *Instrum. Exp. Tech.*, 49:41–55, 2006.

[74] D. Alde et al. Production of G(1590) and other mesons decaying into η pairs by 100 GeV/c π^- on protons . *Nucl. Phys.*, B269:485, 1986.

[75] F. G. Binon et al. HODOSCOPE MULTI - PHOTON SPECTROMETER GAMS-2000. *Nucl. Instr. Meth.*, A248:86, 1986.

[76] F. G. Binon et al. HODOSCOPE GAMMA SPECTROMETER GAMS-200. *Nucl. Instr. Meth.*, 188:507, 1981.

[77] C. Bernet et al. The COMPASS trigger system for muon scattering. *Nucl. Instrum. Meth.*, A550:217–240, 2005.

[78] H. Fischer et al. The COMPASS data acquisition system. *IEEE Trans. Nucl. Sci.*, 49:443–447, 2002.

[79] B. Grube. The Trigger Control System and the Common GEM and Silicon Readout for the COMPASS Experiment. Master's thesis, TU München, 2001.

[80] T. Schmidt. *A Common Readout Driver for the COMPASS Experiment.* PhD thesis, Universität Freiburg, 2002.

[81] A. Grünemaier. *Eine universelle Ausleseschnittstelle für das COMPASS Experiment.* PhD thesis, Universität Freiburg, 2002.

[82] E. van der Bij, R. A. McLaren, O. Boyle, and G. Rubin. S-LINK, a data link interface specification for the LHC era. *IEEE Trans. Nucl. Sci.*, 44:398–402, 1997.

[83] J. H. Christenson et al. Observation of massive muon pairs in hadron collisions. *Phys. Rev. Lett.*, 25:1523–1526, 1970.

[84] S. D. Drell and Tung-Mow Yan. Partons and their applications at high energies. *Ann. Phys.*, 66:578, 1971.

[85] S. D. Drell and Tung-Mow Yan. Massive Lepton Pair Production in Hadron-Hadron Collisions at High-Energies. *Phys. Rev. Lett.*, 25:316–320, 1970.

[86] J. Kubar-Andre and Frank E. Paige. Gluon Corrections to the Drell-Yan Model. *Phys. Rev.*, D19:221, 1979.

[87] Guido Altarelli, R. Keith Ellis, and G. Martinelli. Leptoproduction and Drell-Yan Processes Beyond the Leading Approximation in Chromodynamics. *Nucl. Phys.*, B143:521, 1978.

[88] G. Parisi. Summing Large Perturbative Corrections in QCD. *Phys. Lett.*, B90:295, 1980.

[89] G. Curci and Mario Greco. Large Infrared Corrections in QCD Processes. *Phys. Lett.*, B92:175, 1980.

[90] J. Badier et al. DRELL-YAN EVENTS FROM 400-GeV/c PROTONS: DETERMINATION OF THE K FACTOR IN A LARGE KINEMATICAL DOMAIN. *Z. Phys.*, C26:489, 1985.

[91] G. Moreno et al. Dimuon production in proton - copper collisions at $\sqrt{s} = 38.8$-GeV. *Phys. Rev.*, D43:2815–2836, 1991.

[92] P. L. McGaughey et al. Cross-sections for the production of high mass muon pairs from 800-GeV proton bombardment of H-2. *Phys. Rev.*, D50:3038–3045, 1994.

[93] W. J. Stirling and M. R. Whalley. A Compilation of Drell-Yan cross-sections. *J. Phys.*, G19:D1–D102, 1993.

[94] J. Badier et al. EXPERIMENTAL DETERMINATION OF THE ANTI-PROTON STRUCTURE FUNCTION BY THE DRELL-YAN MECHANISM. *Phys. Lett.*, B96:422, 1980.

[95] J. Badier et al. Experimental Cross-Section for Dimuon Production and the Drell-Yan Model. *Phys. Lett.*, B89:145, 1979.

[96] A. S. Ito et al. Measurement of the continuum of dimuons produced in high- energy proton - nucleus collisions. *Phys. Rev.*, D23:604, 1981.

[97] D. Antreasyan et al. PRODUCTION MECHANISMS OF HIGH MASS MUON PAIRS. DOE/ER/03069-T3.

[98] S. R. Smith et al. EXPERIMENTAL TEST OF THE DRELL-YAN MODEL IN p W $\rightarrow \mu^+ \mu^-$ X. *Phys. Rev. Lett.*, 46:1607, 1981.

[99] J. Badier et al. TEST OF NUCLEAR EFFECTS IN HADRONIC DIMUON PRODUCTION. *Phys. Lett.*, B104:335, 1981.

[100] M. Corden et al. PRODUCTION OF MUON PAIRS IN THE CONTINUUM REGION BY 39.5- GeV/c pi+-, K+-, p AND anti-p BEAMS INCIDENT ON A TUNGSTEN TARGET. *Phys. Lett.*, B96:417, 1980.

[101] M. J. Corden et al. EXPERIMENTAL RESULTS ON J / psi PRODUCTION BY pi+-, K+-, p AND anti-p BEAMS AT 39.5-GeV. *Phys. Lett.*, B96:411, 1980.

[102] S. Falciano et al. A-DEPENDENCE OF MUON PAIR PRODUCTION IN pi- NUCLEUS INTERACTIONS AT 280-GeV/c. *Phys. Lett.*, B104:416, 1981.

[103] B. Alessandro et al. J/psi and psi' production and their normal nuclear absorption in proton nucleus collisions at 400-GeV. *Eur. Phys. J.*, C48:329, 2006.

[104] A. Michelini. HADRON PHYSICS - HARD PROCESS - DILEPTONS. Rapporteur talk given at EPS Int. Conf. on High Energy Physics, Lisbon, Portugal, Jul 9-15, 1981.

[105] D. Antreasyan et al. DIMUON SCALING COMPARISON AT 44-GeV AND 62-GeV. *Phys. Rev. Lett.*, 48:302, 1982.

[106] C. S. Lam and Wu-Ki Tung. A SYSTEMATIC APPROACH TO INCLUSIVE LEPTON PAIR PRODUCTION IN HADRONIC COLLISIONS. *Phys. Rev.*, D18:2447, 1978.

[107] Daniel Boer and Werner Vogelsang. Drell-Yan lepton angular distribution at small transverse momentum. *Phys. Rev.*, D74:014004, 2006.

[108] John C. Collins and Davison E. Soper. Angular distribution of dileptons in high-energy hadron collisions. *Phys. Rev.*, D16:2219, 1977.

[109] C. S. Lam and Wu-Ki Tung. A PARTON MODEL RELATION SANS QCD MODIFICATIONS IN LEPTON PAIR PRODUCTIONS. *Phys. Rev.*, D21:2712, 1980.

[110] P. Chiappetta and M. Le Bellac. ANGULAR DISTRIBUTION OF LEPTON PAIRS IN DRELL-YAN LIKE PROCESSES. *Z. Phys.*, C32:521, 1986.

[111] J. Cleymans and M. Kuroda. COMPARISON OF ANGULAR DISTRIBUTIONS IN pi- N → mu+ mu- anything WITH LOWEST ORDER QCD. *Phys. Lett.*, B105:68, 1981.

[112] J. S. Conway et al. Experimental Study of Muon Pairs Produced by 252-GeV Pions on Tungsten. *Phys. Rev.*, D39:92–122, 1989.

[113] S. Falciano et al. Angular distributions of muon pairs produced by 194-GeV/c negative pions. *Z. Phys.*, C31:513, 1986.

[114] L. Y. Zhu et al. Measurement of angular distributions of Drell-Yan dimuons in p + d interaction at 800-GeV/c. *Phys. Rev. Lett.*, 99:082301, 2007.

[115] A. Brandenburg, O. Nachtmann, and E. Mirkes. Spin effects and factorization in the Drell-Yan process. *Z. Phys.*, C60:697–710, 1993.

[116] D. Boer, A. Brandenburg, O. Nachtmann, and A. Utermann. Factorisation, parton entanglement and the Drell-Yan process. *Eur. Phys. J.*, C40:55–61, 2005.

[117] A. Brandenburg, S. J. Brodsky, Valentin V. Khoze, and Dieter Mueller. Angular distributions in the Drell-Yan process: A Closer look at higher twist effects. *Phys. Rev. Lett.*, 73:939–942, 1994.

[118] K. J. Eskola, P. Hoyer, M. Vanttinen, and R. Vogt. Higher twist effects in the Drell-Yan angular distribution. *Phys. Lett.*, B333:526–530, 1994.

[119] Daniel Boer. Investigating the origins of transverse spin asymmetries at RHIC. *Phys. Rev.*, D60:014012, 1999.

[120] Leonard P. Gamberg, Gary R. Goldstein, and Karo A. Oganessyan. Novel transversity properties in semi-inclusive deep inelastic scattering. *Phys. Rev.*, D67:071504, 2003.

[121] Daniel Boer, Stanley J. Brodsky, and Dae Sung Hwang. Initial state interactions in the unpolarized Drell-Yan process. *Phys. Rev.*, D67:054003, 2003.

[122] Alessandro Bacchetta, Andreas Schaefer, and Jian-Jun Yang. Sivers function in a spectator model with axial-vector diquarks. *Phys. Lett.*, B578:109–118, 2004.

[123] Zhun Lu and Bo-Qiang Ma. Azimuthal asymmetry in unpolarized pi N Drell-Yan process. *Phys. Lett.*, B615:200–206, 2005.

[124] S. Arnold, A. Metz, and M. Schlegel. Dilepton production from polarized hadron hadron collisions. *Phys. Rev.*, D79:034005, 2009.

[125] A. V. Efremov, K. Goeke, S. Menzel, A. Metz, and P. Schweitzer. Sivers effect in semi-inclusive DIS and in the Drell-Yan process. *Phys. Lett.*, B612:233–244, 2005.

[126] J. C. Collins et al. Sivers effect in semi-inclusive deeply inelastic scattering. *Phys. Rev.*, D73:014021, 2006.

[127] M. Anselmino et al. Sivers effect in Drell-Yan processes. *Phys. Rev.*, D79:054010, 2009.

[128] Andrea Bianconi and Marco Radici. Monte Carlo simulation of single spin asymmetries in pion proton collisions. *Phys. Rev.*, D73:114002, 2006.

[129] Alessandro Bacchetta, Francesco Conti, and Marco Radici. Transverse-momentum distributions in a diquark spectator model. *Phys. Rev.*, D78:074010, 2008.

[130] J. Badier et al. Experimental J/psi Hadronic Production from 150-GeV/c to 280-GeV/c. *Z. Phys.*, C20:101, 1983.

[131] William T. Scott. The theory of small-angle multiple scattering of fast charged particles. *Rev. Mod. Phys.*, 35:231–313, 1963.

[132] Virgil L. Highland. Some Practical Remarks on Multiple Scattering. *Nucl. Instr. Meth.*, 129:497, 1975.

[133] Gerald R. Lynch and Orin I. Dahl. Approximations to multiple Coulomb scattering. *Nucl. Instrum. Meth.*, B58:6–10, 1991.

[134] Torbjorn Sjostrand, Stephen Mrenna, and Peter Skands. PYTHIA 6.4 Physics and Manual. *JHEP*, 05:026, 2006.

[135] Andrea Bianconi. A scheme for fast exploratory simulation of azimuthal asymmetries in Drell-Yan experiments at intermediate energies. The DY_AB Monte Carlo event generator. *Nucl. Instrum. Meth.*, A593:562–571, 2008.

[136] S. Guellenstern, P. Gornicki, L. Mankiewicz, and A. Schaefer. Monte Carlo studies of photon production in polarized proton proton collisions. *Nucl. Phys.*, A560:494–500, 1993.

[137] M. R. Whalley, D. Bourilkov, and R. C. Group. The Les Houches Accord PDFs (LHAPDF) and Lhaglue. 2005.

[138] C. Quintans. Private communications.

Acknowledges

I would like to thank prof. Franco Bradamante, who has been my PhD tutor and supervisor of my thesis, who followed my activities during the last three years. I also thank prof. Daniele Panzieri, supervisor of this thesis, who involved me in the preparation of a new experimental proposal.
I thank all the colleagues of the Trieste COMPASS group for all the support that I got from them. I also thank Torino COMPASS group, with whom I worked a lot. I thank all the members of the COMPASS collaboration, who make the experiment possible with their hard work.
I would like to thank prof. Mauro Anselmino who accepted to read my thesis as the referee.
I cannot forget to thank my beloved wife, Angela, who supported me during these years.